

# Computer simulations of cluster and crystal formation in anisotropic colloid-droplet mixtures

Von der Universität Bayreuth  
zur Erlangung des Grades eines  
Doktors der Naturwissenschaften (Dr. rer. nat.)  
genehmigte Abhandlung

von  
Hai Pham Van  
aus Haiphong, Vietnam

1. Gutachter: Prof. Dr. Matthias Schmidt
2. Gutachter: Prof. Dr. Roland Roth

Tag der Einreichung: 07.11.2016  
Tag des Kolloquiums: 18.01.2017



# Abstract

Recent advances in the fabrication of colloidal particles enable the generation of colloids that may be anisotropic in surface chemistry and in shape. However, the main challenge is to organize these anisotropic colloids into novel and well-defined structures for advanced functional materials. This work is concerned with the emulsion-assisted formation of complex structures of anisotropic colloids, including Janus colloids, colloidal dumbbells and patchy colloids. Here, Janus colloids are modeled as colloidal spheres composed of two distinct surfaces corresponding to repulsive and attractive parts. Dumbbells are composed of two colloidal spheres with different sizes or dissimilar materials. Patchy colloids have different compositional patches on their surface.

We use kinetic Monte Carlo simulations to investigate the assembly process of Janus colloids into cluster structures through emulsion droplet evaporation. The cluster configurations obtained range from doublets to convex polyhedra. By decreasing the surface area corresponding to the attractive part of the colloid surface, we find a structural change in cluster configurations from a set of familiar packings that minimize the second moment of the mass distribution to new packings with more spherical symmetry.

Similarly, using kinetic Monte Carlo simulations we investigate the behavior of mixtures of asymmetric colloidal dumbbells and emulsion droplets. We find that the evaporation of the droplets and the competition between the colloid-droplet adsorption energy and colloid-colloid pair interaction leads to the formation of clusters with both closed and open structures. Therefore, stable packings and complex cluster structures can be achieved by controlling the relative size of the colloidal spheres in the dumbbells and/or their interfacial tension with the droplets.

In addition, a binary mixture of droplets and patchy colloids, where patches are arranged in tetrahedral symmetry, is studied with standard Metropolis Monte Carlo simulations. We find stable crystal structures with atomic analogs ZnS, CaF<sub>2</sub> and FCC/HCP (face-centered cubic/hexagonal-close-packed) phase of the droplets coexisting with a dispersed fluid phase of the colloids. The simulated crystal structures agree well with those predicted by close-packing calculations for an intermediate range of droplet-colloid size ratios. A discrepancy between the simulations and theoretical predictions occurs at low and at high size ratios. Furthermore, the results of the simulations for mixtures with anisotropic interactions reveal a richer phase diagram, such as ZnS-gas and ZnS-fluid coexistence, as compared to that with isotropic interactions. For the example of a square planar patch arrangement, we find a particular crystal structure, consisting of two interpenetrating FCC/HCP lattices with bond angles of 90°. Such a structure has no atomic analog. Our fundamental study of generic models of anisotropic colloid-droplet mixtures could provide a promising way towards the fabrication of novel and colloidal complex structures.



# Zusammenfassung

Neuere Fortschritte in der Synthese kolloidaler Teilchen ermöglichen die Herstellung von Kolloiden mit anisotroper Oberflächenchemie und Form. Eine wesentliche Herausforderung ist es, diese anisotropen Kolloide in neuartige und wohldefinierte Strukturen zu organisieren, und somit fortschrittliche funktionale Materialien herzustellen. Die Dissertation behandelt emulsion-unterstützte Formung von komplexen Strukturen anisotroper Kolloide, wie Januskolloide, kolloidale Hanteln ("dumbbells") und Patchkolloide ("patchy colloids"). Dabei werden die Januskolloide modelliert als Kugeln mit zwei unterschiedlichen Hemisphären, die jeweils abstoßend und anziehend sind. Hanteln bestehen aus zwei kolloidalen Kugeln mit unterschiedlicher Größen und Materialbeschaffenheit. Patchkolloide besitzen unterschiedliche anziehende Bereiche auf ihrer Oberfläche.

Kinetische Monte Carlo-Simulationen werden benutzt zur Untersuchung des Assemblierungsprozesses von Januskolloiden zu Clusterstrukturen durch Verdampfen von Emulsionstropfen. Die erzielten Clusterkonfigurationen reichen von Dubletten hin bis zu konvexen Polyedern. Bei Verkleinerung des anziehenden Anteiles der Kolloidoberfläche passiert ein struktureller Übergang der Clusterkonfigurationen von einem Satz von bekannten Packungen, die das zweite Moment der Massenverteilung minimieren, hin zu neuartigen Packungen mit stärker kugelförmiger Symmetrie.

In ähnlicher Weise, unter Benutzung von kinetischen Monte Carlo-Simulationen, wird das Verhalten von Mischungen von asymmetrischen kolloidalen Hanteln und Emulsionströpfchen untersucht. Es zeigt sich, dass das Verdampfen der Tröpfchen und der Wettstreit der Kolloid-Tröpfchen-Adsorptionsenergie mit der Kolloid-Kolloid-Paarwechselwirkung zu der Formung von Clustern mit kompakter, wie auch mit offener Struktur führt. Deshalb können stabile Packungen und komplexe Clusterstrukturen erzielt werden durch Kontrolle des Größenverhältnis der kolloidalen Kugeln in den Hanteln und/oder der Grenzflächenspannung mit den Tröpfchen.

Auch wurde eine binäre Mischung aus Tröpfchen und Patchkolloiden, wobei die Patches in tetraedrischer Symmetrie angeordnet sind, mittels Metropolis Monte Carlo-Simulationen untersucht. Es wurden stabile Kristallstrukturen gefunden mit den atomaren Entsprechungen ZnS,  $\text{CaF}_2$  und FCC/HCP (kubisch flächenzentriert/hexagonal dicht gepackt) als Gitterstrukturen für die Tröpfchen; diese koexistieren mit einer fluiden Phase der Kolloide. Die simulierten Kristallstrukturen stimmen gut überein mit Strukturen, die aus Berechnung der dichtesten Packung folgen, in einem mittleren Bereich des Größenverhältnis von Kolloiden und Tröpfchen. Eine Abweichung zwischen simulierten und berechneten Ergebnissen tritt auf bei kleinen, wie auch bei großen Größenverhältnissen. Weiterhin enthüllen die Ergebnisse von Simulationen von Mischungen mit anisotropen Wechselwirkungen ein reichhaltigeres Phasendiagramm, mit ZnS-gasförmig und ZnS-fluid Koexistenz, verglichen mit dem Fall isotroper Wechselwirkungen. Für das Beispiel einer quadratischen, planaren Anordnung von Patches ergibt sich eine besondere Kristallstruktur, die aus zwei sich einander durchdringenden FCC/HCP Gittern mit neunzig Grad Bindungswinkeln besteht. Diese Struktur hat kein atomares Analogon. Die vorliegende grundlegende Studie generischer Modelle für anisotrope Kolloid-Tröpfchen-Mischungen könnte einen vielversprechenden Weg aufzeigen, hin zur Herstellung von neuartigen und komplexen kolloidalen Strukturen.



# Contents

<b>1. Introduction</b>	<b>1</b>
<b>2. Methods and data analysis</b>	<b>5</b>
2.1. Standard Metropolis Monte Carlo simulation . . . . .	5
2.2. Kinetic Monte Carlo simulation . . . . .	7
2.3. Data analysis . . . . .	9
2.3.1. Radial distribution function . . . . .	9
2.3.2. Coordination number . . . . .	10
2.3.3. Angular distribution function . . . . .	11
2.3.4. Bond order parameter . . . . .	11
<b>3. Cluster structures of Janus colloids assembled by emulsion droplet evaporation</b>	<b>14</b>
3.1. Introduction . . . . .	14
3.2. Model and simulation method . . . . .	17
3.2.1. Pair interaction between Janus colloids . . . . .	17
3.2.2. Droplet-droplet pair interaction . . . . .	20
3.2.3. Janus colloid-droplet pair interaction . . . . .	20
3.2.4. Total interaction energy . . . . .	22
3.2.5. Simulation method . . . . .	22
3.3. Results and discussion . . . . .	23
3.3.1. Dynamics of cluster formation . . . . .	23
3.3.2. Packing of small clusters $n_c \leq 6$ . . . . .	29
3.3.3. Packing of large clusters . . . . .	30
3.3.4. Orientational order parameter of clusters . . . . .	36
3.3.5. Effect of Janus colloid packing fraction on cluster size distribution . . . . .	38
3.3.6. Hierarchical assembly: Superclusters . . . . .	38
3.4. Conclusions . . . . .	41
<b>4. Assembly of open clusters of colloidal dumbbells via droplet evaporation</b>	<b>43</b>
4.1. Introduction . . . . .	43
4.2. Model and simulation method . . . . .	44
4.2.1. Colloid-colloid pair interaction . . . . .	44
4.2.2. Droplet-droplet pair interaction . . . . .	46
4.2.3. Colloid-droplet pair interaction . . . . .	46
4.2.4. Total interaction energy . . . . .	47
4.2.5. Simulation method . . . . .	47

4.3. Results and discussion . . . . .	48
4.3.1. Asymmetric wetting properties and symmetric sizes . . . . .	48
4.3.2. Symmetric wetting properties and asymmetric sizes . . . . .	55
4.4. Conclusions . . . . .	57
<b>5. Crystal structure in binary hard-sphere mixtures with droplets anisotropically bonded to colloids</b>	<b>60</b>
5.1. Introduction . . . . .	60
5.1.1. Binary mixtures of additive hard spheres . . . . .	60
5.1.2. Binary mixtures of oppositely charged colloids . . . . .	62
5.1.3. Binary colloid-droplet mixtures . . . . .	62
5.2. Model and methods . . . . .	63
5.3. Results and discussion . . . . .	67
5.3.1. Close-packing calculation for structures of regular tetrahedral bond distribution . . . . .	67
5.3.2. Simulation results . . . . .	76
5.3.3. Influence of symmetry of patch geometry on the crystal structure of droplet-colloid mixtures . . . . .	85
5.4. Conclusions . . . . .	86
<b>6. Summary and conclusions</b>	<b>88</b>
<b>Appendices</b>	<b>91</b>
<b>A. Cluster analysis</b>	<b>92</b>
A.1. Cluster criterion . . . . .	92
A.2. Cluster initialization . . . . .	93
A.3. Cluster analysis and visualization . . . . .	95
<b>B. Cell lists and neighbor lists</b>	<b>97</b>
<b>C. Generator of patch arrangement in polyhedra</b>	<b>98</b>
<b>Bibliography</b>	<b>100</b>
<b>List of Publications</b>	<b>109</b>
<b>Acknowledgements</b>	<b>110</b>
<b>Eidesstattliche Vericherung</b>	<b>112</b>

# Chapter 1.

## Introduction

The term colloid or colloidal dispersion is used primarily to describe mixtures of a dispersed solid and a continuous liquid phase, where the dispersed phase consists of small particles that range typically from nanometer to micrometer in size and are evenly dispersed (or suspended) throughout the continuous phase. Colloids form an important class of soft matter extensively used in many applications, including pharmaceuticals, food, (non-drip) paints, sewage disposal, and wet photography [1]. Self-assembly processes of colloidal particles into hierarchically organized structures have attracted great interest over the last few decades due to a vast range of different characterization and structure of materials that would not be accessible directly at atomic or molecular scales. For example, by choosing an appropriate ratio between small (S) and large (L) colloidal spheres, Leunissen *et al.* [2] observed crystals with LS, LS<sub>6</sub> and LS<sub>8</sub> stoichiometry for different ionic strengths. One of these structures, LS<sub>8</sub>, has no atomic analogue. In addition, the colloidal self-assembly of basic building blocks also provides useful insights for the fabrication of novel materials with rationally designed functionality. This raises questions as to how colloidal particles can be assembled into more complex structures, what new material properties relate to these structures, and what type of structures are required for practical applications. Answering these questions would not only allow better insights into the mechanism of the formation of complex-structured materials, but also play an important role in production at large scales for technological impact [3]. Within the diverse class of hierarchically organized structures, primary research interest has been focused on two typical structural motifs: colloidal clusters and colloidal crystals.

Colloidal clusters with a small number of constituent particles can be regarded as colloidal analogues to small molecules, i.e. ‘colloidal molecules’ or ‘patchy particles’. They are expected to show more complex behavior than their individual particles [4]. The enormous potential of colloidal clusters has been recognized because of their unique rheological, optical, magnetic, and electric properties [5–7]. The synthetic route towards fabricating colloidal clusters has been pursued by several strategies, including coalescence, physical routes, chemical routes, or two-dimensional (2D) and three-dimensional (3D) geometrical confinement [8]. Manoharan *et al.* [9] reported a method for the fabrication of clusters with complex shapes consisting of micron-sized colloidal spheres. The authors obtained large quantities of these clusters by evaporating the oil droplets in an oil-in-water emulsion. The particles which are adsorbed to the surface of the oil droplets were packed together by capillary forces and held together by van der Waals forces. Based on this technique, Wittemann and coworkers [10–12] also produced clusters but with a considerably smaller size. The experimentally observed structures of the clusters showed good

agreement with those predicted by Monte Carlo simulations, which indicates that the clustering process via emulsion droplet evaporation can lead to stable clusters, or even superclusters [13]. In the results of Manoharan *et al.* and Wittemann *et al.*, clusters consisting of the same number of spherical colloids,  $n_c$ , (for relatively small values of  $n_c$ ) have a unique structure that seems to minimize the second moment of the mass distribution,  $M_2 = \sum_{i=1}^{n_c} |\mathbf{r}_i - \mathbf{r}_{\text{cm}}|^2$ , where  $\mathbf{r}_i$  is the position of the particle  $i$  and  $\mathbf{r}_{\text{cm}}$  is the position of the cluster center-of-mass. Lauga and Brenner [14] later showed that the selection of the unique structure arises purely from geometrical constraints during the evaporation. Pine and coworkers extended the method of Manoharan *et al.* [9] to a wide range of colloidal materials using oil-in-water emulsions [15, 16], water-in-oil emulsions [17, 18] or aerosol droplets [19]. Interestingly, in addition to the familiar  $M_2$ -minimal isomers, the authors found a few particular cluster configurations for  $n_c = 7, 8$  and 11. For example, for  $n_c = 8$  two isomeric clusters were observed: one was a  $M_2$ -minimal cluster called the snub disphenoid configuration and the other a square antiprism configuration which was believed to result from the electrostatic repulsion between colloidal particles at the water-oil interface [17, 19]. However, the reason why these types of isomeric clusters were formed, instead of the  $M_2$ -minimal clusters, is still unknown.

A higher level of complexity can be achieved when the chemical composition of the constituent colloids (or at least their surface chemistry) varies and/or the shape of colloids is extended, ranging from polyhedra [20–23], rods [24, 25], ellipsoids [26, 27] and dumbbells [28]. Particles with such anisotropic properties are interesting, since their complexity offers new routes to tailoring particles for specific tasks. In a review article, Reilly *et al.* [29] classified the key features of anisotropic particles as Janus, multicompartment and patchy architectures and compared their structural properties as well as their preparation techniques. Janus particles (named after the double-faced Roman god) have a biphasic geometry of distinct compositions and properties in their core and/or surface. Multicompartment particles have a multi-phasic anisotropy in the core domain, while patchy particles usually have different compositional patches in the surface [29].

Despite the strong experimental interest in isotropic particles, little research has been done to investigate the emulsion-assisted formation of cluster structures of particles anisotropic in shape or interparticle interactions. Peng *et al.* [30] carried out experiments and simulated the cluster formation of dumbbell-shaped colloids. The authors proposed that the principle of  $M_2$  minimization is not generally true for anisotropic colloidal dumbbell self-assembly. However, the authors predicted cluster structures without considering the differing chemical properties of the constituent colloidal spheres. Very recently, Smallenburg and Löwen [31] studied the close packing of hard spherocylinders confined to a spherical surface and found a rich variety of cluster structures that depends on the number and aspect ratio of the rods. A detailed investigation of the cluster structure of a diverse class of Platonic solids inside spherical confinement, albeit without modeling the interparticle interaction beyond the hard-core repulsion, has also been reported [32].

In this work, based on a basic model for a binary mixture of colloidal particles and spherical emulsion droplets [13], we study the clustering process of colloidal systems via emulsion droplet evaporation by means of kinetic Monte Carlo simulations. We consider some cases of colloidal systems with anisotropic behavior in interparticle interactions (Janus colloidal particles) or shape (colloidal dumbbells). Detailed descriptions of the resulting cluster structures and their size dis-

tribution are presented. We find that stable packings and hence complex colloidal structures can be obtained by controlling the directional interparticle potential (for a system of Janus colloids and droplets), the relative size of colloidal spheres as well as their interfacial tension with droplets (for a system of colloidal dumbbells and droplets). These results may provide not only an explanation for the occurrence of few  $M_2$ -nonminimal isomers found in previous experiments [12, 17, 19, 33], but also be helpful to guide experimental work for preparing and also exploiting complex colloidal building blocks.

In addition to colloidal clusters, enormous efforts have been made to create colloidal crystals in which colloidal particles are arranged in highly ordered 2D or 3D arrays. The organization into crystal-like structures with lattice parameters comparable to the wavelength of visible light shows promising applications in many fields such as photonic bandgap materials [34], chemical sensors [35], and macroporous materials [36]. It is well known that colloidal spheres with centrosymmetric and isotropic interaction potentials arrange in simple crystal structures such as face-centered cubic (FCC), hexagonal close-packed (HCP), and body-centered cubic (BCC). The potential use of the self-assembled colloids in 3D photonic band gap materials, however, requires non-close packed structures (e.g. the diamond structure) that are typically not thermodynamically stable. In addition, the diamond lattice of colloidal molecules remains elusive since colloids require four-fold bond coordination [37]. Using a single-component system of tetrahedral patchy colloids might not be straightforward because of the potentially frustrating effects of a variety of local structures that are possible in the colloidal liquid phase [38]. Another proposed strategy is to prepare binary colloidal crystals assembled from two different materials, and then selectively remove one of them by burning or dissolution. Experimentally, the fabrication of such structures is still, however, challenging [39].

Wang *et al.* [40] recently used the technique of Manoharan *et al.* [9] and Wittemann [10–12] *et al.* to create patchy particles with directional interactions that mimic atoms with valence. This feature allows the fabrication of patchy colloids with triangular, tetrahedral, trigonal dipyramidal, octahedral or pentagonal dipyramidal symmetries. Motivated by this experiment, we study the self-assembly of binary mixtures of patchy colloids and droplets, especially particles with four patches are arranged in a regular tetrahedral symmetry. Using standard Monte Carlo simulations and close-packing considerations, we investigate the influence of the droplet-colloid size ratio, contact angle and concentration of particles on the crystal structures of systems. We find the occurrence of the ZnS-structure (the two-component analog of the diamond lattice) for a certain range of size ratios. Increasing the size ratio leads to a continuous transition from the ZnS- to the  $\text{CaF}_2$ -structure, both of which might be of interest in 3D photonic bandgap materials [41]. Our results identify key parameters to possibly obtain such structures in experiments.

The thesis is organized as follows. Chapter 2 first gives a brief overview of the key ideas of standard Metropolis and kinetic Monte Carlo simulation techniques. Then we discuss the relevant quantities that are used to analyze our simulation data. Chapter 3 presents the results of the dynamics of cluster formation for the mixture of Janus colloidal particles and emulsion droplets obtained by kinetic Monte Carlo simulations. We classify the clusters into two groups based on their sizes and examine the effect of the interparticle interactions between colloidal spheres on the final shape of the clusters. Results for superclusters are given at the end of the

chapter. Chapter 4 provides the results of the assembly of open clusters of colloidal dumbbells via droplet evaporation. We analyze the cluster formation, structures and size distributions for dumbbells with asymmetric properties in either wettability or size. Chapter 5 shows how the influence of the relative size, contact angle, symmetric geometry, and concentration of particles on the crystal structure. The summary and conclusions are given in Chapter 6. Finally, we add several appendices, in which we show more details of various analysis of clusters and numerical implementation.

## Chapter 2.

### Methods and data analysis

In this chapter we describe computer simulations to study the assembly of mixtures of colloids and droplets. Two main methods used are the standard Metropolis and kinetic Monte Carlo simulation, depending on the system of interest. Although there is a little difference in their implementation, the standard Metropolis Monte Carlo method is designed to study the equilibrium behavior of the system, while the kinetic Monte Carlo method involves the dynamics of the system in a simplified way. We briefly introduce the basic principles of both methods.

#### 2.1. Standard Metropolis Monte Carlo simulation

Consider a system of a fixed number of  $N$  particles in a given volume  $V$  at a fixed temperature  $T$ ; a collection of such systems is called a canonical ensemble. The equilibrium probability density,  $f(\mathbf{r}^N, \mathbf{p}^N)$ , for a system with a specific set of particle positions  $\mathbf{r}^N$  and momenta  $\mathbf{p}^N$  is proportional to the Boltzmann factor

$$f(\mathbf{r}^N, \mathbf{p}^N) \propto \exp[-\beta H(\mathbf{r}^N, \mathbf{p}^N)], \quad (2.1)$$

with  $\beta = 1/k_B T$ , where  $k_B$  is the Boltzmann constant,  $H(\mathbf{r}^N, \mathbf{p}^N)$  is the Hamiltonian of the system. The average value of a measurable quantity  $A$  is defined as weighted average of  $A$  over all possible configurations in the system, i.e.

$$\langle A \rangle = \frac{\iint A(\mathbf{r}^N, \mathbf{p}^N) f(\mathbf{r}^N, \mathbf{p}^N) d\mathbf{r}^N d\mathbf{p}^N}{\iint f(\mathbf{r}^N, \mathbf{p}^N) d\mathbf{r}^N d\mathbf{p}^N}. \quad (2.2)$$

Since the potential energy is independent of the momenta of the particles, the Hamiltonian can be separated into the kinetic and potential energy

$$H(\mathbf{r}^N, \mathbf{p}^N) = \sum_{i=0}^N \frac{\mathbf{p}_i^2}{2m} + U(\mathbf{r}^N), \quad (2.3)$$

where  $m$  is the mass of particle,  $\mathbf{r}_{ij}$  is the distance between particles  $i$  and  $j$ ,  $U(\mathbf{r}^N)$  is the total potential energy. If the quantity  $A$  depends only on the particle coordinates, the integrals over

the momenta cancel between the numerator and denominator of Eq. (2.2) to give

$$\langle A \rangle = \frac{\int A(\mathbf{r}^N, \mathbf{p}^N) \exp[-\beta U(\mathbf{r}^N)] d\mathbf{r}^N}{\int \exp[-\beta U(\mathbf{r}^N)] d\mathbf{r}^N}. \quad (2.4)$$

At first sight, one might compute the measurable quantity  $A$  given in Eq. (2.4) from uniformly distributed random configurations, and then weight it by the Boltzmann factor  $\exp[-\beta U(\mathbf{r}^N)]$ . However, this procedure requires a huge number of configurations that would need to be evaluated. Moreover, for most intermolecular potentials, the Boltzmann factor decrease rapidly when some particles are close together. As an example of a fluid of 100 hard spheres at the freezing point, the Boltzmann factor would be non-zero for 1 out of every  $10^{260}$  configurations [42]. This indicates that an overwhelming majority of calculations of Eq. (2.4) will be devoted to configurations that make insignificant contributions to the quantity  $\langle A \rangle$ .

Metropolis *et al.* [43] in 1953 proposed an algorithm that, instead of generating uniform configurations randomly and then weighting them with the Boltzmann factor, one generate non-uniform configurations with the probability distribution function  $\exp[-\beta U(\mathbf{r}^N)]$  and then weight these equally. This algorithm is known as the importance sampling Monte Carlo or Metropolis scheme. To do this, the simulation is set up with a Markov chain that consists of sequential trials in a random process performing transitions from one configuration to the next in a way that follows the Boltzmann distribution.

In practice, in the case of the canonical ensemble the simulation is initialized with one possible configuration with  $N$  particles in a volume  $V$  at a temperature  $T$ . A trial configuration is generated by choosing a particle at random and giving it a small, random displacement. The probability of accepting the trial move as the next configuration in the Markov chain is given by

$$\text{acc}(o \rightarrow n) = \min(1, \exp[-\beta(U(\mathbf{r}_n^N) - U(\mathbf{r}_o^N))]), \quad (2.5)$$

where the subscripts  $o$  and  $n$  refer the old and new configurations, respectively. In the equivalent form,

$$\text{acc}(o \rightarrow n) = \begin{cases} \exp[-\beta(U(\mathbf{r}_n^N) - U(\mathbf{r}_o^N))] & \text{if } U(\mathbf{r}_n) > U(\mathbf{r}_o) \\ 1 & \text{otherwise.} \end{cases} \quad (2.6)$$

The usual scheme is as follows: We generate a trial move from the configuration  $o$  to the configuration  $n$ . Before making the real move, we compute the energy change  $U(\mathbf{r}_n) - U(\mathbf{r}_o)$  of the system caused by the move. If  $U(\mathbf{r}_n) - U(\mathbf{r}_o) \leq 0$  then the move is always accepted. Otherwise, if  $U(\mathbf{r}_n) - U(\mathbf{r}_o) > 0$  then we will accept the move with a probability of  $\exp[-\beta(U(\mathbf{r}_n) - U(\mathbf{r}_o))]$ . In order to determine this probability, we generate a random number  $\xi$  between 0 and 1. If  $\xi \leq \text{acc}(o \rightarrow n)$  then the move is accepted and otherwise it is rejected. Clearly, it is important to generate random numbers that are distributed uniformly in the interval  $[0, 1]$  for avoiding any biased Monte Carlo sampling. One of the most widely used generators, based on the Mersenne Twister algorithm, was developed by Makoto Matsumoto and Takuji Nishimura [44].

The Monte Carlo simulation described here is applicable to the canonical ensemble ( $NVT$

ensemble). For other ensembles, e.g. the isothermal-isobaric ensemble ( $NPT$  ensemble) random displacements of particles are combined with random changes in volume. For the simulation of anisotropic particles rotational moves of the particles must be taken into account. For a detailed description of the Monte Carlo simulation for a variety of ensembles and systems, see Ref. [42].

## 2.2. Kinetic Monte Carlo simulation

The standard Metropolis Monte Carlo simulation has been widely used in many applications in order to study equilibrium thermodynamics [45, 46]. On the other hands, Brownian dynamics (BD) simulations have played a significant role in modeling the dynamic properties of colloidal liquids [46]. However, one of the major drawbacks of the BD method is that a significant contribution of hydrodynamic interactions between the elements of colloidal systems is neglected. This interaction can be taken into account via time-consuming techniques such as lattice Boltzmann or stochastic rotation dynamics. In addition, the BD simulation cannot be directly implemented in the simplest models with non-differentiable (hard) potentials. Although one can apply an event-driven BD technique to treat these interaction types, the implementation of the MC scheme is considerably easier. Moreover, evaluating the forces in the BD simulation becomes more complicated for orientational dependent potentials, while only energy needs to be computed in the MC simulation. Therefore, an investigation of the dynamics of systems using the MC simulation could be an efficient way. The MC technique called kinetic MC (kMC) has been developed to deal with non-equilibrium systems such as the glass-forming system [47], crystal nucleation in hard-sphere colloidal fluids [48], and self-assembly processes [49].

Several reports in the literature have shown that MC schemes consisting of only physically meaningful moves, in the limit of very small displacements, are equivalent to BD schemes. In this way, nearly all the sequential moves of individual particles are accepted but configurational biased moves, cluster moves, swaps are not allowed [50–55]. Here we show a derivation introduced by Kikuchi *et al.* [54]. Although the following derivation is not directly applicable to our numerical implementation, we give it as proof of using the standard MC simulation as a replacement for the BD simulation.

Consider a system of  $N$  particles moving in one-dimension subject to a potential  $U(x)$ . According to the standard Metropolis MC scheme, we give each of  $N$  particles in succession a random displacement,  $x' = x + \Delta x$  with  $\Delta x = \alpha\xi$ , where  $\alpha$  is the maximum displacement and  $\xi$  is a uniform random number between  $-1$  and  $1$ . In other words, the trial displacement is selected in the interval  $[-\alpha, \alpha]$ . Let  $N_\nu$  be the number of new possible positions for the particle in the computer simulation ( $N_\nu$  is large but finite). Then the probability of moving the particle to a new position in the interval  $[-\alpha, \alpha]$  is  $1/N_\nu$ .

We assume that the Metropolis MC scheme can be regarded as a physical process and all the particles move to their new positions in the ‘time’ interval  $\Delta t$ . Then the mean displacement of the particle during this ‘time’ is written as

$$\langle \Delta x \rangle = \sum_{\Delta x > 0} \frac{1}{N_\nu} \Delta x + \sum_{\Delta x < 0} \frac{1}{N_\nu} \exp\left(-\frac{\Delta U}{k_B T}\right) \Delta x, \quad (2.7)$$

where  $\Delta U$  is the change in potential energy of the system, which caused by the move. For convenience, we assume that  $\partial U(x)/\partial x < 0$ . Thus the above equation means that there is a probability of  $1/N_\nu$  for the particle to go right, and a probability of  $1/N_\nu$  times  $\exp(-\Delta U/k_B T)$  to go left. If the maximum displacement  $\alpha$  is small and the change in potential energy  $\Delta U$  is written as

$$\Delta U = \frac{\partial U}{\partial x} \Delta x = \frac{\partial U}{\partial x} \alpha \xi \quad (2.8)$$

then Eq. (2.7) becomes

$$\langle \Delta x \rangle \approx -\frac{\alpha^2}{6} \frac{1}{k_B T} \frac{\partial U}{\partial x}. \quad (2.9)$$

Similarly, the mean-square displacement can be found to be

$$\begin{aligned} \langle (\Delta x)^2 \rangle &= \sum_{\Delta x > 0} \frac{1}{N_\nu} (\Delta x)^2 + \sum_{\Delta x < 0} \frac{1}{N_\nu} \exp\left(-\frac{\Delta U}{k_B T}\right) (\Delta x)^2 \\ &\approx \frac{1}{3} \alpha^2. \end{aligned} \quad (2.10)$$

If we define the diffusion coefficient  $D$  by

$$D = \frac{\langle (\Delta x)^2 \rangle}{2\Delta t} = \frac{\alpha^2}{6} \frac{1}{\Delta t} \quad (2.11)$$

then

$$\frac{\langle \Delta x \rangle}{\Delta t} = -\frac{D}{k_B T} \frac{\partial U}{\partial x} = -\frac{1}{\zeta} \frac{\partial U}{\partial x}, \quad (2.12)$$

where  $\zeta$  is the drag coefficient related to the diffusion coefficient  $D$  via the Einstein relation,  $D/k_B T = 1/\zeta$ .

For the small time step  $\Delta t$  the master equation which governs the MC scheme is equivalent to the Fokker-Planck equation

$$\frac{\partial P(x, t)}{\partial t} = -\frac{\partial}{\partial x} \left( \frac{\langle \Delta x \rangle}{\Delta t} P(x, t) \right) + \frac{1}{2} \frac{\partial^2}{\partial x^2} \left( \frac{\langle \Delta x \rangle^2}{\Delta t} P(x, t) \right), \quad (2.13)$$

where  $P(x, t)$  is the particle distribution function. Substitution of Eqs. (2.11) and (2.12) in Eq. (2.13) leads to

$$\frac{\partial P(x, t)}{\partial t} = \frac{1}{\zeta} \frac{\partial}{\partial x} \left[ \left( \frac{\partial U}{\partial x} \right) P(x, t) \right] + D \frac{\partial^2 P(x, t)}{\partial x^2}. \quad (2.14)$$

This equation has the same form as a diffusion equation for the Brownian particles in the fluid characterized by the diffusion coefficient  $D$  and drag coefficient  $\zeta$ . Thus, by choosing the maximum displacement to match the diffusion property given in Eq. (2.11), the Metropolis MC scheme will adequately describe the dynamics of systems.

Similarly, Sanz and Marenduzzo [56] have shown that the dynamical properties in the crystal nucleation and colloidal self-diffusion in dense suspensions are in good agreement with those

obtained by Metropolis MC simulations as long as the the maximum displacement  $\alpha$  is small enough and the time scale in MC simulations is rescaled with the acceptance probability. Several works have recently reported on the use of kMC as an alternative strategy to study the dynamics of spherical and anisotropic colloidal particles [57–61]. These authors have also found a quantitative agreement between the BD and kMC simulations, especially when the translational and rotational elementary of individual particles are quite small.

## 2.3. Data analysis

In this section we give a short introduction to relevant quantities for analyzing our simulation data.

### 2.3.1. Radial distribution function

For a canonical ensemble of fixed  $N, V, T$  the equilibrium  $n$ -particle density is [62]

$$\begin{aligned}\rho_N^{(n)}(\mathbf{r}^n) &= \frac{N!}{(N-n)! h^{3N} N! Q_N} \iint \exp(-\beta H) d\mathbf{r}^{(N-n)} d\mathbf{p}^N \\ &= \frac{N!}{(N-n)! Z_N} \int \exp[-\beta U(\mathbf{r}^N)] d\mathbf{r}^{(N-n)},\end{aligned}\quad (2.15)$$

where  $h$  is the Planck constant.  $Q_N$  is the canonical partition function and  $Z_N$  is the configuration integral, defined as

$$Q_N = \frac{1}{h^{3N} N!} \iint \exp(-\beta H) d\mathbf{r}^N d\mathbf{p}^N, \quad (2.16)$$

and

$$Z_N = \int \exp[-\beta U(\mathbf{r}^N)] d\mathbf{r}^N. \quad (2.17)$$

The definition of  $n$ -particle density implies that

$$\int \rho_N^{(n)}(\mathbf{r}^n) d\mathbf{r}^n = \frac{N!}{(N-n)!}. \quad (2.18)$$

In particular, the single-particle density  $n = 1$  and pair density  $n = 2$  are often used in theory and simulation to investigate structural but also thermodynamic properties

$$\rho^{(1)}(\mathbf{r}) = \frac{N}{Z_N} \int \exp[-\beta U(\mathbf{r}^N)] d\mathbf{r}^{(N-1)}, \quad (2.19)$$

$$\rho^2(\mathbf{r}, \mathbf{r}') = \frac{N(N-1)}{Z_N} \int \exp[-\beta U(\mathbf{r}^N)] d\mathbf{r}^{(N-2)} \quad (2.20)$$

and hence

$$\int \rho^{(1)}(\mathbf{r}) d\mathbf{r} = N, \quad (2.21)$$

$$\int \rho^{(2)}(\mathbf{r}, \mathbf{r}') d\mathbf{r} d\mathbf{r}' = N(N-1). \quad (2.22)$$

The radial distribution function (RDF) is a binning of the distances between all pairs of particles  $i$  and  $j$ . It can be defined in terms of the corresponding two-particle density as

$$g^{(2)}(\mathbf{r}, \mathbf{r}') = \frac{\rho^{(2)}(\mathbf{r}, \mathbf{r}')}{\rho^{(1)}(\mathbf{r})\rho^{(1)}(\mathbf{r}')}. \quad (2.23)$$

For a two-component system of species 1 and 2 we introduce the pair distribution functions  $g_{11}$ ,  $g_{12}$  and  $g_{22}$  to characterize the correlations between each component:

$$g_{11}^{(2)}(\mathbf{r}, \mathbf{r}') = \frac{\rho_{11}^{(2)}(\mathbf{r}, \mathbf{r}')}{\rho_1^{(1)}(\mathbf{r})\rho_1^{(1)}(\mathbf{r}')}, \quad (2.24)$$

$$g_{22}^{(2)}(\mathbf{r}, \mathbf{r}') = \frac{\rho_{22}^{(2)}(\mathbf{r}, \mathbf{r}')}{\rho_2^{(1)}(\mathbf{r})\rho_2^{(1)}(\mathbf{r}')}, \quad (2.25)$$

and

$$g_{12}^{(2)}(\mathbf{r}, \mathbf{r}') = \frac{\rho_{12}^{(2)}(\mathbf{r}, \mathbf{r}')}{\rho_1^{(1)}(\mathbf{r})\rho_2^{(1)}(\mathbf{r}')}, \quad (2.26)$$

where  $\rho_1, \rho_2$  are the one-particle density for the first component and the second component, respectively;  $\rho_{11}$  is two-particle density of the first component in the presence of the second component, and  $\rho_{12}$  is two-particle density between the first component and the second component. Their explicit formula are generalizations of Eqs. (2.19) and (2.20)

$$\rho_{11}^{(2)}(\mathbf{r}, \mathbf{r}') = \frac{N_1(N_1-1)}{2Z_{N_1N_2}} \int \exp[-\beta U(\mathbf{r}^N)] d\mathbf{r}_1^{N_1-2} d\mathbf{r}_2^{N_2}, \quad (2.27)$$

$$\rho_{22}^{(2)}(\mathbf{r}, \mathbf{r}') = \frac{N_2(N_2-1)}{2Z_{N_1N_2}} \int \exp[-\beta U(\mathbf{r}^N)] d\mathbf{r}_1^{N_2-2} d\mathbf{r}_2^{N_1}, \quad (2.28)$$

$$\rho_{12}^{(2)}(\mathbf{r}, \mathbf{r}') = \frac{N_1N_2}{2Z_{N_1N_2}} \int \exp[-\beta U(\mathbf{r}^N)] d\mathbf{r}_1^{N_1-1} d\mathbf{r}_2^{N_2-1}, \quad (2.29)$$

with  $N_1, N_2$  being the total number of particles of each component. In the limit of very low densities of a homogeneous fluid, the pair distribution functions are directly related to pair potentials  $\phi_{ij}(r)$

$$g_{ij}(r) = \exp[-\beta\phi_{ij}(r)], \quad (2.30)$$

for  $i, j = 1, 2$  and  $r = |\mathbf{r}_2 - \mathbf{r}_1|$ .

### 2.3.2. Coordination number

The coordination number gives the number of neighbors of a particle which are located within a given cutoff radius from the tagged particle. The average coordination number,  $n(r)$ , can be calculated in terms of the radial distribution functions  $g(r)$

$$n(r) = 4\pi \int_0^r r'^2 g(r') \rho dr' \quad (2.31)$$

In fact, the first coordination number  $n_1$  (the first nearest-neighbor number) is often used

$$n_1 = 4\pi \int_0^{r_1} r^2 g(r) \rho dr, \quad (2.32)$$

where  $r_1$  is the position of the first minimum of  $g(r)$ .

While the radial distribution function plays a key role in the physics of liquids because thermodynamic properties can be expressed in terms of integrals over  $g(r)$  [62], the coordination number is particularly useful for the description of the structure of solids. Examples of several perfect crystal structures include  $n_1 = 12$  for the FCC (face-center cubic) and HCP (hexagonal-close packing),  $n_1 = 8$  for BCC (body-center cubic) and  $n_1 = 6$  for SC (simple cubic) structure. For binary mixtures, their crystal structure are described by two coordination numbers corresponding to each species. For example, in the ZnS structure  $n_1$  of Zn and S are equal in value ( $n_1 = 4$ ), but in the CaF<sub>2</sub> structure  $n_1$  of Ca and F are 8 and 4, respectively.

### 2.3.3. Angular distribution function

The angular distribution function (ADF) is a further useful tool to analyze the different crystal structures obtained in simulations. For example, it can be used to distinguish between the perfect FCC and HCP lattices. These are indistinguishable from each other if only using the RDF as a criterion. The ADF is constructed by calculating the bond angles between any three particles in the system, and then analyzing the distribution of bond angles using a histogram. Once all bond angles are known, each bin in the histogram is divided by the total number of bond angles so that each bin represents the probability of finding that angle.

The ADF provides the probability that the bond angle between any three particles falls within a given increment of the arc. However, it is computationally less demanding and also often more informative to consider only bond angles between the first few nearest-neighbors, because that is where the short-ranged order of the system is most evident. Therefore, we need to introduce a cutoff radius of the first or second nearest-neighbor (easily determined from the RDF) and then eliminate all bond angles between particles outside this radius [63].

### 2.3.4. Bond order parameter

In order to determine the local environment of a given particle  $i$ , Steinhardt *et al.* [64] proposed rotationally invariant bond order parameters, defined as

$$q_l(i) = \sqrt{\frac{4\pi}{2l+1} \sum_{m=-l}^l |q_{lm}(i)|^2}, \quad (2.33)$$

where  $q_{lm}$  is the complex function given by

$$q_{lm}(i) = \begin{cases} 0 & \text{if } N_b(i) = 0 \\ \frac{1}{N_b(i)} \sum_{j=1}^{N_b(i)} Y_{lm}(\theta_{ij}, \varphi_{ij}) & \text{otherwise,} \end{cases} \quad (2.34)$$

**Table 2.1.:** Bond order parameters for different structures [67, 68].

Geometry	$\bar{q}_4$	$\bar{q}_6$	$\bar{w}_4$	$\bar{w}_6$
FCC	0.19094	0.57452	-0.15932	-0.0136
HCP	0.09722	0.48476	0.13410	-0.01244
BCC	0.03637	0.51069	0.15932	0.01316
SC	0.76376	0.35355	0.15932	0.01316
icosahedral	0	0.66332	0	-0.16975
liquid	0	0	0	0

where  $Y_{lm}(\theta_{ij}, \varphi_{ij})$  are spherical harmonics and  $\theta_{ij}$  and  $\varphi_{ij}$  are the polar and azimuthal angles of the relative vector  $\mathbf{r}_{ij}$  between particle  $i$  and  $j$  with respect to an arbitrary reference frame.  $N_b(i)$  is the number of the nearest-neighbors of the particle  $i$ ,  $l$  is an integer and  $m$  is an integer which runs from  $-l$  to  $l$ .

Recently Lechner and Dellago [65] have introduced a modified version of the Steinhardt *et al.* order parameters in such a way that the additional information derived from the second nearest-neighbors is taken into account, defining the so-called averaged bond order parameters

$$\bar{q}_l(i) = \sqrt{\frac{4\pi}{2l+1} \sum_{m=-l}^l |\bar{q}_{lm}(i)|^2}, \quad (2.35)$$

and

$$\bar{w}_l(i) = \frac{\sum_{m_1+m_2+m_3=0} \begin{pmatrix} l & l & l \\ m_1 & m_2 & m_3 \end{pmatrix} \bar{q}_{lm_1}(i) \bar{q}_{lm_2}(i) \bar{q}_{lm_3}(i)}{\left( \sum_{m=-l}^l |\bar{q}_{lm}(i)| \right)^{3/2}}, \quad (2.36)$$

where the coefficient  $\begin{pmatrix} l & l & l \\ m_1 & m_2 & m_3 \end{pmatrix}$  is the Wigner 3- $j$  symbol [66]. The integers  $m_1$ ,  $m_2$  and  $m_3$  run from  $-l$  to  $l$ , but with the constraint  $m_1 + m_2 + m_3 = 0$ , and  $\bar{q}_{lm}(i)$  is defined as

$$\bar{q}_{lm}(i) = \frac{1}{\tilde{N}_b(i)} \sum_{k=0}^{\tilde{N}_b(i)} q_{lm}(k). \quad (2.37)$$

Here the sum for  $k$  runs for all neighboring particles  $\tilde{N}_b(i)$  of particle  $i$  plus the particle  $i$  itself. In our analysis, the neighbors of particle  $i$  are defined as those particles located within the distance cutoff corresponding to the first minimum of the radial distribution functions. Using the averaged bond order parameter allows to improve the accuracy of the distinction of different crystalline phases and clusters, i.e. FCC, HCP, and BCC. The crystalline structure around a given particle is sufficiently determined by the combination of four average local bond order parameters  $\bar{q}_4$ ,  $\bar{q}_6$ ,  $\bar{w}_4$  and  $\bar{w}_6$ . The values of bond order parameters for several perfect crystal structures are listed in Tab. 2.1.

In order to classify the state of particles into liquid-like, FCC-like, HCP-like and BCC-like we use the following criteria [69]. First, if  $\bar{q}_6 < 0.3$ , particle is classified as liquid-like. Otherwise, if

**Table 2.2.:** Criterion to determine the state of a particle based on average local bond order parameters [69].

State of a particle	$\bar{q}_4$	$\bar{q}_6$	$\bar{w}_4$	$\bar{w}_6$
liquid		$\bar{q}_6 < 0.3$		
BCC structure		$\bar{q}_6 > 0.3$		$\bar{w}_6 > 0$
HCP structure		$\bar{q}_6 > 0.3$	$\bar{w}_4 > 0$	$\bar{w}_6 < 0$
FCC structure		$\bar{q}_6 > 0.3$	$\bar{w}_4 < 0$	$\bar{w}_6 < 0$

$\bar{q}_6 > 0.3$  it is considered as crystalline. If the particle is crystalline and  $\bar{w}_6 > 0$ , it is classified as BCC-like. If the particle is not BCC-like but crystalline,  $\bar{w}_4$  will be checked. If  $\bar{w}_4 > 0$ , the particle is HCP-like, otherwise it is FCC-like (see Tab. 2.2).

## Chapter 3.

# Cluster structures of Janus colloids assembled by emulsion droplet evaporation

### 3.1. Introduction

Janus particles, named after the Roman god Janus, are formed by colloidal particles that possess two different surface chemical functionalities distributed in the two hemispheres. In 1991, the term “Janus grains” was first mentioned by Pierre-Gilles de Gennes in his Nobel lecture titled “Soft Matter” [70]. According to de Gennes, Janus grains composed of polar and apolar hemispheres can arrange to form a monolayer in a similar way to conventional molecular surfactants at an air/water interface. However, while the monolayer of molecular surfactants would be dense and impermeable, the monolayer of Janus grains has some interstices between grains, and therefore allows the chemical exchange between air and water. de Gennes also suggested that this behavior possibly makes Janus particles useful in various applications.

In general, Janus particles can be classified into several different categories, based on the particles’ chemical composition such as polymeric, inorganic and polymer-inorganic or on their shapes such as spherical, ellipsoidal, cylindrical, dumbbell-like (see Fig. 3.1). Among these possibilities, spherical Janus particles with hemispherical coverage are the most typical anisotropic particles since their chemical composition and size can be relatively easily controlled in experiments. However, in some specific cases colloidal particles whose covered and exposed surface area are different may be a better choice for certain applications.

In fact, due to the difficulty of finding synthetic methods for these Janus particles the idea of de Gennes has not received much interest until the last decade. With the recent advances in the fabrication as well as motivation from unique properties of Janus particles in practical applications, the related research has attracted increasing attention [71, 72]. Many approaches

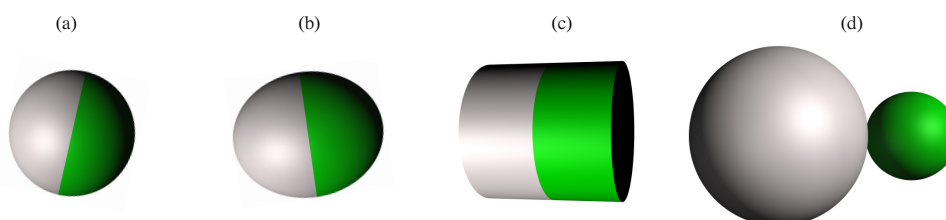


**Figure 3.1.:** Several possible Janus particle architectures differing in shape (a) spherical, (b) ellipsoidal, (c) cylindrical and (d) dumbbell-shaped.

can be taken to fabricate Janus particles with size ranging from micro- to nanoscopic length scales such as microfluidics [73–75], electrohydrodynamic jetting [76, 77], layer-by-layer assembly [78, 79], copolymers self-assembly [80–82]. Recently, Hong *et al.* [83] have reported a simple method, based on the Pickering effect, to prepare Janus particles using oil-water emulsions. The process is conducted as follows: silica particles are initially dispersed in a liquid wax at high temperature, and then mixed with water. Silica particles are entrapped on the surface of the wax droplet, thereby stabilizing the Pickering emulsion. When cooling the mixture to room temperature, the wax solidifies. This restricts the rotation of the trapped silica particles on wax surface. The particles can then be chemically modified on their exposed surface. Furthermore, appropriate surfactants that adsorb onto the exposed surface allow to control the Janus balance [84–86].

One of major goals in the fabrication of novel materials with desired functionalities is to control assembly processes into hierarchically organized structures. Of particular interest are Janus particles because of their tunable chemical anisotropy on both hemispheres [87]. Many studies have been conducted regarding the aggregation behavior of these particles, focusing on a variety of interactions, e.g. between dipolar particles, amphiphilic particles and magnetic/metallic particles under the influence of external fields [74, 80, 81, 88, 89].

For dipolar Janus particles, Goyal *et al.* [90] used molecular dynamics simulation to predict a phase diagram that displays a variety of self-assembled microstructures including face-centered cubic, hexagonal-close packed, and body-centered tetragonal lattices at high packing fractions and fluid, string-fluid, and gel phases at lower packing fractions. In experiments and Monte Carlo simulations, Hong *et al.* [88] reported spontaneous particle aggregation into well-defined geometric clusters depending on the number of the constituent particles. This result also differs from the chain-like assembly of electric dipoles [91–94] and magnetic dipoles [95] as a result of the difference in the Janus balance of Janus particles.

Self-assembly behavior of amphiphilic Janus particles whose two hemispheres are negatively charged and hydrophobic, respectively, were investigated by Granick and co-workers [96, 97]. In these studies, the salt concentration is used as an important parameter for controlling the electrostatic screening length. First, in the absence of salt the strong electrostatic repulsive force among amphiphilic Janus particles keeps them separated in solution. Along with increasing the salt concentration the electrostatic screening length reduces, and as a result, small clusters form. Further reduction of the electrostatic screening length extends progressively these clusters into worm-like objects. Experimental results complemented by Monte Carlo simulations reveal the existence of several distinct cluster structures with the same number of constituent particles,  $n_c$ . For example, two types of clusters that can rearrange dynamically were found in the case of the tetramer ( $n_c = 4$ ). One of these types belongs to the conventional tetrahedron and the other is less densely packed [96]. Further investigations of the kinetics of self-assembly processes show that cluster growth is promoted through three different reaction mechanisms: progressive aggregation of single particles, aggregation of small clusters into a single large one and isomerization.

Motivated by experimental results of Granick and co-workers [96], Sciortino *et al.* [98] performed numerical simulations to investigate the phase behavior and collective structure of Janus particles. The phase diagram exhibits a re-entrant transition, characterized by the shrinking and the shift of the phase coexistence region to higher densities at a low temperature below the

critical temperature. This unconventional phase behavior is due to the formation of clusters including micelles (Janus particles self-assemble into a spherical shell) and vesicles (Janus particles self-assemble into two concentric spherical shells) [98]. Fantoni *et al.* [99, 100] developed a cluster theory to describe the micellization process in the gas phase and found equilibrium cluster concentrations in good agreement with the numerical simulations of [98]. Sciortino *et al.* [101] analyzed in great detail the formation process of clusters and their size distribution by tuning progressively the surface coverage  $\chi$  (fraction of surface covered by the attractive part) of Janus particles in the both gas and liquid phase. The result shows the peculiar phase coexistence behavior of Janus particles ( $\chi = 0.5$ ) distinguishing them from the standard behavior of simple liquids for all  $\chi > 0.5$  cases. Several studies using molecular dynamics simulation have recently been aimed at the self-assembly behavior of Janus particles under different conditions including three-dimensional channels [102], shear flow [103] and electrolyte solutions [104]. These results suggest that the systematic tuning of parameters provides a rich variety of structures such as single, double, triple, quadruple chains and Boerdijk-Coxeter helices [102, 104].

The Pickering emulsion method was not only subsequently used to prepare individual Janus particles [83, 105], but it also represents one of the most effective strategies to produce hierarchically clustered structures with high stability and large yield. The fabrication of clusters or “colloidosomes”, based on Pickering emulsions, was first reported by Velev and co-workers [106–108]. In a series of experiments a rich variety of structures was made by taking advantage of the aggregation behavior of particles on droplets. Here the particles that are adsorbed at the liquid-liquid interface reduce the total interfacial energy and thus can be used to stabilize emulsions and foams against coalescence between droplets [109]. The subsequent removal of emulsion droplets by evaporation generates capillary forces which pack the particles into a specific configuration. This configuration is then stabilized by van der Waals forces once the particles are pulled close enough together [9]. Manoharan *et al.* fabricated micron-sized clusters with complex geometries from polystyrene, silica or polymer microspheres [9, 15, 16]. Although the several types of colloidal particles used differ widely in their sizes, interparticle interactions and surface properties, it is noticeable that the final cluster configurations made from the same number of constituent particles  $n_c$  ( $n_c \leq 11$ ) are nearly identical and equivalent to spherical packings that seem to minimize the second moment of their mass distribution  $M_2$  [110]. However, for  $n_c > 11$ , the clusters obtained from the experiments deviate increasingly from the minimal moment rule [9, 15]. In addition, when the particles are trapped at the interface between the water phase and the oil phase of low dielectric constant, the interparticle electrostatic repulsion can be enhanced due to an asymmetric charge distribution at the particle surface. The long-ranged dipole-dipole repulsion through the oil phase may lead to an ordered arrangement of the particles at the droplet surface [16].

Although the emulsion evaporation technique of Manoharan’s group was used to synthesize successfully for micron-sized particles, it did not elaborate for particles with a diameter of the hundred-nanometer scale due to the rupture of micron-sized oil droplets during the evaporation process [7]. A novel approach towards nano-sized clusters based on a miniemulsion technique was developed by Wittemann and co-workers [10–12]. The polymer colloidal particles were initially suspended in the oil phase or alternatively in the aqueous phase. The samples were then emulsified

by ultrasonication in order to obtain narrowly size distributed droplets with average sizes in the range of 360 nm to 2000 nm [12]. Finally, the complete evaporation of oil droplets yielded a large number of stable clusters of colloidal particles where the number of constituent particles  $n_c$  varies between about 2 and 12. Similarly, Cho *et al.* prepared colloidal clusters under different conditions, e.g. water-in-oil emulsion [17] and found a few particular cases of 7-, 8-, and 11-sphere clusters that have not been observed in experiments based on oil-in-water emulsions [18]. These authors suggested that isomeric structures depend on the surface properties of colloidal particles. Schwarz [13] have reported that while the most typical cluster structures with  $2 \leq n_c \leq 12$  (except  $n_c = 11$ ) are in good agreement with those found in Ref. [9, 15], changing the model of short-ranged attractive interaction can produce different non-minimal isomers and the fraction of isomers can be varied for each number of constituent particles.

Despite numerous studies of the self-assembly into hierarchically organized structures and of the phase behavior of Janus particles, the cluster formation as well as cluster structure templated by emulsion droplets is unknown at present. In this chapter, we give a systematic investigation of the cluster assembly of Janus colloidal particles via droplet evaporation, based on a simple theoretical model proposed in Ref. [13] and the experimental results of Ref. [10–12]. The anisotropic colloid-colloid interaction is modeled via a Kern-Frenkel potential [111], a model that has been extensively used to study the self-assembly of patchy colloids. By varying the attractive patchy area of Janus colloidal particles we find a variety of particular structures in addition to a set of common  $M_2$ -minimal structures. In particular, such cluster structures are very similar to those reported by Cho *et al.* [18, 19]. From these observations we believe that the anisotropic behavior of colloids is related directly to the geometric structures of clusters that appear to maximize a specific orientational order parameter of clusters.

This chapter is organized as follows. We introduce the details of the pair interactions and the simulation method in Sec. 3.2. We analyze the dynamics of cluster formation in Sec. 3.3.1. In Secs. 3.3.2 and 3.3.3 we describe the results for structures and cluster size distributions for small and large clusters, respectively. In Sec. 3.3.4 we analyze the orientational order parameter of clusters. In Sec. 3.3.5 we show the results for the effect of the colloid packing fraction on the size distribution of clusters. In Sec. 3.3.6 we present the results for superclusters of Janus colloids. Final remarks and conclusions are given in Sec. 3.4.

## 3.2. Model and simulation method

### 3.2.1. Pair interaction between Janus colloids

For a system of hard spheres the phase diagram exhibits only a single fluid phase and a crystal phase [112]. Introducing short-ranged attractions such as the Asakura-Oosawa depletion [113, 114], attractive Yukawa [115] or square-well potential [116, 117] into colloidal systems results in gas-liquid (or fluid-fluid) phase equilibrium. Recently a new simple model was proposed by Kern and Frenkel to describe colloidal particles with anisotropic interactions [111] that can be found in a variety of biological systems such as globular proteins [111, 118–120] and colloidal suspensions [111, 121]. In addition, in order to describe charged colloidal particles and proteins

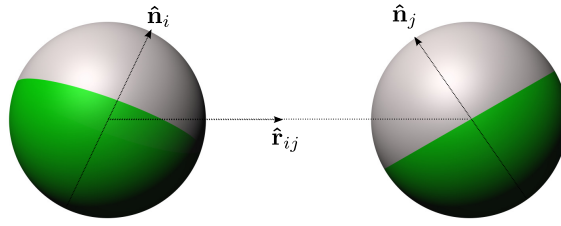


**Figure 3.2.:** Representation of the single-patch Kern-Frenkel model with surface coverage  $\chi = 1/2$ . The surface of the particle is partitioned into two hemispheres where the white and green region corresponds to the attractive and repulsive part, respectively. Here  $\hat{\mathbf{r}}_{ij}$  is the direction joining the two sphere centers, pointing from the center of sphere  $i$  to the center of sphere  $j$ ;  $\hat{\mathbf{n}}_i, \hat{\mathbf{n}}_j$  are vectors specifying directions of the attractive patch of sphere  $i$  and sphere  $j$ , respectively.

in electrolyte solution where electrostatic interactions play a role in the structure and phase behavior [122], the Derjaguin-Landau-Verwey-Overbeek (DLVO) potential or screened electrostatic Yukawa potential can be employed.

In the Kern-Frenkel model [111], colloid  $i$  of hard-sphere diameter  $\sigma_c$  possesses a central position and a set of unit vectors  $\{\hat{\mathbf{n}}_i^k\}$  locating the position of patch  $k$  on the particle surface. The size of the attractive patch is characterized by a conical segment of (half) opening angle  $\delta$  around the direction  $\hat{\mathbf{n}}_i^k$ . It is convenient to define the surface coverage  $\chi$  as the relative ratio between the attractive surface area and total surface area. Therefore,  $\chi$  is related to the half opening angle  $\delta$  and the number of patches  $n_p$  via

$$\chi = n_p \sin^2 \left( \frac{\delta}{2} \right). \quad (3.1)$$

In the present chapter, we only consider a single patch per particle, therefore  $n_p = 1$  and  $k = 1$ . The patch label  $k$  in the unit vectors  $\hat{\mathbf{n}}_i^k$  is omitted for clarity. The short-ranged attractive pair potential,  $U_{\text{KF}}(\hat{\mathbf{r}}_{ij}, \hat{\mathbf{n}}_i, \hat{\mathbf{n}}_j)$ , is defined as a product of a square-well potential with an angular modulation

$$U_{\text{KF}}(\mathbf{r}_{ij}, \hat{\mathbf{n}}_i, \hat{\mathbf{n}}_j) = U_{\text{SW}}(r) \Psi(\hat{\mathbf{r}}_{ij}, \hat{\mathbf{n}}_i, \hat{\mathbf{n}}_j), \quad (3.2)$$

where

$$U_{\text{SW}}(r) = \begin{cases} \infty & r < \sigma_c \\ -\epsilon_{\text{SW}} & \sigma_c < r < \sigma_c + \Delta \\ 0 & \text{otherwise,} \end{cases} \quad (3.3)$$

and

$$\Psi(\hat{\mathbf{r}}_{ij}, \hat{\mathbf{n}}_i, \hat{\mathbf{n}}_j) = \begin{cases} 1 & \text{if } \hat{\mathbf{n}}_i \cdot \hat{\mathbf{r}}_{ij} \geq \cos \delta \text{ and } -\hat{\mathbf{n}}_j \cdot \hat{\mathbf{r}}_{ij} \geq \cos \delta \\ 0 & \text{otherwise,} \end{cases} \quad (3.4)$$

where  $U_{\text{SW}}(r)$  is an isotropic square-well potential of depth  $\epsilon_{\text{SW}}$  and width  $\Delta$ .  $\Psi(\hat{\mathbf{r}}_{ij}, \hat{\mathbf{n}}_i, \hat{\mathbf{n}}_j)$  is a modulation function that depends on the relative orientation of the two particles,  $\hat{\mathbf{n}}_i(\hat{\mathbf{n}}_j)$  is the unit vector pointing from the center of sphere  $i(j)$  to the center of the corresponding attractive patch and  $\hat{\mathbf{r}}_{ij}$  is the unit vector of magnitude  $r$  between the centers of two spheres (see Fig. 3.2).

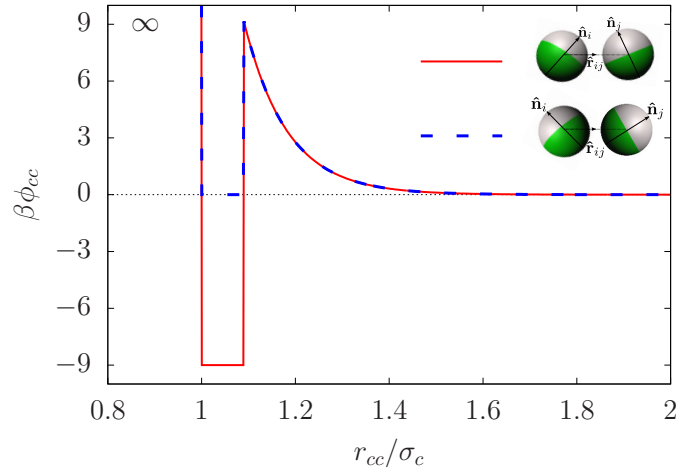


**Figure 3.3.:** Janus colloid-colloid pair interactions given parameters with  $\chi = 1/2$ ,  $\kappa\sigma_c = 10$ ,  $\beta\epsilon_Y = 24.6$ ,  $\beta\epsilon_{SW} = 9$ ,  $\Delta = 0.09\sigma_c$  where  $\beta = 1/k_B T$ . When the attractive parts of two particles properly face each other, they interact via the square-well potential of depth  $18k_B T$  (red solid line), and otherwise they interact via the square-well potential of depth  $9k_B T$  (blue dashed line).

By varying the surface coverage  $\chi$ , one can control the angular range of the anisotropic interactions. The case  $\chi = 1/2$  ( $\delta = 90^\circ$ ) is known as the Janus limit with half-half geometry [123], as illustrated in Fig. 3.2.

The Yukawa repulsion  $U_Y(r)$  describes the interactions between two charged colloidal particles screened by a electrolyte solution with inverse Debye length  $\kappa$ , i.e.

$$U_Y(r) = \epsilon_Y \sigma_c \frac{\exp[-\kappa(r - \sigma_c)]}{r}, \quad (3.5)$$

where the parameter  $\epsilon_Y$  controls the strength of the repulsion.

The total interaction energy between two spherical Janus particles is written in term of the single-patch short-ranged attraction  $U_{KF}(\hat{\mathbf{r}}_{ij}, \hat{\mathbf{n}}_i, \hat{\mathbf{n}}_j)$  and the longer-ranged Yukawa repulsion  $U_Y(r)$ , i.e.

$$\phi_{cc}(\mathbf{r}_{ij}, \hat{\mathbf{n}}_i, \hat{\mathbf{n}}_j) = \begin{cases} \infty & r < \sigma_c \\ U_{KF}(r) & \sigma_c < r < \sigma_c + \Delta \\ U_Y(r) & \text{otherwise.} \end{cases} \quad (3.6)$$

As shown in Fig. 3.3, the potential  $\phi_{cc}(\hat{\mathbf{r}}_{ij}, \hat{\mathbf{n}}_i, \hat{\mathbf{n}}_j)$  defined by Eq. (3.6) is plotted for a typical set of parameters (justified below). Here two particles interact via the square-well potential of depth  $18k_B T$  only if both the patch unit vectors  $\hat{\mathbf{n}}_i$  and  $\hat{\mathbf{n}}_j$  form angles smaller than  $\delta$  with the vector connecting each particle to the other, and the distance between the two particles is within the range  $(\sigma, \sigma + \Delta)$ .

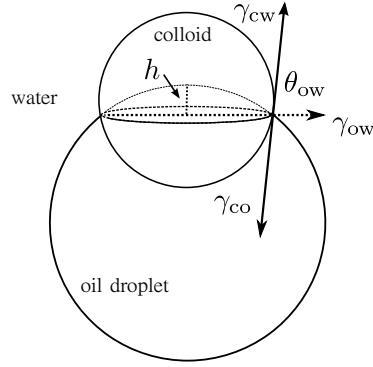


**Figure 3.4.:** Representative diagram of a spherical colloidal particle located at an oil-water interface with the interfacial tension  $\gamma_{ow}$ . Also shown is the colloid-oil interfacial tension  $\gamma_{co}$  and the colloid-water interfacial tension  $\gamma_{cw}$ , the height of the spherical cap  $h$  and the contact angle  $\theta_{ow}$ . The Young equation can be interpreted as a force balance of interfacial tensions (marked by arrows).

### 3.2.2. Droplet-droplet pair interaction

The droplet-droplet interaction is aimed at modeling the repulsive interaction of charged droplets so that coalescence is negligible. Furthermore, in order to avoid the binding between any two droplets due to a shared Janus colloid we assume that each droplet has an effective interaction diameter  $\sigma_d + \sigma_c$  that is larger than the geometric droplet diameter  $\sigma_d$ . Hence the droplet-droplet pair interaction is

$$\phi_{dd}(r) = \begin{cases} \infty & r < \sigma_d + \sigma_c \\ 0 & \text{otherwise.} \end{cases} \quad (3.7)$$

### 3.2.3. Janus colloid-droplet pair interaction

Figure 3.4 shows a schematic diagram of a colloidal particle at an oil-water (droplet-solvent) interface. The contact angle (measured in the water phase),  $\theta_{ow}$ , is related to the three interfacial tensions by the Young equation

$$\cos \theta_{ow} = \frac{\gamma_{co} - \gamma_{cw}}{\gamma_{ow}}, \quad (3.8)$$

where  $\gamma_{co}$ ,  $\gamma_{cw}$  and  $\gamma_{ow}$  represent the colloid-oil, colloid-water and oil-water interfacial tensions. The free energy  $-\Delta G_{\text{int}}$  needed to detach the colloid of diameter  $\sigma_c$  from the interface due to the Pickering effect [124] is

$$-\Delta G_{\text{int}} = \frac{\pi}{4} \sigma_c^2 \gamma_{ow} (1 \pm \cos \theta_{ow})^2, \quad (3.9)$$

where the minus and plus sign inside the bracket correspond to the removal of the colloid into the water phase and into the oil phase, respectively. The binding energy is of the order of  $10^3 - 10^5 k_B T$  for nano-sized spherical silica,  $\gamma_{ow} = 0.036 \text{ Nm}^{-1}$  and  $\theta_{ow} = 90^\circ$  [125]. However, equation (3.9) is only valid when the contact angle  $\theta_{ow}$  is formed by the planar interface. In the case of a particle located at a spherically curved water-oil interface, as shown in Fig. 3.4, the free energy is a more complicated function of the oil droplet diameter [125].

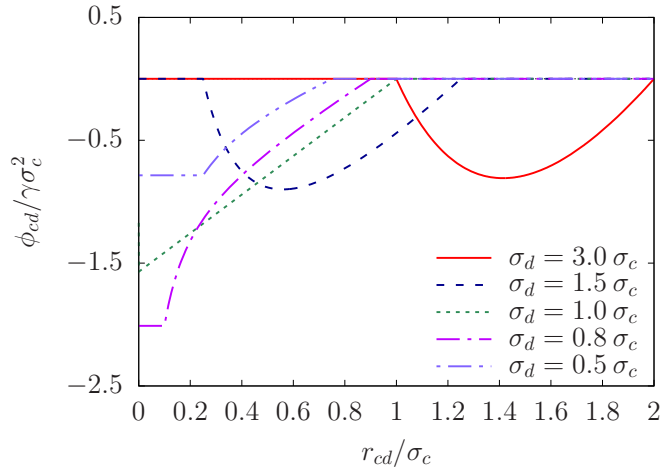


**Figure 3.5.:** Janus colloid-droplet pair potential scaled by the oil-water interfacial tension  $\gamma$  is shown as a function of the scaled distance  $r_{cd}/\sigma_c$  for size ratios  $\sigma_d/\sigma_c = 3.0, 1.5, 1.0, 0.8, 0.5$  (from right to left).

Similarly to the previous study of Schwarz *et al.* [13], we assume that the colloid-water interfacial tension is equal to the colloid-droplet interfacial tension,  $\gamma_{co} = \gamma_{cw}$ , so that  $\theta_{ow} = 90^\circ$ . This assumption is reasonable since a change in the contact angle seems to not have an influence on the final outcomes [14]. In addition, we neglect the influence of the adsorbed colloid on the oil-water interfacial curvature such that the droplet remains spherical.

The evaporation of the dispersed oil droplet implies that the droplet diameter is initially larger and eventually smaller than the colloid diameter. In order to mimic this situation, the colloid-droplet potential  $\phi_{cd}(r)$  is given as follows

If  $\sigma_d > \sigma_c$ ,

$$\phi_{cd}(r) = \begin{cases} -\gamma\pi\sigma_d h & \frac{\sigma_d - \sigma_c}{2} < r < \frac{\sigma_d + \sigma_c}{2} \\ 0 & \text{otherwise,} \end{cases} \quad (3.10)$$

and if  $\sigma_d < \sigma_c$ ,

$$\phi_{cd}(r) = \begin{cases} -\gamma\pi\sigma_d^2 & r < \frac{\sigma_c - \sigma_d}{2} \\ -\gamma\pi\sigma_d h & \frac{\sigma_c - \sigma_d}{2} < r < \frac{\sigma_c + \sigma_d}{2} \\ 0 & \text{otherwise,} \end{cases} \quad (3.11)$$

with  $\gamma_{ow}$  abbreviated to  $\gamma$  and  $h$  being the height of the spherical cap that results from the colloid-droplet intersection (see Fig. 3.4) given by

$$h = \frac{(\sigma_c/2 - \sigma_d/2 + r)(\sigma_c/2 + \sigma_d/2 - r)}{2r}. \quad (3.12)$$

Figure 3.5 shows the colloid-droplet pair potential plotted against the scaled distance for several different ratios of the droplet diameter and colloid diameter.

### 3.2.4. Total interaction energy

The total interaction energy  $U_{\text{tot}}$  is the sum of Janus colloid-colloid, droplet-droplet, and Janus colloid-droplet interactions,

$$\frac{U_{\text{tot}}}{k_{\text{B}}T} = \sum_{i < j}^{N_c} \phi_{cc}(\mathbf{r}_{ij}, \hat{\mathbf{n}}_i, \hat{\mathbf{n}}_j) + \sum_{i < j}^{N_d} \phi_{dd}(|\mathbf{R}_i - \mathbf{R}_j|) + \sum_i^{N_c} \sum_j^{N_d} \phi_{cd}(|\mathbf{r}_i - \mathbf{R}_j|), \quad (3.13)$$

where  $N_c, N_d$  are the number of colloids and droplets, respectively;  $(\mathbf{r}_i, \hat{\mathbf{n}}_i)$  and  $(\mathbf{r}_j, \hat{\mathbf{n}}_j)$  is the center-of-mass coordinate and the unit vector locating the attractive patch of colloid  $i$  and colloid  $j$ , respectively;  $\mathbf{R}_i$  is the center-of-mass coordinate of droplet  $i$ .

### 3.2.5. Simulation method

The mixture of Janus colloids and droplets is simulated in the  $NVT$  ensemble using the kinetic Monte Carlo method. All simulation parameters are described in detail in the following tables. In Tab. 3.1 we show the parameters of the pair interaction potentials. The parameters of the binary mixture and of the kinetic Monte Carlo simulation are summarized in Tabs. 3.2 and 3.3, respectively.

The simulations are performed in a cubic box with periodic boundary conditions. For a given set of parameters, statistical data is collected by running 20 independent simulations and averaging. In each run, a maximum trial displacement and rotation step of colloids and droplets are set small enough (see Tab. 3.3) such that the Monte Carlo (MC) simulation is approximately equivalent to Brownian dynamics, as discussed in Sec. 2.2. The time evolution of the system is therefore described by the number of MC cycles per particle. In each MC cycle, we attempt to move each particle once on average. The droplets shrink at a constant rate and vanish completely half-way through the simulation. Differently from Schwarz's work [13], the kinetic pathway is simply simulated without taking account of the collective motion of particles in the cluster, e.g. collective translational and rotational cluster moves. Such collective modes of motion are significantly involved in dense colloidal systems with interparticle attractive interactions that vary strongly with distance or angle [126, 127].

To initialize our simulation, the Janus colloids are distributed randomly outside droplets, i.e.  $r > (\sigma_c + \sigma_d)/2$ , and the minimum separation between Janus colloids is larger than one bond length,  $\sigma_c + \Delta$  (two Janus colloids form a bond if their distance is smaller than  $\sigma_c + \Delta$ ). Hence, no two Janus colloids form a bond in the initial stage of the simulation. We use the following definition of a cluster: a cluster is a set of Janus colloids that are connected with each other by bonds. Each cluster is therefore described by both the number of bonds,  $n_b$ , and the number of Janus colloids,  $n_c$ , belonging to this cluster. Although the definition of  $n_b$  is insufficient to distinguish a variety of different structures (isomers), especially for clusters of large sizes, it is considered an important indicator of the compactness of the cluster [13]. The cluster criterion and the detailed algorithm for searching clusters are described in Appx. A.1.

**Table 3.1.:** Summary of parameters of the pair interaction potentials used in the computer simulations

Physical quantity	Description
$\epsilon_{\text{sw}} = 9 k_{\text{B}}T$	square-well depth
$\Delta = 0.09 \sigma_c$	square-well width
$k = 10 \sigma_c^{-1}$	inverse Debye length
$\epsilon_{\text{Y}} = 24.6 k_{\text{B}}T$	Yukawa repulsion strength
$r_{\text{cut}} = 2.5 \sigma_c$	cut-off radius
$\gamma = 100 \frac{k_{\text{B}}T}{\sigma_c^2}$	oil-water interfacial tension

**Table 3.2.:** Parameters used for the mixture of droplets and colloids

Physical quantity	Description
$N_c = 500$	number of Janus colloids
$N_d = 7 - 35$	number of droplets
$\eta_c = 0.01 - 0.05$	colloid volume packing fraction
$\eta_d = 0.15$	droplet volume packing fraction
$\sigma_c = 1$	colloid diameter
$\sigma_d(0) = 6\sigma_c$	initial droplet diameter

**Table 3.3.:** Parameters used for the kinetic Monte Carlo simulation

Physical quantity	Description
$d_c = 0.01\sigma_c$	maximum trial displacement of colloid
$r_c = 0.01\text{rad}$	maximum trial rotation of colloid
$d_d = d_c \sqrt{\sigma_c/\sigma_d}$	maximum trial displacement of droplet
$n = 10^6$	number of Monte Carlo cycles per particle
$a = \frac{\sigma_d(0)}{2n}$	shrinking amplitude <sup>a</sup>

<sup>a</sup> The shrinking amplitude is chosen in such a way that the droplets vanish completely after  $n/2$ .

### 3.3. Results and discussion

#### 3.3.1. Dynamics of cluster formation

In the kinetic Monte Carlo simulation, one can determine the physical time corresponding to each MC step. Here we calculate approximately the physical time per MC step via the translational diffusion coefficient of clusters  $D_{\text{cls}}$  because this quantity provides a relationship between the mean square displacement of particles and the simulation time.

According to the Einstein equation [128]

$$\lim_{n \rightarrow \infty} \frac{\langle \Delta r_{\text{cls}}^2(n) \rangle}{n} = 6D_{\text{cls}}\tau, \quad (3.14)$$

where  $n$  is the number of MC cycles and  $\tau$  is the physical time per MC cycle. Here,  $\langle \Delta r_{\text{cls}}^2(n) \rangle$

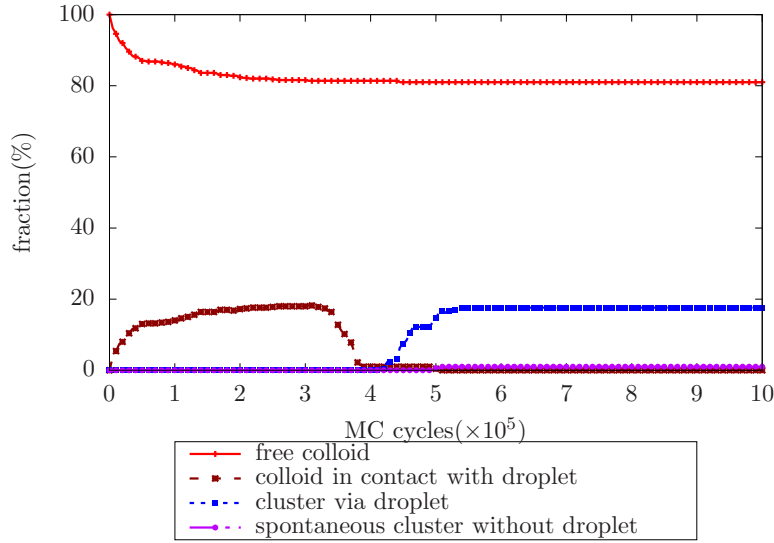


**Figure 3.6.:** Fraction of colloids in the different states as a function of the MC time at  $\eta_c = 0.03$ ,  $\eta_d = 0.15$ ,  $\sigma_d(0) = 6\sigma_c$  and  $\chi = 1/2$ . A very low fraction of colloids that were in bonds but then becomes free is not shown.

is the mean square displacement of clusters after  $n$  cycles, defined as

$$\langle \Delta r_{\text{cls}}^2(n) \rangle = \frac{1}{N_{n_c}} \sum_{i=1}^{N_{n_c}} (\Delta \mathbf{r}_{\text{cls},i}(n))^2, \quad (3.15)$$

where  $N_{n_c}$  is the number of clusters with  $n_c$  colloids and  $\Delta \mathbf{r}_{\text{cls},i}(n)$  is the center-of-mass displacement of a cluster with  $n_c$  colloids after  $n$  cycles. In addition, the time required for a cluster to diffuse over its diameter  $\sigma_{\text{cls}}$  is the so-called Brownian time scale  $\tau_B$  given by  $\tau_B = \sigma_{\text{cls}}^2 / D_{\text{cls}}$  with an assumption that the diameter of the spherical cluster  $\sigma_{\text{cls}} = \sqrt[3]{n_c} \sigma_c$ . Hence, we have

$$\frac{n\tau}{\tau_B} \simeq \frac{\langle \Delta r_{\text{cls}}^2(n) \rangle}{6 \sqrt[3]{n_c^2} \sigma_c^2}. \quad (3.16)$$

From Eq. (3.16) the physical time that corresponds to the MC simulation time ranges from tens to hundreds of  $\tau_B$  depending on the number of colloids in the cluster. Using the Stokes-Einstein equation for diffusion of spherical particles,  $D_{\text{cls}} = \frac{k_B T}{3\pi\eta\sigma_{\text{cls}}}$ , with  $\eta$  the viscosity of the solvent. For example, for the clusters composed of ten colloids with diameter of 154 nm in water ( $\eta = 1 \text{ mPa}\cdot\text{s}$ ) at room temperature,  $\tau_B \sim 0.85 \text{ s}$ . Compared to experimental time scales of the clusters that typically last tens of minutes [10, 13], our estimated MC simulation time scales are much smaller and hence do not address the realistic long-time dynamics in the experiments. However, as mentioned previously in the experimental and simulation study [13, 129], despite a lack of time scales the model of single colloids reproduces qualitative and quantitative agreement with experimental results.

During the dynamic process of cluster formation, a Janus colloid typically proceeds through several possible states: (i) the colloid is free, (ii) the colloid is trapped on the droplet surface, but does not yet form a bond with another colloid, (iii) the colloid is trapped at the interface and

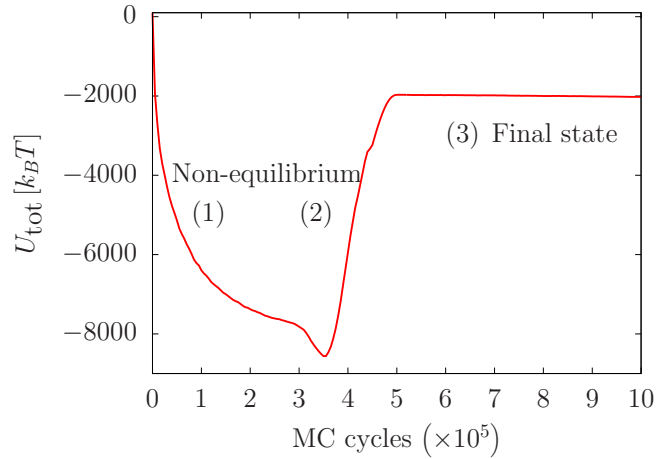


**Figure 3.7.:** Total energy of the system as a function of Monte Carlo time at  $\eta_c = 0.03$ ,  $\eta_d = 0.15$ ,  $\sigma_d(0) = 6\sigma_c$  and  $\chi = 1/2$ . Curves with label (1) and (2) show non-equilibrium states of the system at early stage of the simulation, whereas the line labeled (3) shows that the system reaches a stable final state after  $5 \times 10^5$  MC cycles.

forms a bond with other colloids on the droplet surface, (iv) the colloid forms bonds spontaneously to another colloid without involvement of any droplets, and (v) the colloid was bonded but then becomes free. Figure 3.6 shows the fraction of colloids corresponding to each of the above states as a function of the MC time. Starting from the initial configuration of free colloids (red line), the number of free colloids decreases gradually until all droplets vanish completely after  $5 \times 10^5$  MC cycles. At the same time, the number of colloids belonging to clusters increases (blue line). After that time, both types of colloids stay at a constant fraction. In the final stage of the simulation, the total yield of clusters is nearly 20%. In addition, the number of spontaneously formed clusters has a small fraction of roughly 1% (black line). This result comes from the fact that the distance between two Janus colloids in the initial configuration is larger than the bond length, therefore in order to form one bond Janus colloids have to obtain a thermal energy which is larger than the repulsive energy barrier  $9k_B T$ . In practice, the corresponding probability is so small that we find only a very low fraction of doublets but not larger clusters [13].

The dynamical evolution of the system is also checked by monitoring the total energy  $U_{\text{tot}}$  as a function of the Monte Carlo time. Figure 3.7 shows how the total energy of the system varies with respect to the number of Monte Carlo cycles at  $\eta_c = 0.03$ ,  $\eta_d = 0.15$ ,  $\sigma_d(0) = 6\sigma_c$  and  $\chi = 1/2$ . Starting from the nearly zero initial value,  $U_{\text{tot}}$  decrease steadily to the minimum value (the curve line labeled (1) in Fig. 3.7), which corresponds to a continuous capturing of colloids at the droplet surface. The minimum value  $U_{\text{tot}}$  indicates that the number of colloids trapped at the droplet surface may be maximized (or saturated) after about  $3.6 \times 10^5$  MC cycles. At the next stage, when the droplet diameter becomes smaller than the colloid diameter, some colloids are no longer confined to the droplet surface and therefore do not possess the adsorption energy due to the Pickering effect. As a consequence, the total energy of the system increases until all the droplets vanish completely after  $5 \times 10^5$  (the line labeled (2) in Fig. 3.7). Later, the total energy reaches a constant value, showing that the system is in a stable final state (the line labeled (3) in Fig. 3.7).

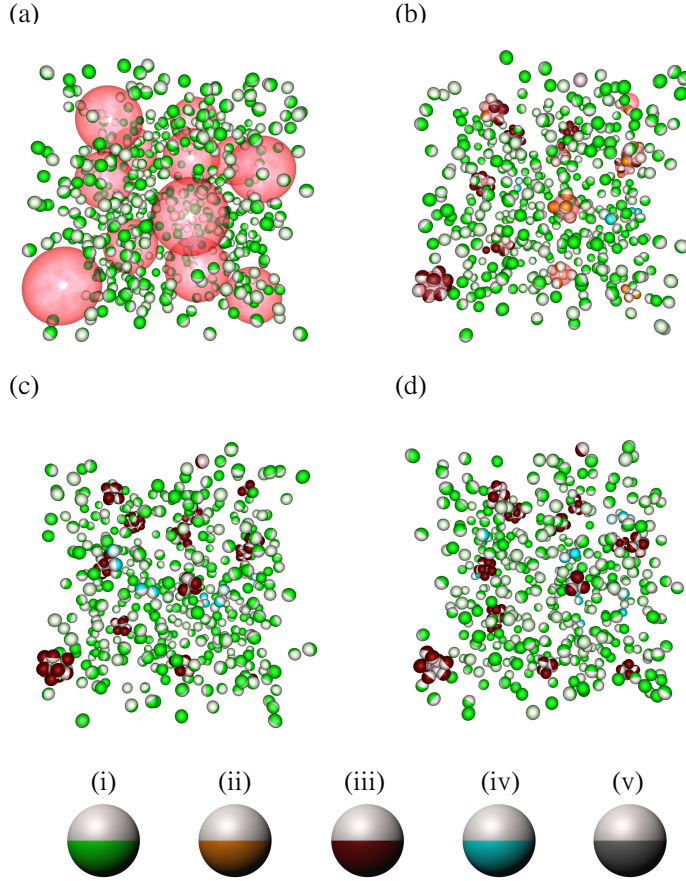


**Figure 3.8.:** Representative snapshots of simulation system with  $\eta_c = 0.03$ ,  $\eta_d = 0.15$ ,  $\sigma_d(0) = 6\sigma_c$  and  $\chi = 1/2$  at different stages of the time evolution (a) initial configuration (b) after  $3.25 \times 10^5$  MC cycles (c) after  $5 \times 10^5$  and (d) after  $10^6$  MC cycles. Droplets are shown as pink spheres. Differently colored spheres (as indicated) are used to describe the state of Janus colloid: (i) a free Janus colloid, (ii) a Janus colloid trapped at the droplet surface (iii) a Janus colloid trapped forming a bond with others via droplet (iv) a Janus colloid forming a bond with others without via droplet (v) a Janus colloid breaking a bond.

Figure 3.8 shows some typical snapshots of the simulated system at four different stages of the time evolution. The initial configuration consists of non-overlapping spheres of both the Janus colloids and the large (pink) droplets [Fig. 3.8(a)]. After  $3.25 \times 10^5$  MC cycles many Janus colloids are trapped at the droplet surface [red colloidal spheres in Fig. 3.8(b)]. After  $5 \times 10^5$  MC cycles the droplets completely vanish and the Janus colloids assembly into clusters [Fig. 3.8(c)]. At the end of the simulation, i.e. after  $10^6$  MC cycles, the presence of all clusters formed via the droplets demonstrates the stability of the clusters against thermal fluctuations [Fig. 3.8(d)].

We further investigate the assembly of the Janus colloid particles into clusters via droplet evaporation by means of the radial distribution functions (RDFs) of colloid-droplet,  $g_{cd}(r)$ , and colloid-colloid pairs,  $g_{cc}(r)$ . We consider these RDFs at different stages of the time evolution ranging from  $t_1$  to  $t_6$ , corresponding to given numbers of MC cycles (see Tab. 3.4). As shown in Fig. 3.9 and Tab. 3.4,  $g_{cd}(r)$  between times  $t_1$  and  $t_5$  has one prominent peak that is located at the instantaneous droplet diameter  $\sigma_d(t)/2$ . This peak results from colloids that are captured at the droplet surface. Due to the shrinking of the droplet diameter, the peak is shifted steadily towards shorter separations. In addition, an increase of the peak height of  $g_{cd}(r)$  in MC time

demonstrates that the number of Janus colloids captured at the droplet surface may increase in time. Finally, after  $t = t_6$  ( $5 \times 10^5$  MC cycles) the droplets vanish completely, and therefore  $g_{cd}(r)$  gives unphysical behavior. At the same time, the colloid-colloid RDF  $g_{cc}(r)$  shows a transition from an effectively ideal gas state (after  $0.8 \times 10^5$  MC cycles) to a fluid state with some degree of short-ranged orders outside the square-well region (after  $4.0 \times 10^5$  MC cycles). The presence of short-ranged orders at distances larger than  $\sigma + \Delta$ , as shown in Fig. 3.10, indicates that clusters have formed. This observation agrees with visual inspection of simulation snapshots.

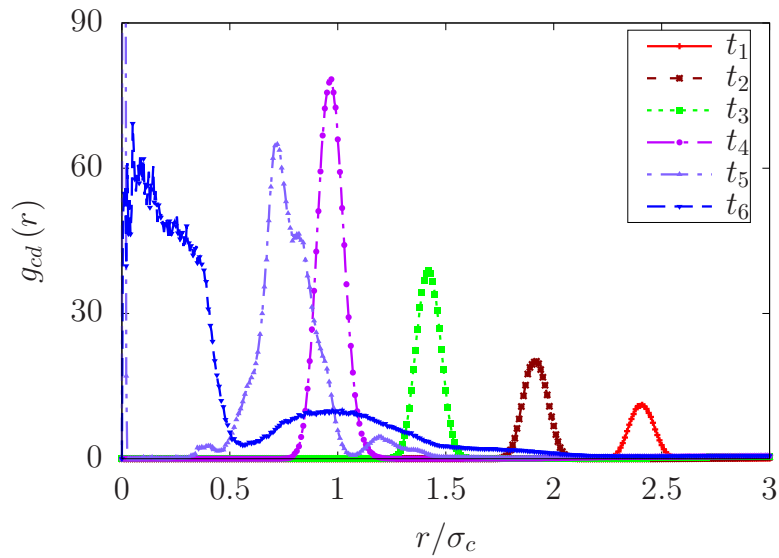


**Figure 3.9.:** Colloid-droplet radial distribution function as a function of the scaled distance  $r/\sigma_c$  at different stages of the computer simulation. The peak position of  $g_{cd}(r)$  together with an explanation for times  $t_i$  are given in Tab. 3.4.

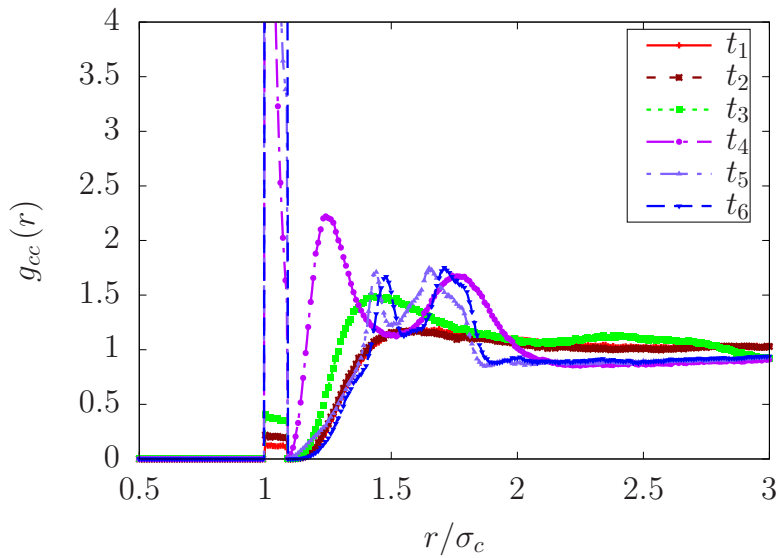


**Figure 3.10.:** Colloid-colloid radial distribution functions plotted against the scaled distance  $r/\sigma_c$  at different stages of the simulation. See the notation for times  $t_i$  in Tab. 3.4.

**Table 3.4.:** The variation of peak positions of  $g_{cd}(r)$ ,  $g_{cc}(r)$  radial distribution functions and droplet diameter as a function of the time evolution for  $\sigma_d(0) = 6\sigma_c$ .

$i$	$t_i$ ( $\times 10^5$ MC cycles)	Peak position ( $r/\sigma_c$ )			$\sigma_d(t)/\sigma_c$
		$g_{cd}(r)$	$g_{cc}(r)$		
1	0.8	2.42	$1.05 \pm 0.04^a$	$\sim^b$	4.8
2	1.6	1.91	$1.05 \pm 0.04$	$\sim$	3.8
3	2.4	1.41	$1.05 \pm 0.04$	$\sim$	2.8
4	3.2	0.90	$1.05 \pm 0.04$	$1.25^c$ 1.77	1.8
5	4.0	$\approx 0.65$	$1.05 \pm 0.04$	1.43 1.73	1.2
6	5.0	$  ^d$	$1.05 \pm 0.04$	1.47 1.72	0.0

<sup>a</sup> Peak within square-well region

<sup>b</sup> Ideal gas state

<sup>c</sup> Short-ranged order

<sup>d</sup> Undefined value

### 3.3.2. Packing of small clusters $n_c \leq 6$

**Surface coverage**  $\chi = 1/2$

First, we analyze the packing of small clusters with a number of constituent spheres in the range  $n_c = 2 - 6$  for the colloid packing fraction  $\eta_c = 0.03$ ,  $\sigma_d(0) = 6\sigma_c$  and for the Janus limit case  $\chi = 1/2$ . The clusters obtained are shown in Fig. 3.11. Except for a chain-like structure [Fig. 3.11(b)], all clusters have the same configuration as those observed previously in the self-assembly of amphiphilic Janus colloids [96]. Here we obtain cluster sizes  $n_c$  between 2 (dumbbell), 3 (triplet), 4 (tetrahedron), 5 (triangular dipyramid) and 6 (octahedron), which have familiar structures of small molecules such as diatomic fluorine, boron trifluoride, carbon tetrafluoride, phosphorus pentafluoride, and sulfur hexafluoride, respectively [9]. Furthermore, the unique packing of these cluster structures also minimizes the second moment of the mass distribution  $M_2$ , defined as

$$M_2 = \sum_{i=1}^{n_c} |\mathbf{r}_i - \mathbf{r}_{\text{cm}}|^2, \quad (3.17)$$

where  $\mathbf{r}_i$  is the position of the center of sphere  $i$  and  $\mathbf{r}_{\text{cm}}$  is the center of mass of a given cluster structure. In Figs. 3.11(c)-(e), the cluster structure is identical to the geometric solution of the Thomson and Tammes problem at low values of  $n_c$  ( $n_c \leq 6$ ). The objective of the Thomson problem is to find the minimal electrostatic energy configuration of  $n_c$  identical point charges on a spherical surface [130], whereas the Tammes problem is a problem in the arrangement of  $n_c$  spheres on the spherical surface such that the minimum distance between spheres is maximized, or equivalently the area density of spheres on the spherical surface is maximized [131].

**Surface coverage**  $\chi = 1/4$

For the case of Janus colloid with the surface coverage  $\chi = 1/4$  some additional structures are found, including a chain-like structure for  $n_c = 4$  and square dipyramid for  $n_c = 5$  (see Fig. 3.12).

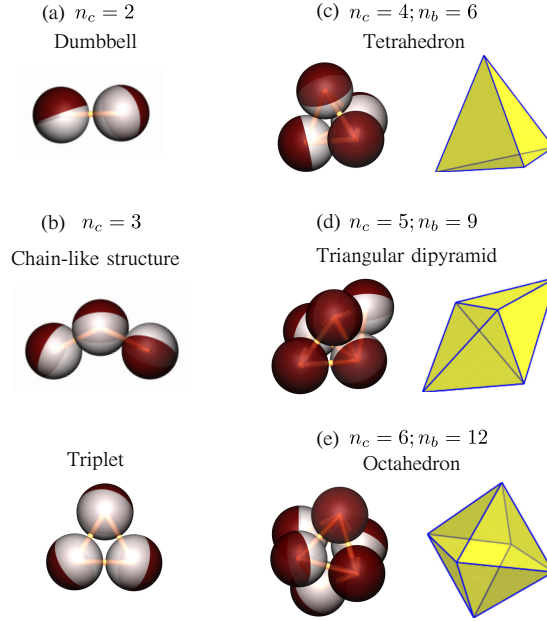


**Figure 3.11.:** Cluster configurations for  $n_c = 2 - 6$  and corresponding bond number  $n_b$  obtained in the final stage of the simulation for  $\sigma_d(0) = 6\sigma_c$ ,  $\eta_c = 0.03$  and  $\chi = 1/2$ . Clusters found for (a) dumbbell, (b) chain-like structure and triplet, (c) tetrahedron, (d) triangular dipyramid, (e) octahedron. The white and red hemispheres represent the attractive and repulsive parts, respectively. The rightmost column of clusters with  $n_c > 3$  shows polyhedra formed by connecting the center of each colloid to its nearest neighbors. The wireframe inside the cluster structure illustrates the bond formed by a pair of colloidal spheres.

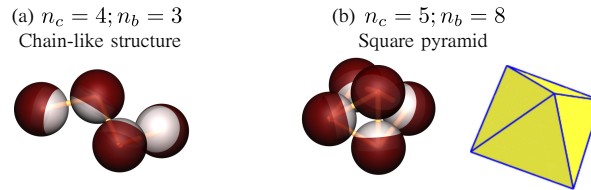


**Figure 3.12.:** Similar to Fig. (3.11), but for  $\chi = 1/4$ . Here, we show only the additional structures that are not found at  $\chi = 1/2$ : (a) chain-like structure, (b) square dipyramid.

### Stacked Histograms

We obtain a cluster size distribution by using a stacked histogram of the number of clusters with a given cluster size. In Fig. 3.13, each bar corresponds to the cluster size  $n_c$  ( $n_c \leq 6$ ) and is divided into differently colored regions with a relative height which is proportional to the number of clusters with  $n_b$  bonds. The total height of bars indicates the number of cluster  $N_{n_c}$  with  $n_c$  Janus colloids. In the case of  $\chi = 1/4$  [ Fig. 3.13(a)], two distinguishable isomers are found for  $n_c = 3, 4$  and  $5$ , while only one isomer is found for  $\chi = 1/2$  (except for  $n_c = 3$ ).

### 3.3.3. Packing of large clusters

Next, our focus is on larger clusters ( $6 < n_c \leq 12$ ) where a new variety of sphere packings occurs. These are members of a unfamiliar set of highly symmetric polyhedra, some of which have not been yet reported in previous studies of evaporation-driven assembly of colloidal particles.

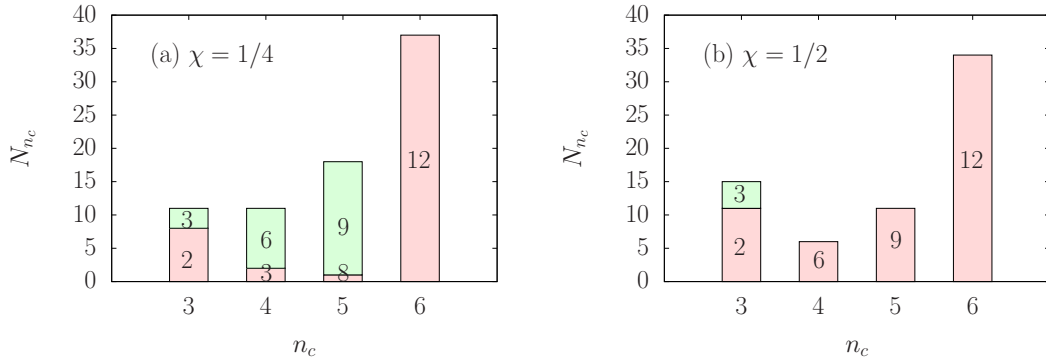


**Figure 3.13.:**  $N_{n_c}$  denotes the number of clusters with  $n_c$  Janus colloids. The total height of column indicates  $N_{n_c}$ . Each column is divided in differently colored regions in a such way that the each height is proportional to the number of clusters with  $n_b$  bonds. Each region is labeled with the bond number. The  $n_c = 2$  bar whose height is larger than 200 is not shown for clarity. (a) Results for  $\chi = 1/4$  and (b) Results for  $\chi = 1/2$  at  $\eta_c = 0.03$ ,  $\eta_d = 0.15$ ,  $\sigma_d(0) = 6\sigma_c$ .

#### Clusters for $n_c = 7$

Figure 3.14 shows clusters for  $n_c = 7$  obtained for two different values of the surface coverage,  $\chi = 1/4$  (left) and  $\chi = 1/2$  (right). As shown in Fig. 3.14(a), we find two isomers; one is a unique  $M_2$ -minimal pentagonal dipyramid (PD) and the other an augmented triangular prism (ATP). The ATP is constructed by augmenting a triangular prism by attaching a square pyramid to one of its equatorial faces. Interestingly, ATP clusters have been observed previously in colloidal clusters from aerosol droplets [19] but not from water-in-oil [17] and oil-in-water emulsions [18]. Furthermore, in our simulations PD and ATP clusters has nearly the same fraction at  $\chi = 1/4$ .

At a higher value of the surface coverage,  $\chi = 1/2$ , we also observe two isomeric clusters, i.e. an octahedron-plus-one and a PD where the fraction of PD clusters is smaller than that of octahedron-plus-one clusters. Note also that the octahedron-plus-one clusters can be decomposed into a tetrahedron and a triplet, and thus may be found in close-packed lattices [9, 132].

Comparison of the bond number  $n_b$  of clusters for  $\chi = 1/4$  and  $\chi = 1/2$  reveals a slightly higher value of  $n_b$  found in the latter case, resulting from a lower potential energy of clusters (see Fig. 3.14).

#### Clusters for $n_c = 8$

As shown in Fig. 3.15, for 8-sphere clusters we observe one isomeric structure of a square antiprism configuration ( $\chi = 1/4$ ) and one  $M_2$ -minimal snub disphenoid configuration ( $\chi = 1/2$ ). The snub disphenoid was commonly found in many preceding studies of colloidal assemblies driven by evaporation [9, 13, 14, 18], whereas the square antiprism, formed by two regular tetramers lying in parallel planes with one being twisted relative to the other by  $45^\circ$ , is less frequent than the snub disphenoid according to Cho *et al.* [17]. The authors believe that electrostatic repulsion between the colloidal particles in water droplets caused formation of their square antiprism clusters [17, 19]. The square antiprism configuration has been observed for clusters, which were prepared from toluence-in-water emulsion, by Wittmann and co-workers [12]. Very recently, Demirörs *et*

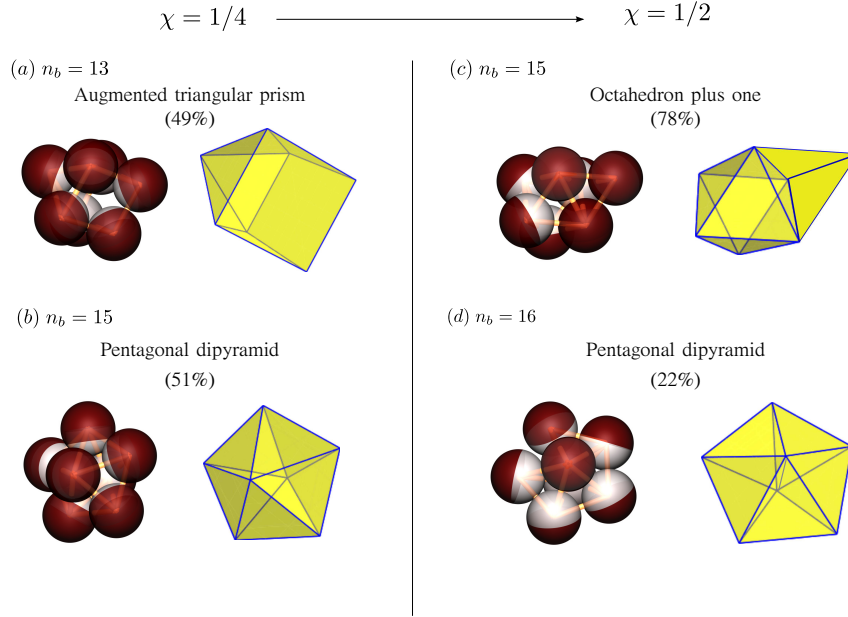


**Figure 3.14.:** Configuration of clusters for  $n_c = 7$  at  $\eta_c = 0.03$ ,  $\eta_d = 0.15$ ,  $\sigma_d(0) = 6\sigma_c$ .  $\chi = 1/4$  (left) and  $\chi = 1/2$  (right) surface coverage are shown. For each  $\chi$ , two isomers of Janus colloid packings are found: (a) augmented triangular prism (b) pentagonal dipyramid with  $n_b = 15$  (c) octahedron plus one (d) pentagonal dipyramid with  $n_b = 16$ . The percentage of clusters corresponding to each surface coverage is shown below each cluster name.

*al.* [133] have reported square antiprism clusters in an experimental and simulation study of long-ranged oppositely charged colloidal particles. These results indicate that cluster configurations even at low  $n_c$  depend strongly on both the surface properties of colloidal particles and on the interparticle potential.

#### Clusters for $n_c = 9$

For  $n_c = 9$ , see Fig. 3.16, there is only a  $M_2$ -minimal isomeric structure of triaugmented triangular prism (TTP) configuration found for both  $\chi = 1/4$  and  $\chi = 1/2$ . As the name suggests, TTP can be constructed by attaching square pyramids to each of three equatorial faces of the triangular prism. However, there is a slight deviation in the bond number of the TTP

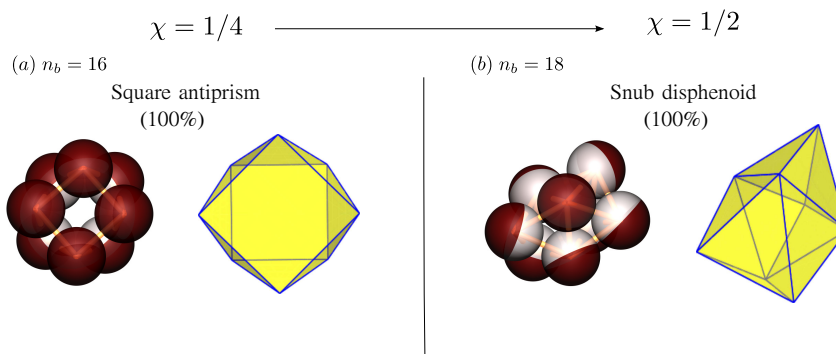


**Figure 3.15.:** Same as Fig. 3.14, but for  $n_c = 8$ . For each  $\chi$ , one isomer is found: (a) square antiprism (b) snub disphenoid.

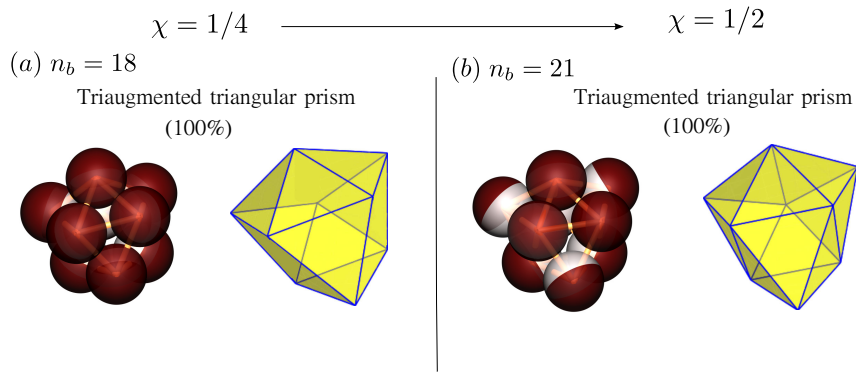


**Figure 3.16.:** For  $n_c = 9$  only one isomer of triaugmented triangular prism with the bond number (a)  $n_b = 18$  and (b)  $n_b = 21$  is obtained for two values of  $\chi = 1/4$  and  $\chi = 1/2$ , respectively.

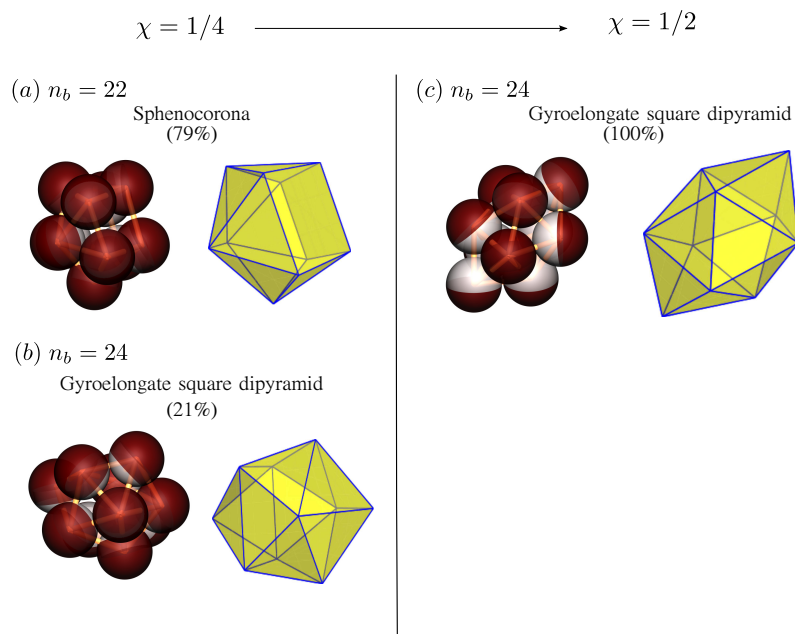


**Figure 3.17.:** Clusters containing  $n_c = 10$  particles belong to two distinct configurations at  $\chi = 1/4$  (left) (a)  $n_b = 22$  (sphenocorona) (b)  $n_b = 24$  (gyroelongate square dipyramid) and at  $\chi = 1/2$  (right) only gyroelongate square dipyramid structure (c)  $n_b = 24$ .

structure between two cases of  $\chi$ . More specifically, three bonds are missing in the TTP cluster at  $\chi = 1/4$  [Fig. 3.16(a)] compared to that of  $\chi = 1/2$  [Fig. 3.16(b)].

#### Clusters for $n_c = 10$

Similarly to 7-sphere clusters, in Fig. 3.17(a), for  $n_c = 10$  and at  $\chi = 1/4$ , we find two different isomers: sphenocorona ( $n_b = 22$ ) and  $M_2$ -minimal isomeric structure of gyroelongate square dipyramid configuration ( $n_b = 24$ ) with fraction of 79% and 21%, respectively. To our best knowledge, there is no report about sphenocorona clusters in the literature. At a larger value of  $\chi$ , i.e  $\chi = 1/2$ , there remains only the gyroelongate square dipyramid structure, as shown in Fig. 3.17(b).

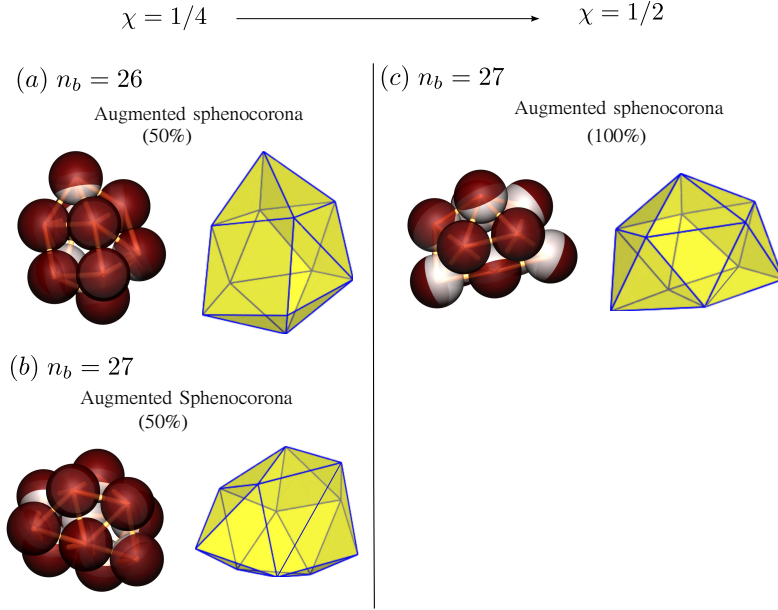


**Figure 3.18.:** Clusters containing  $n_c = 11$  particles (augmented sphenocorona) but having a slight difference in the bond number  $n_b$ . Results are shown at  $\chi = 1/4$  (a)  $n_b = 26$ , (b)  $n_b = 27$  and at  $\chi = 1/2$  (c)  $n_b = 27$ .

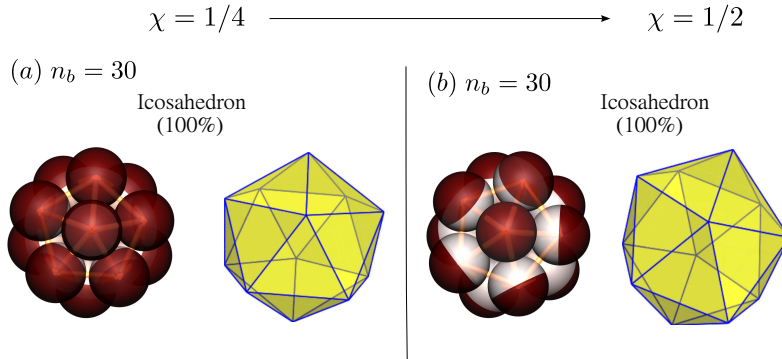


**Figure 3.19.:** Unique cluster of icosahedra found in both cases (a)  $\chi = 1/4$  and (b)  $\chi = 1/2$ .

#### Clusters for $n_c = 11$

Figure 3.18 shows the clusters with  $n_c = 11$  at  $\chi = 1/4$  (left) and  $\chi = 1/2$  (right). We obtain the unique structure of an augmented sphenocorona configuration with the bond number  $n_b = 26$  [Fig. 3.18(a)] and  $n_b = 27$  [Figs. 3.18(b)-(c)]. This structure belongs to a convex polyhedron, which is very similar to that of icosahedron-minus-one [13, 17] configuration but different from a non-convex polyhedral configuration in previous studies [9, 16].

#### Clusters for $n_c = 12$

For 12-sphere clusters only one unique icosahedron configuration with the bond number  $n_b = 30$  is observed in both cases of  $\chi = 1/4$  and  $\chi = 1/2$ . In fact, the icosahedral symmetry in which all sphere positions are equivalent is known to have an optimal configuration in both the Tammes and the Thomson problem.

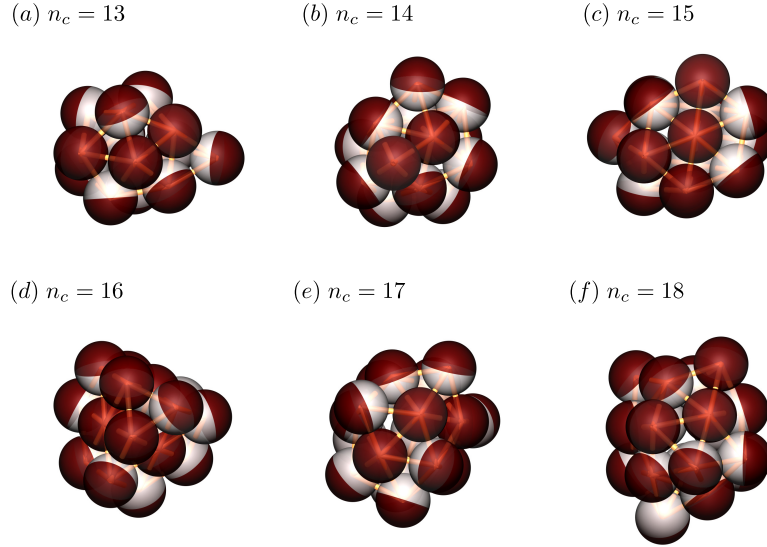


**Figure 3.20.:** Typical clusters found for  $n_c \geq 13$  at  $\eta_c = 0.05$ ,  $\eta_d = 0.15$ ,  $\sigma_d(0) = 6\sigma_c$  and  $\chi = 1/2$ .

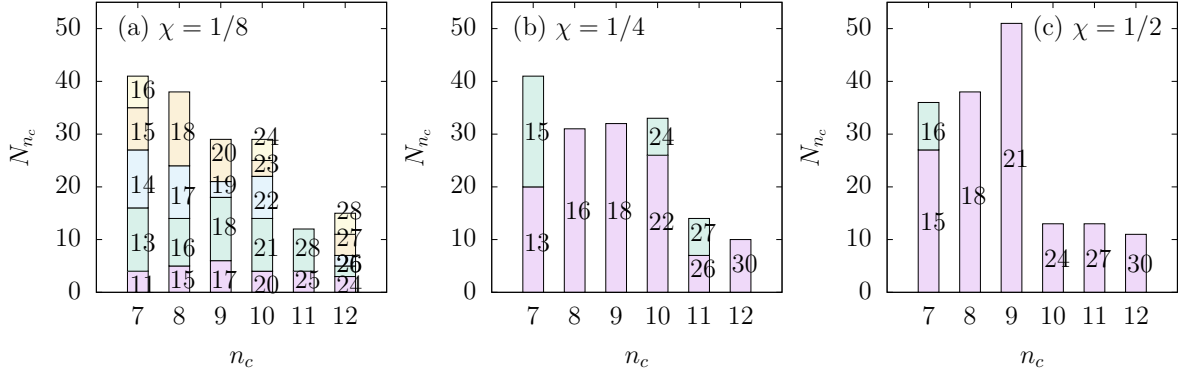


**Figure 3.21.:** Same as Fig. 3.13, but for cluster size  $7 \leq n_c \leq 12$ . Results are shown at (a)  $\chi = 1/8$ , (b)  $\chi = 1/4$  and (c)  $\chi = 1/2$ .

Larger clusters can be obtained by increasing the initial droplet diameter or colloid volume packing fraction. Figure 3.20 shows the typical cluster structures with  $n_c = 13 - 18$  obtained at  $\eta_c = 0.05$ ,  $\eta_d = 0.15$ ,  $\sigma_d(0) = 6\sigma_c$  and  $\chi = 1/2$ . In practice, it is difficult to identify the geometric symmetry of large  $n_c$ -polyhedra if using only the number of constituent colloids and bond number of isomers. Therefore, the analysis of the large size clusters ( $n_c \geq 13$ ) are skipped in this work.

### Stacked histograms

The stacked histograms of the number of clusters as a function of the cluster size ( $7 \leq n_c \leq 12$ ) are shown in Fig. 3.21. For  $\chi = 1/8$  we find a variety of isomers with different bond numbers. However, for  $\chi = 1/4$  only two distinct isomers of 7-, 10-, 11-sphere clusters and one isomer of 8-, 9-, 12-sphere clusters are observed. In particular, for  $\chi = 1/2$ , all the clusters (except for the 7-sphere cluster) have a unique configuration with larger average bond numbers compared to the cases  $\chi = 1/8$  and  $\chi = 1/4$ . Intuitively, this can be explained as follows: an increase of the repulsive part of the Kern-Frenkel potential due to a decrease of  $\chi$  leads to a difficult equilibration process of the cluster geometry.

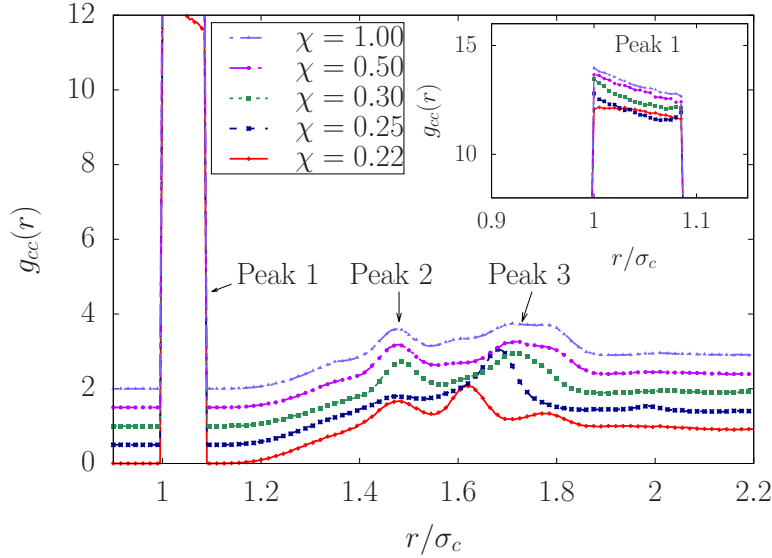


**Figure 3.22.:** Colloid-colloid radial distribution functions  $g_{cc}(r)$  as a function of the scaled distance  $r/\sigma_c$  at  $\eta_c = 0.03, \eta_d = 0.15, \sigma_d(0) = 6\sigma_c$  in the final stage of the computer simulations. Results are shown at different surface coverages  $\chi$  (as indicated). Curves are shifted upwards by 0.5 units for clarity. The inset shows a magnified view of peak 1.

### Colloid-colloid radial distribution functions

The compactness of clusters under the influence of the surface coverage  $\chi$  can further be characterized by means of the colloid-colloidal radial distribution function  $g_{cc}(r)$ . Figure 3.22 shows  $g_{cc}(r)$  in the final stage of the simulation for several different  $\chi$  values. It can be seen that the colloid-colloid radial distributions exhibit a pronounced peak (labeled peak 1) of width  $\Delta$  (recall that  $\Delta$  is the square-well width) at a short distance around  $r = \sigma_c$ , indicating a large degree of bonding between the colloids formed at this distance. In addition, as  $\chi$  increases the bond number of clusters increases slightly, signaled by a larger peak height as shown in a magnified view of this peak (see inset of Fig. 3.22). These results are in good agreement with our results for stacked histograms, as discussed above.

For clarity curves are shifted upwards by 0.5 units in Fig. 3.22.  $g_{cc}(r)$  shows two additional distinct peaks labeled peak 2 and peak 3 which correspond to the second and third nearest-neighbor distance of clusters, respectively. In particular, differently from the fixed positions of peak 1 and peak 2, the position of peak 3 shifts continuously towards larger distances with an increase of  $\chi$  in the range of 0.22–0.30. The peak 3 then keeps a nearly fixed position as  $\chi \geq 0.30$ . From this analysis, we believe that a structural transformation of clusters probably occurs at  $\chi$  around 0.30.

### 3.3.4. Orientational order parameter of clusters

As the cluster configurations are in equilibrium in the final stage of the simulations, the constituent Janus colloids align in such a way that their attractive patches face each other in order to minimize the total potential energy. We employ an orientational order parameter that was used in a classification of self-assembled structures of patchy colloidal dumbbells [134, 135],

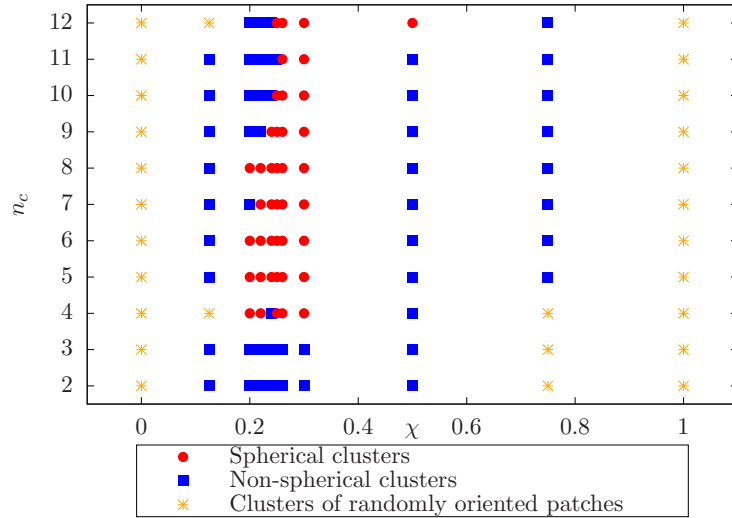


**Figure 3.23.:** State diagram of Janus colloidal clusters of size  $n_c$  as a function of surface coverage  $\chi$  at the final stage of the simulation for  $\eta_c = 0.03, \eta_d = 0.15, \sigma_d(0) = 6\sigma_c$ .

defined as

$$\mathcal{M} = \left\langle \frac{1}{n_c} \sum_{i=1}^{n_c} \hat{\mathbf{n}}_i \cdot \frac{\mathbf{r}_{\text{cm}} - \mathbf{r}_i}{|\mathbf{r}_{\text{cm}} - \mathbf{r}_i|} \right\rangle, \quad (3.18)$$

where the angular brackets denote an average over all clusters that are composed of  $n_c$  constituent colloids,  $\hat{\mathbf{n}}_i$  is the unit vector pointing in the direction of the attractive patch of colloid  $i$ ,  $\mathbf{r}_i$  is the center of mass of colloid  $i$  and  $\mathbf{r}_{\text{cm}} = (\sum_{i=1}^{n_c} \mathbf{r}_i)/n_c$  is the center of mass of the cluster. For a perfectly spherical cluster, i.e. all directional vectors of Janus colloids belonging to the cluster point towards the center of the cluster, we have  $\mathcal{M} = 1$ . If clusters have  $\mathcal{M} \geq 0.9$  we consider them as spherical (marked with a solid colored circle). Otherwise, if any cluster has  $0.5 \leq \mathcal{M} < 0.9$  we consider it to be a non-spherical cluster (elongated cluster) and mark with a blue colored square. Finally, clusters of  $\mathcal{M} < 0.5$  are considered as having randomly oriented patches (depicted by an orange asterisk).

Using the order parameter of clusters, we map out the state diagram for Janus colloids in the surface coverage  $\chi$ -cluster size  $n_c$  representation, as shown in Fig. 3.23. We find a narrow region of  $\chi$  in the range  $0.20 - 0.30$  in which spherical clusters are favored, and a broader region of non-spherical clusters when  $\chi$  is outside of this range. The clusters of randomly oriented patches are found when  $\chi$  is larger than  $0.8$  or smaller than  $0.2$ . Of the cluster states observed, the spherical and non-spherical clusters that can be regarded as micelles are interesting because they are found, on smaller length scales, in the chemistry of surfactant molecules and the physical biology of the cell [123]. Additionally, a high value of the order parameter corresponds to a highly restricted rotation for individual Janus colloids in the cluster. For this reason, we plot  $\mathcal{M}$  as a function of  $\chi$  in order to determine the value of  $\chi$  at which maximizes  $\mathcal{M}$  (see Fig. 3.24). It can be seen that the order parameter  $\mathcal{M}$  exhibits a maximum value for  $\chi$  from  $0.22$  to  $0.25$  for all clusters with different sizes. The  $\chi$  values in this range are in accordance with  $\chi$  that exhibit the structural transformation as above discussed in Sec. 3.3.3.

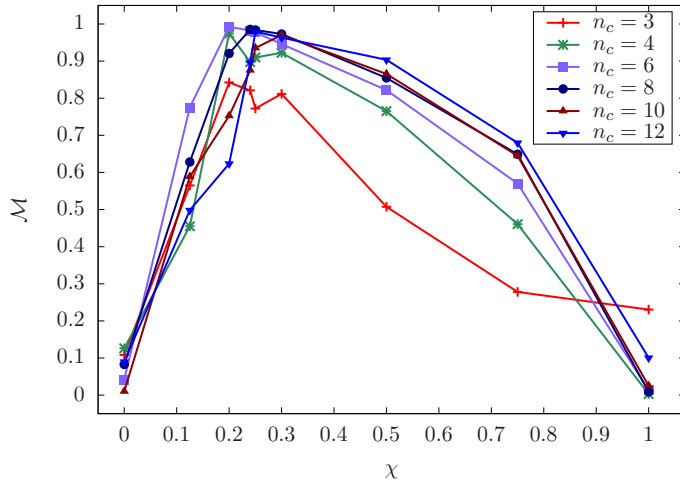


**Figure 3.24.:** Order parameter of  $n_c$ -sphere clusters as a function of surface coverage  $\chi$  for  $\eta_c = 0.03, \eta_d = 0.15, \sigma_d(0) = 6\sigma_c$ .

Recall that the isomers for  $n_c = 7$  ( $n_b = 13$ ),  $n_c = 10$  ( $n_b = 22$ ) and  $n_c = 11$  ( $n_b = 26$ ) are members of a set of convex polyhedra that do not minimize the second moment of the mass distribution. Comparison of  $\mathcal{M}$  for two  $n_c$ -isomers, as given in Tab. 3.5, shows that  $\mathcal{M}$  of  $M_2$ -nonminimal isomers is slightly larger than that of  $M_2$ -minimal isomers at the same surface coverage  $\chi = 1/4$ . Therefore, we suppose that the formation of new  $M_2$ -nonminimal isomeric clusters is directly related to the maximization condition for the order parameter  $\mathcal{M}$ .

### 3.3.5. Effect of Janus colloid packing fraction on cluster size distribution

The cluster size distribution depends not only on the initial droplet diameter but also on the colloid packing fraction. Hence we investigate the normalized number of clusters,  $N_{n_c}/\sum N_{n_c}$  (with  $\sum N_{n_c}$  being the total number of clusters), as a function of the number of constituent colloids  $n_c$ . Figure 3.25 shows the cluster size distribution for several different colloid packing fractions. A subsequent increase in the colloid packing fraction, from Figs. 3.25(a) to (d), leads to a decrease in the yield of small sized clusters, or equivalently a yield increase of larger clusters. At the same time the cluster distribution becomes broader. This can be explained by a higher probability of capturing the colloids on the droplet surface when the colloid density increases. Additionally, there is no considerable difference in the cluster size distribution between the two cases  $\chi = 1/4$  and  $\chi = 1/2$ , which is a direct consequence of the strong short-ranged attraction between the Janus colloids.

### 3.3.6. Hierarchical assembly: Superclusters

In this section, we investigate the assembly process into hierarchical superstructures in a mixture of droplets and one of types of building blocks: dumbbell, triangular and tetrahedral clusters of Janus colloids. The clusters of colloidal dumbbells via droplet evaporation will be separately described in Chap. 4. To generate the initial configurations we start by randomly distributing the colloidal triangular clusters in the cubic simulation box and with random orientations. The

**Table 3.5.:** The value of the orientational order parameter of clusters  $\mathcal{M}$  for two isomers with  $n_c = 7, 10$  and 11 at  $\chi = 1/4$ . See the illustration of these isomers in Figs. 3.14, 3.17 and 3.18.

$n_b \backslash n_c$	13	16
7	$0.981 \pm 0.008$	$0.976 \pm 0.012$
$n_b \backslash n_c$	22	24
10	$0.935 \pm 0.053$	$0.900 \pm 0.036$
$n_b \backslash n_c$	26	27
11	$0.921 \pm 0.046$	$0.889 \pm 0.051$

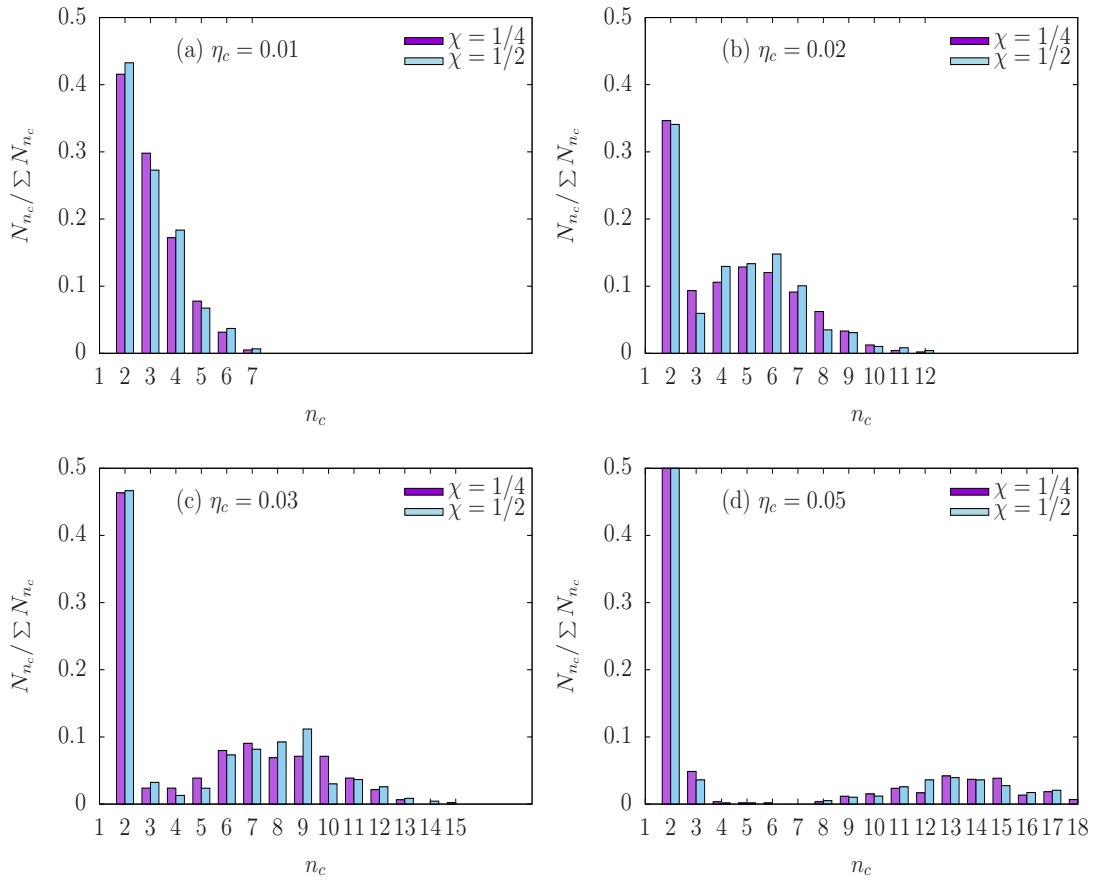


**Figure 3.25.:** Normalized cluster size distribution,  $N_{n_c} / \sum N_{n_c}$ , as a function of the number of colloids in the cluster  $n_c$  at  $\sigma_d(0) = 6\sigma_c$  and  $\eta_d = 0.15$ . Results are shown for different colloid packing fractions (a)  $\eta_c = 0.01$  (b)  $\eta_c = 0.02$  (c)  $\eta_c = 0.03$  and (d)  $\eta_c = 0.05$ , the  $n_c = 2$  bar height is about 0.65.

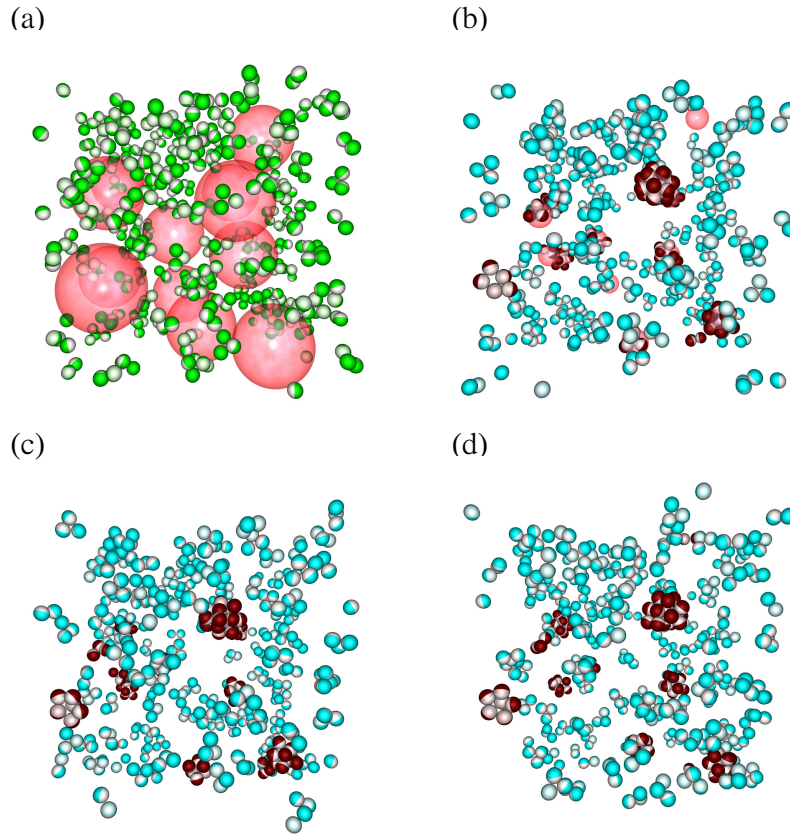


**Figure 3.26.:** Snapshots of the simulation system consisting of triangular clusters and emulsion droplets at  $\eta_c = 0.03$ ,  $\eta_d = 0.15$ ,  $\sigma_d(0) = 6\sigma_c$  and  $\chi = 1/2$  at different stages of the time evolution (a) initial configuration (b) after  $3.25 \times 10^5$  MC cycles (c) after  $5 \times 10^5$  and (d) after  $10^6$  MC cycles. Droplets are shown as pink spheres, while the Janus colloids are represented by different colors as described in Fig. 3.8.

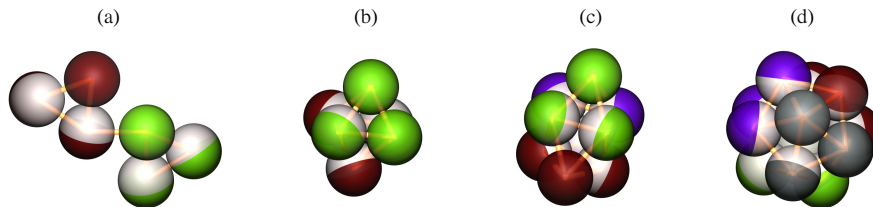


**Figure 3.27.:** Superclusters formed by initial triangular clusters for  $\chi = 1/2$ ,  $\eta_c = 0.03$ ,  $\eta_d = 0.15$ ,  $\sigma_d(0) = 6\sigma_c$ . Colloids with the same color belong to the same initial triangular building block. (a) Chain-like structure (b) octahedron (c) triangulated triangular clusters composed of three triangular clusters and (d) icosahedron composed of four triangular clusters.

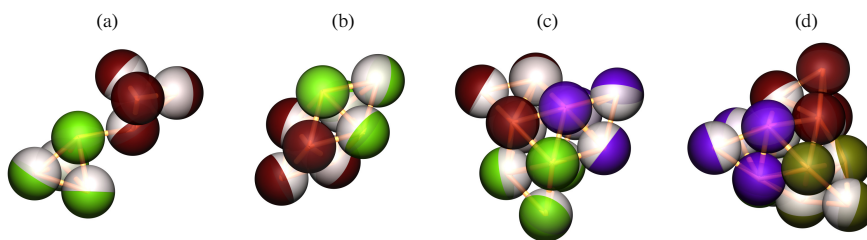


**Figure 3.28.:** Same as Fig. 3.27 but for initial tetrahedral clusters (a) Chain-like structures (b) elongated triangular dipyrmaid (c) supercluster composed of three tetrahedra, and (d) supercluster composed of four tetrahedra.

initial distance between colloids in a triangular cluster is smaller than one bond length (i.e.  $\sigma + \Delta$ ). In contrast, the initial distance between colloids that belongs to different triangular clusters is larger than one bond length. As a consequence, no two triangular clusters bind together in the initial stage of the simulation. In addition, all colloids are initially located outside of droplets (see Appx. A.2). All simulation parameters are kept the same as that of single colloids.

Figure 3.26 shows snapshots of the simulation system at different stages of the time evolution. In the initial configuration [Fig. 3.26(a)], only the droplets and triangular clusters are present in the system. After  $3.25 \times 10^5$  MC cycles, as shown in Fig. 3.26(b), the pink large droplets have shrunk and simultaneously trapped several triangular colloidal clusters at their surface. We indicate the state of each colloid a corresponding color (same as in Fig. 3.8). Figure 3.26(c) and (d) show the configurational snapshots after  $5 \times 10^5$  MC cycles when all the droplets completely vanish and after  $10^6$  MC cycles (final stage of the simulation), respectively. We obtain complex superclusters that consist of triangular colloidal clusters and are stable against thermal fluctuations on the time scale of the simulation.

The typical supercluster structures obtained in the simulations for a set of parameters (given in the caption) are shown in Fig. 3.27. In Figs. 3.27(a) and (b), two distinct structures consisting of two triangular building blocks are found; one is chain-like (open structure), the other is a familiar octahedral cluster. The cluster of triaugmented triangular prism configuration formed by three building blocks and of icosahedron configuration formed by four building blocks are shown in Figs. 3.27(c) and (d), respectively. So, the hierarchical assembly of triangular clusters does not generally produce new cluster structures, except for the chain-like structure, as compared to that made of single colloids.

Similarly, we carried out simulations for a mixture of tetrahedral clusters and emulsion droplets. Figure 3.28 shows typical structures at  $\chi = 1/2, \eta_c = 0.03, \eta_d = 0.15, \sigma_d(0) = 6\sigma_c$ . Shown in Fig. 3.28(a) is a chain-like structure formed by two tetrahedra. This structure is very similar to that shown in Fig. 3.27(a). We find elongated triangular dipyrmaid clusters [Fig. 3.28(b)] composed of two tetrahedra rotated by  $30^\circ$  against each other and with two touching faces. Figure 3.28(c) and 3.28(d) show the superstructures composed of three and of four tetrahedra, respectively. Such superstructures have geometry structures that are completely different from the compounds of uniform tetrahedra [136].

In addition, different from the single colloidal clusters that possess several  $n_c$  isomers available depending on the attractive surface coverage, we observe only a unique  $n_c$ -superstructure. This can be explained by the fact that a strong bonding between the colloids of triangular/tetrahedral clusters in the initial configuration significantly restricts the displacement of particles during the dynamic process of supercluster formation.

### 3.4. Conclusions

We have investigated the hierarchical assembly of Janus colloidal particles via emulsion droplet evaporation by means of Metropolis-based kinetic Monte Carlo simulations. We employed the Yukawa potential to model a long-ranged repulsion, and the square-well potential modulated by

the direction-dependent Kern-Frenkel potential to model an anisotropic short-ranged attraction between the colloids. The colloid-droplet interaction is aimed at modeling the Pickering effect in a such way that the colloids cannot escape from the droplet surface by thermal agitation. The droplet-droplet interaction is hard-core potential with an increased distance to ensure that no two droplets can be bridged by a colloid.

To mimic experimental evaporation-driven assembly, the droplet diameter decreases at a fixed rate in the simulation. Meanwhile, droplets can capture Janus colloids at their surface during the dynamic process, resulting in a non-equilibrium system. We therefore performed the computer simulations with sufficiently small displacement of particles to ensure that the kinetic Monte Carlo simulation mimics the results of Brownian dynamics.

The dynamic pathway of the cluster formation were analyzed by means of radial distribution functions together with direct visual inspection of configurations. In the final stage of the simulation, we observe a majority of clusters formed via emulsion droplets and only a very small percentage of dumbbells formed spontaneously. The cluster configurations obtained range from doublets to convex polyhedra. Compared to a familiar set of  $M_2$ -minimal isomers, for the attractive surface coverage  $\chi = 0.5$ , we find some additional isomeric structures at  $\chi = 0.25$ , including the square dipyramid ( $n_c = 5$ ), augmented triangular prism ( $n_c = 7$ ), square antiprism ( $n_c = 8$ ), sphenocorona ( $n_c = 10$ ) and augmented sphenocorona ( $n_c = 11$ ). In particular, colloid-colloid radial distribution functions show that an isomeric transformation from  $M_2$ -minimal clusters to unique  $M_2$ -nonminimal clusters occurs when  $\chi$  is smaller than 0.3. A further decrease of  $\chi$  below 0.2 gives more isomers with a smaller number of bonds, i.e. with more open clusters, as a direct result of the difficulty of equilibration of cluster structures in the presence of a strong repulsive part of the Kern-Frenkel potential. This finding, in accordance with previous reports [17, 19], suggests that the formation of  $M_2$ -nonminimal isomers is directly related to the repulsive interaction between colloidal particles.

An orientational order parameter  $\mathcal{M}$  was used to classify the clusters obtained. We found that spherical micelles are only observed in a narrow region of  $\chi$  (0.20-0.30). In addition, for a fixed value of  $\chi$  the order parameter of  $M_2$ -nonminimal isomers is higher than that of  $M_2$ -minimal isomers with the same number of constituent particles. It is therefore plausible to suppose that maximization of the order parameter appears to favor structures that are more spherical.

Histograms shows that cluster size distribution is independent of the surface coverage as a direct result of a strong short-ranged attraction between colloids. Additional, larger clusters can be obtained by increasing the colloid packing fraction.

Further investigation of the cluster formation of a mixture of tetrahedral clusters via emulsion droplets shows that compact superstructures can be obtained from a specific number of building blocks. Such superstructures are identical to those assembled by tetrahedral clusters of isotropic colloids [13] except for the chain-like structure. Besides, we did not find any new structure assembled by triangular clusters than those made of single colloids.

## Chapter 4.

# Assembly of open clusters of colloidal dumbbells via droplet evaporation<sup>1</sup>

### 4.1. Introduction

Assembly of anisotropic colloidal particles controlled via interparticle interactions or geometric shapes has given rise to a rich variety of novel structures of colloidal materials as well as unusual phase equilibria [40, 137]. Of many available categories of anisotropic building blocks, colloidal dumbbells composed of two connected colloidal spheres, have attracted considerable attention because the aspect ratio, size, interaction potential and asymmetric functionalization properties of two constituent colloidal spheres can be easily manipulated by experiments [11, 138–145]. The self-assembly of colloidal dumbbells has been widely studied in both computer simulations and experiments, revealing the spontaneous formation of crystal structures [146, 147], micelles [134], vesicles [135], bilayers [134, 148, 149]. Other investigations of the phase behavior of colloidal dumbbells have shown that even hard dumbbells exhibit a complex phase diagram [146, 150–155]. For example, Singer and Mumaugh first observed a transition from a fluid phase to a stable plastic crystal phase for small aspect ratios [152]. At higher densities and aspect ratios, the plastic crystal phase transforms into a fully ordered crystal phase. A further increase of the aspect ratio leads to an aperiodic crystal phase possessing long-range positional order yet lacking any defined periodicity [146, 153–155]. In the case of square-well dumbbells that involves both repulsive and attractive interactions, the structure and phase behavior strongly depends not only on their size, aspect ratio but also the strength of attractive interactions [148, 149, 156–159]. Chapela and Alejandre reported that the micellization process of heterogeneous vibrating square-well dumbbells occurs at a relative diameter ratio between particles of 1/2 and relative depth ratio of the interacting potential of 4 in both the liquid and vapor phases, indicating a simultaneous presence of the micellization and the phase separation. Besides, the nucleation process [160] and the structural properties of hard dumbbells under the effect of the oscillatory shear [161], and gravity [162] have been already reported.

In contrast to the large body of work to understand the crystal structure and the phase behavior of colloidal dumbbells, little work has been done to describe the process of cluster formation as well as cluster structures. In particular, open clusters of colloidal dumbbells with syndiotactic,

---

<sup>1</sup>Selections from this chapter have been reprinted with permission from our study [129]. Copyright 2016, American Physical Society.

chiral [163], and stringlike structures [164] are significant because they can be used as building blocks for bottom-up fabrications of novel materials with unique magnetic, optical and rheological properties [5]. Skelton [165] investigated the cluster formation of Janus dumbbells via the desorption of a polymeric stabiliser. This procedure, which is supported by simulations based on a constraint of surface area minimization, leads to supracolloidal structures such as dimers, trimers, tetramers, and pentamers. The evaporation technique of emulsion droplets pioneered by Velev *et al.* [106–108] has been widely used to prepare clusters of monodispersed colloidal particles [9–13, 15, 16] (see more detail in Section 3.1) and bidispersed colloidal particles [18]. These authors [18] found that the interparticle interaction and the wettability of the constituent spheres play an important role in the surface coverage of the smaller particles. In addition, the minimization of the second moment of the mass distribution ( $M_2$ ) only applies if the size ratio is less than 3. Recently, Peng *et al.* [30] reported both experimental and simulation work on the cluster formation of dumbbell-shaped colloids. These authors proved that the minimization of the second moment of the mass distribution is not generally true for anisotropic colloidal dumbbell self-assembly. However, they predicted cluster structures without considering the different wettabilities for constituent colloidal spheres.

In this chapter, we extend the model of Schwarz [13] to investigate the cluster formation of colloidal dumbbells with asymmetric properties in either size or wetting induced by emulsion droplet evaporation. By varying the relative size of two spherical colloids and/or their interfacial tension with the droplets, we obtain a rich variety of complex cluster structures with the open or intermediate structures that have not yet been observed in experiments and computer simulations. Such structures could lead to novel hierarchically organized structures. This chapter is organized as follows. In Sec. 5.2 we give the details of the pair interaction and the simulation method. We analyze the cluster formation, structures, and size distributions for dumbbells with asymmetric wetting properties in Sec. 4.3.1. The results were featured in our publication [129]. In addition, we complement a detailed analysis for dumbbells with asymmetric sizes in Sec. 4.3.2 in order to show that uniqueness of compact structures is lost when the size ratio between the large- and small-sized spheres is larger than 1.2. Conclusions are given in Sec. 4.4.

## 4.2. Model and simulation method

### 4.2.1. Colloid-colloid pair interaction

A sketch of the model for two colloidal dumbbells is shown in Fig. 4.1. Each dumbbell is composed of two spherical colloids, labeled colloidal species 1 and colloidal species 2, of diameter  $\sigma_1$  and  $\sigma_2$  ( $\sigma_1 \geq \sigma_2$ ), respectively. The colloids in each dumbbell are separated from each other by a distance that vibrates in the range of  $\lambda \leq l \leq \lambda + \Delta$ , where  $\lambda = (\sigma_1 + \sigma_2)/2$ . Such a colloidal dumbbell is called the heteronuclear (or homonuclear when  $\sigma_1 = \sigma_2$ ) vibrating colloidal dumbbell [157].

The colloid-colloid pair interaction includes a short-ranged attraction and a Yukawa electrostatic repulsion. For the colloidal dumbbells, two colloidal species may have different sizes. Thus,

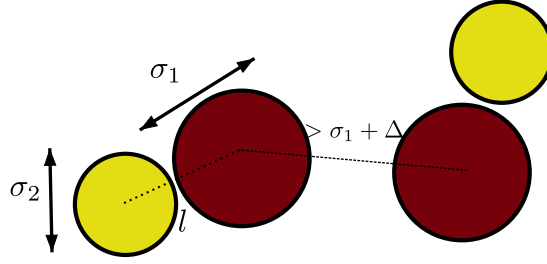


**Figure 4.1.:** Sketch of the model of colloidal dumbbells composed of two species (red and yellow spheres). Shown are the diameters of colloidal species 1,  $\sigma_1$ , colloidal species 2,  $\sigma_2$ . In the initial stage of the simulation, the colloid 1–colloid 2 distance in the same dumbbell is  $l$ , whereas the initial distance between two any colloids belonging to different dumbbells is set to larger than  $\sigma_1 + \Delta$ .

the colloid–colloid pair interaction can be expressed by three equations

$$\phi_{11}(r) = \begin{cases} \infty & r < \sigma_1 \\ -\epsilon_{\text{SW}} & \sigma_1 < r < \sigma_1 + \Delta \\ \epsilon_Y \sigma_1 \frac{e^{-\kappa(r-\sigma_1)}}{r} & \text{otherwise,} \end{cases} \quad (4.1)$$

$$\phi_{22}(r) = \begin{cases} \infty & r < \sigma_2 \\ -\epsilon_{\text{SW}} & \sigma_2 < r < \sigma_2 + \Delta \\ \epsilon_Y \sigma_2 \frac{e^{-\kappa(r-\sigma_2)}}{r} & \text{otherwise,} \end{cases} \quad (4.2)$$

and

$$\phi_{12}(r) = \begin{cases} \infty & r < \lambda \\ -\epsilon_{\text{SW}} & \lambda < r < \lambda + \Delta \\ \epsilon_Y \lambda \frac{e^{-\kappa(r-\lambda)}}{r} & \text{otherwise,} \end{cases} \quad (4.3)$$

where  $\phi_{11}$ ,  $\phi_{12}$ , and  $\phi_{22}$  are the colloid 1–colloid 1, colloid 1–colloid 2, and colloid 2–colloid 2 pair interactions, respectively;  $\epsilon_{\text{SW}}$ ,  $\Delta$  are the depth and the width of the short-ranged attractive square well, respectively;  $\epsilon_Y$ ,  $\kappa$  are parameters to control the strength and range of the Yukawa repulsion, respectively;  $r$  is the center–center distance of particles.

Figure 4.2 shows colloid–colloid interaction potentials as a function of the scaled distance for a given set of parameters used in the simulations (given in the caption of Fig. 4.2). In principle, the strength of the attractive interaction is chosen so that physical bonds between colloids at the end of evaporation are irreversible. At the same time the repulsive barrier is chosen to be large enough to hinder spontaneous clustering. A wide range of simulation parameters satisfies the above conditions without qualitatively affecting the final results. The potential shape illustrated in Fig. 4.2 is very similar to that used in Ref. [166] to study the stability of nanoparticle shells. Experimentally, these parameters can be tuned via the surface potential, concentration of electrolyte and charges of particles [166].

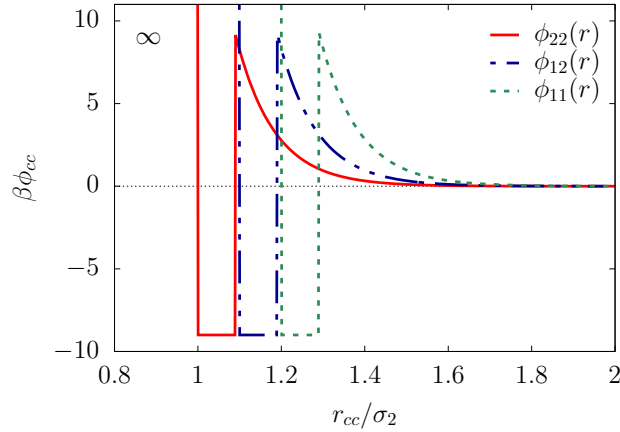


**Figure 4.2.:** Illustration of the pair interactions between two colloidal spheres with  $\epsilon_{\text{SW}} = 9k_{\text{B}}T$ ,  $\Delta = 0.09\sigma_2$ ,  $\epsilon_{\text{Y}} = 24.6k_{\text{B}}T$ ,  $\kappa\sigma_2 = 10$ , and  $\sigma_1 = 1.2\sigma_2$ .

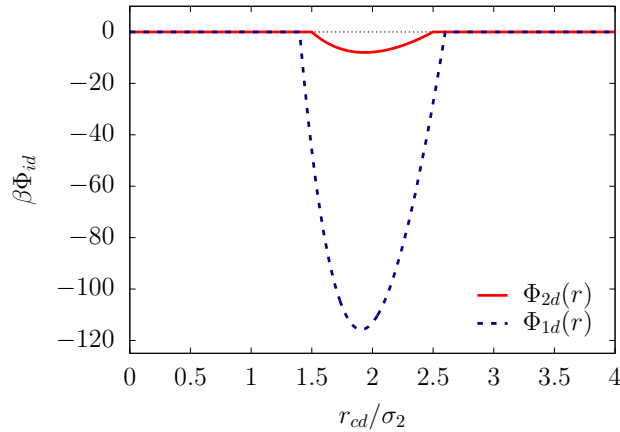


**Figure 4.3.:** Illustration of the colloid-droplet pair interactions at  $\sigma_d(t) = 4\sigma_2$  with  $\sigma_1 = 1.2\sigma_2$ ,  $\gamma_1 = 100k_{\text{B}}T/\sigma_2^2$  and  $\gamma_2 = 10k_{\text{B}}T/\sigma_2^2$

#### 4.2.2. Droplet-droplet pair interaction

The droplet-droplet pair interaction is a purely hard-sphere potential,

$$\Phi_{dd}(r) = \begin{cases} \infty & r < \sigma_d + \sigma_1 \\ 0 & \text{otherwise,} \end{cases} \quad (4.4)$$

where the droplet diameter  $\sigma_d$  is added to the larger colloid diameter  $\sigma_1$  to ensure that no two droplets can share the same colloid.

#### 4.2.3. Colloid-droplet pair interaction

Similarly to the model described in Chap. 3, the colloid-droplet pair interaction is given by Eqs. (3.10) and (3.11) with a small modification. Since the droplets shrink, their diameter is recorded as a function of time, that is,  $\sigma_d(t)$  may be larger or smaller than that of the colloids. If the diameter of droplets  $\sigma_d$  is larger than that of the colloids  $\sigma_i$ ,  $\sigma_d > \sigma_i$  the colloid-droplet

adsorption energy is

$$\Phi_{id} = \begin{cases} -\gamma_i \pi \sigma_d h & \frac{\sigma_d - \sigma_i}{2} < r < \frac{\sigma_d + \sigma_i}{2} \\ 0 & \text{otherwise,} \end{cases} \quad (4.5)$$

and when  $\sigma_d < \sigma_i$ ,

$$\Phi_{id} = \begin{cases} -\gamma_i \pi \sigma_d^2 & r < \frac{\sigma_i - \sigma_d}{2} \\ -\gamma_i \pi \sigma_d h & \frac{\sigma_i - \sigma_d}{2} < r < \frac{\sigma_i + \sigma_d}{2} \\ 0 & \text{otherwise,} \end{cases} \quad (4.6)$$

where  $i = 1, 2$  labels the two colloidal species in the dumbbell,  $h$  is the height of the spherical cap resulting from the colloid-droplet intersection (see Fig. 3.4) given by

$$h = \frac{(\sigma_i/2 - \sigma_d/2 + r)(\sigma_i/2 + \sigma_d/2 - r)}{2r}. \quad (4.7)$$

The parameter  $\gamma_i$  is the droplet-solvent interfacial tension in order to control the colloid-droplet interaction strength. To characterize for the asymmetric wetting property of the two colloidal species to the droplet we introduce the energy ratio  $k$  defined by

$$k = \frac{\gamma_2}{\gamma_1}. \quad (4.8)$$

A sketch of the colloid-droplet pair potentials for  $k = 0.1$  is given in Fig. 5.2.

#### 4.2.4. Total interaction energy

The system can be regarded as a ternary mixture of  $N_d$  droplets and  $N_c$  colloidal dumbbells formed two colloidal species. Therefore, the total energy is the sum of the colloid 1-colloid 1, colloid 1-colloid 2, colloid 2-colloid 2, colloid 1-droplet, colloid 2-droplet, and droplet-droplet pair interactions

$$\begin{aligned} \frac{U_{\text{tot}}}{k_{\text{BT}}} &= \sum_{i < j}^{N_c} \phi_{11}(|\mathbf{r}_{1i} - \mathbf{r}_{1j}|) + \sum_{i < j}^{N_c} \phi_{22}(|\mathbf{r}_{2i} - \mathbf{r}_{2j}|) + \sum_{i,j}^{N_c} \phi_{12}(|\mathbf{r}_{1i} - \mathbf{r}_{2j}|) \\ &+ \sum_i^{N_c} \sum_j^{N_d} \Phi_{1d}(|\mathbf{r}_{1i} - \mathbf{R}_j|) + \sum_i^{N_c} \sum_j^{N_d} \Phi_{2d}(|\mathbf{r}_{2i} - \mathbf{R}_j|) + \sum_{i < j}^{N_d} \Phi_{dd}(|\mathbf{R}_i - \mathbf{R}_j|), \end{aligned} \quad (4.9)$$

where  $\Phi_{1d}$ ,  $\Phi_{2d}$ , and  $\Phi_{dd}$  are the colloid 1-droplet, colloid 2-droplet and droplet-droplet pair interactions, respectively;  $\mathbf{r}_{1i}$  and  $\mathbf{r}_{2i}$  is the center of mass coordinates of colloid 1 and colloid 2 in dumbbell  $i$ , respectively;  $\mathbf{R}_i$  is the center-of-mass coordinate of droplet  $i$ .

#### 4.2.5. Simulation method

We carry out kinetic Monte Carlo simulation in the canonical ( $NVT$ ) ensemble. Most of simulation parameters are kept fixed as given in Tabs. 3.1, 3.2 and 3.3 of Chap. 3. The relevant

**Table 4.1.:** Simulation parameters of a ternary mixture of colloidal dumbbells and droplets. All the other necessary parameters are kept the same as in Tabs. 3.1 3.2 and 3.3.

Physical quantity	Description
$N_c = 250$	number of colloidal dumbbells
$N_d = 10 - 44$	number of droplets
$\eta_c = 0.01 - 0.05$	colloid volume packing fraction
$\eta_d = 0.10 - 0.15$	droplet volume packing fraction
$\sigma_2 = 1$	diameter of type-2 colloids
$\sigma_d(0) = 8\sigma_2$	initial droplet diameter
$d_c = 0.01\sigma_2$	maximum displacement step of colloids
$d_d = d_c\sqrt{\sigma_2/\sigma_d}$	maximum displacement step of droplets
$\gamma_1 = 100k_B T/\sigma_2^2$	colloid 1-droplet interfacial tension
$\gamma_2 = 10 - 100k_B T/\sigma_2^2$	colloid 2-droplet interfacial tension

parameters that are added or modified for a mixture of colloidal dumbbells are given in Tab. 4.1. For a fixed set of parameters, statistical data are collected by running 30 independent simulations.

The initial random configuration of non-overlapping colloidal particles and droplets is prepared in a cubic box with the periodic boundary condition. The initial distance between the colloid-1 and colloid-2 in the same dumbbell (see Fig. 4.1) is set smaller than  $\lambda + \Delta$ , whereas the initial distance between any colloidal species that belong to different dumbbells is set larger than  $\sigma_1 + \Delta$ . As a result, no two dumbbells bind together in the initial stage of the computer simulation.

We define a bond between two colloidal spheres of type  $i$  and  $j$  when their distance is smaller than or equal to  $(\sigma_i + \sigma_j)/2$ , with  $i, j = 1, 2$ . A cluster is a group of colloidal particles connected with each other by a sequence of bonds. Hence, each cluster is characterized by both the number of bonds  $n_b$  and the number of colloidal particles  $n_c$  belonging to this cluster. Clearly, a single dumbbell can be regarded as a trivial cluster with  $n_c = 2, n_b = 1$ . These trivial clusters will be neglected in the following analysis.

### 4.3. Results and discussion

Since the adsorption energy in the Pickering effect depends on both the wetting property, i.e. the interface tension, and the particle size [124], we investigate the formation and structure of clusters of colloidal dumbbells by varying the relative size of colloidal species and/or their interfacial tension with droplets. In the first part of the section, we give the results for dumbbells with asymmetric wetting properties. Next, the results for dumbbells asymmetric sizes are presented in the second part of the section.

#### 4.3.1. Asymmetric wetting properties and symmetric sizes

In order to investigate the cluster formation from the two colloidal species of dissimilar surface wetting properties, we set the diameter of two colloidal species to be equal,  $\sigma_1 = \sigma_2 = \sigma$ . The

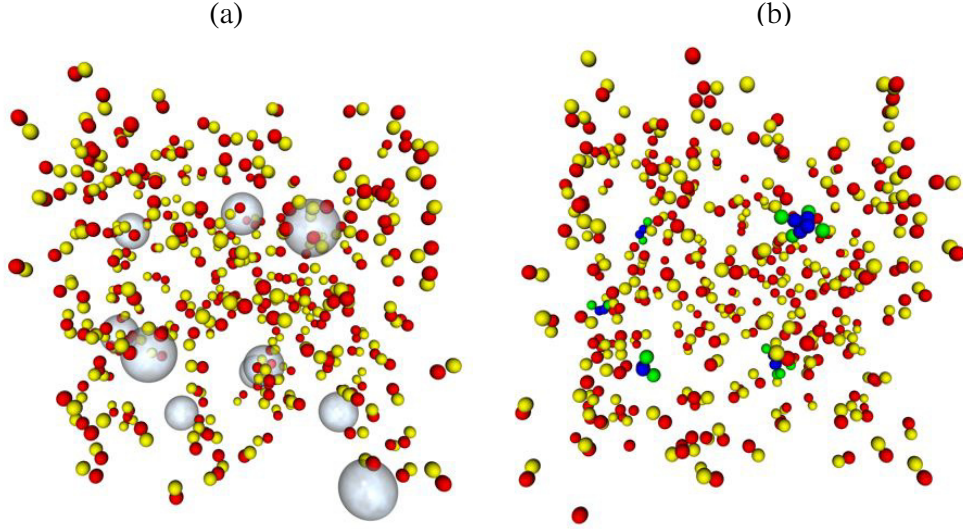


**Figure 4.4.:** Representative snapshots for colloidal dumbbells with symmetric sizes and droplets at the energy ratio  $k = 0.1$ ,  $\eta_c = 0.01$ ,  $\eta_d = 0.1$ ,  $\sigma_d(0) = 8\sigma_c$ . Results are shown at two different stages of the time evolution: (a) after  $2.5 \times 10^5$  MC cycles several colloidal dumbbells (bright yellow and dark red spheres) are trapped at the surface of the droplets (gray spheres); and (b) after  $10^6$  MC cycles the stable clusters that are formed due to the droplets are composed of different colored colloids, that is, blue and green spheres represent colloidal species 1 and colloidal species 2, respectively. Open cluster structures with a compact core by colloid 1 and protruding arms by colloid 2 can be observed. Reproduced with permission [129]. Copyright 2016, American Physical Society.

colloid 1-droplet surface tension  $\gamma_1$  is fixed to  $100k_B T/\sigma^2$ , while colloid 2-droplet surface tension  $\gamma_2$  is varied from  $10k_B T/\sigma^2$  to  $100k_B T/\sigma^2$ . Therefore the energy ratio  $k$  given by Eq. (4.8) ranges from 0.1 to 1. For the special case of  $k = 1$ , colloid-1 and colloid-2 become identical.

Figure 4.4 shows snapshots at two different stages of the simulation for the energy ratio  $k = 0.1$ . In Fig. 4.4(a), several colloidal dumbbells (bright yellow and dark red spheres) are trapped at the surface of the droplets (gray spheres) after  $2.5 \times 10^5$  MC cycles. Figure 4.4(b) shows the final cluster configuration obtained after  $10^6$  MC cycles. Only clusters that are stable against thermal fluctuations survived and are considered for analysis.

#### Colloid-droplet pair interaction functions

We compute the radial distribution functions of colloid 1-droplet,  $g_{1d}(r)$ , and colloid 2-droplet,  $g_{2d}(r)$ , to analyze how colloidal dumbbells are trapped by the droplets. Figure 4.5 shows colloid-droplet radial distributions functions at different stages of the time evolution at  $k = 0.1$  (see Table I for an explanation of the symbols). Between times  $t_1$  and  $t_6$  the function  $g_{1d}(r)$  (solid lines) shows only a single peak. For example, at  $t_1 = 2 \times 10^5$  MC,  $g_{1d}(r)$  has a peak at  $r \simeq 2.25\sigma$  corresponding to the instantaneous droplet radius  $\sigma_d(t)/2$ . The peak is due to colloid-1 spheres trapped at the droplet surface. The droplet radius decreases continuously during the modeled evaporation. As a result, the peak position of  $\sigma_d(t)/2$  shifts continuously towards smaller distances. Moreover, since the number of trapped type-1 colloids onto the droplet surface can increase during the movement of particles, the peak height of  $g_{1d}(r)$  increases with MC time. Finally, after  $t = t_7$  ( $5 \times 10^5$  MC cycles) the droplets vanish completely ( $\sigma_d(t) = 0$ ) and as a result  $g_{1d}(r)$  stops changing.

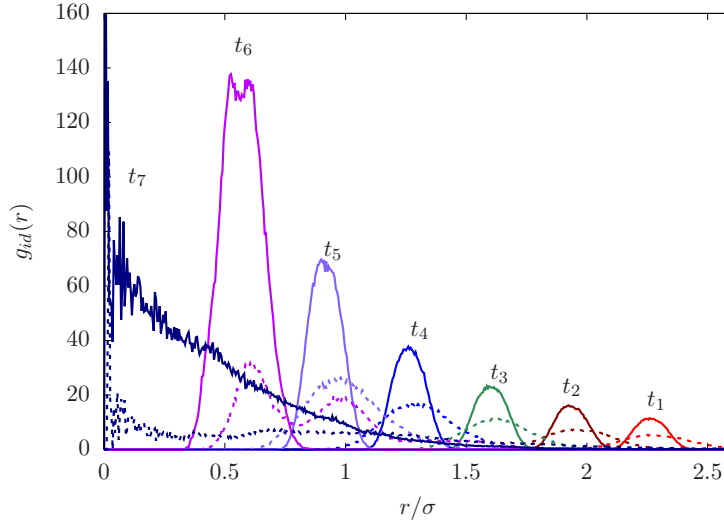


**Figure 4.5.:** Radial distribution functions,  $g_{id}(r)$  ( $i = 1, 2$ ), for colloid 1–droplet (solid lines) and colloid 2–droplet (dashed lines) as a function of the scaled distance  $r/\sigma$  at energy ratio  $k = 0.1$ . Shown are results at different stages of the computer simulation. (See the notation in Tab. 4.2. Reproduced with permission [129]. Copyright 2016, American Physical Society.

A similar trend can be observed in the radial distribution function  $g_{2d}(r)$  (dashed lines in Fig. 4.5). However,  $g_{2d}(r)$  has two distinct peaks at  $t_6 = 4 \times 10^5$  MC cycles. Table 4.2 lists peak positions of  $g_{1d}(r)$ ,  $g_{2d}(r)$  and instantaneous droplet diameter  $\sigma_d(t)$  with respect to the time evolution of the system for  $k = 0.1$ . In addition, for  $k = 0.1$  the peak height of  $g_{1d}(r)$  is always much larger than that of  $g_{2d}(r)$  at the same time. This means that there exists a higher probability of finding type-1 colloids than finding type-2 colloids on the droplet surface.

Figure 4.6 shows results for  $g_{1d}(r)$  and  $g_{2d}(r)$  at different energy ratios  $k$  after  $4.0 \times 10^5$  MC cycles. As shown in Fig. 4.6(a),  $g_{1d}(r)$  has a peak at  $r \simeq \sigma_d(t)/2$  that is independent of the value of  $k$ . At the same time,  $g_{2d}(r)$  [Fig. 4.6(b)] exhibits two distinct peaks, the first peak at a position coinciding with the peak of  $g_{1d}(r)$ , and the second peak (marked by an asterisk), which shifts towards the first peak with increasing  $k$ .

We use Fig. 4.7 as an illustration to explain these results. Colloids trapped on the droplet surface, as shown in Fig. 4.7(a), feel the Yukawa repulsive interaction, thermal fluctuation and adsorption interaction between colloids and droplets  $\Phi_{id}$ ,  $i = 1, 2$ . For a given colloid 1–droplet interaction  $\gamma_1 = 100k_B T/\sigma^2$ , whose magnitude is much larger than the Yukawa repulsive interaction and thermal energy, the colloid-1 spheres cannot overcome the energy barrier to escape from the droplet surface [Fig. 4.7(b)]. Meanwhile, for  $k = 0.1$  ( $\gamma_2 = 10k_B T/\sigma^2$ ) the trapped colloid-2–droplet interaction may be comparable to the Yukawa repulsive interaction and thermal energy. This leads to some colloid-2 to be separated from each other and/or released from the droplet surface [Fig. 4.7(b)], forming the second peak at a distance larger than  $\sigma_d(t)/2$ . When the energy ratio  $k$  increases, the binding energy between trapped colloid-2 and droplets becomes stronger, which results in an increase of the probability of finding the colloid-2 at a shorter radial distance from the droplet. Finally, for  $k = 1$ , all of trapped colloid-1 and colloid-2 are strongly localized on the droplet surface [Fig. 4.7(c)], signalled by a single peak with a broader width (see Fig. 4.6).

**Table 4.2.:** Peak positions of the radial distribution functions  $g_{1d}(r)$ ,  $g_{2d}(r)$  and instantaneous droplet diameter at different stages of the time evolution for energy ratio  $k = 0.1$ . Reproduced with permission [129]. Copyright 2016, American Physical Society.

$i$	$t_i (\times 10^5 \text{ MC cycles})$	Peak positions ( $r/\sigma$ )		$\sigma_d(t)/\sigma$
		$g_{1d}(r)$	$g_{2d}(r)$	
1	2.0	2.26	2.27	4.5
2	2.4	1.92	1.95	3.9
3	2.8	1.60	1.62	3.2
4	3.2	1.26	1.29	2.5
5	3.6	0.90	0.97	1.8
6	4.0	0.55	<sup>a</sup> 0.60 1.00 <sup>b</sup>	1.1
7	5.0		<sup>c</sup>	0.0

<sup>a</sup> Peak 1

<sup>b</sup> Peak 2

<sup>c</sup> Undefined value

### Open clusters

The bond number  $n_b$  is used to distinguish different cluster structures (isomers) that possess the same number of constituent colloids  $n_c$ . For a given  $n_c$ , the smaller  $n_b$  is, the more open the structure is.

Figure 4.8 shows examples of the open clusters of  $n_c = 4 - 10$  found at  $k = 0.1$ . For each cluster, type-1 colloids (red spheres) are arranged themselves into symmetric structures, i.e., doublet, triplet, tetrahedron and triangular dipyramid (from left to right), while type-2 colloids (yellow spheres) can move freely around type-1 colloids.

### Intermediate clusters

As the energy ratio  $k$  increases, a larger number of isomers with different bond numbers  $n_b$  is found. For example, as shown in Fig. 4.9, for  $k = 0.5$  we find four distinct isomers of  $n_c = 4$  with  $n_b$  ranging from 3 to 6, corresponding to a transition from stringlike clusters to more compact structures.

### Closed clusters

At sufficiently high energy ratios, all obtained clusters have a closed (compact) structure. As an example, for the special case  $k = 1$ , two colloidal species become identical and we find compact isomers with the largest  $n_b$  [Fig. 4.10] such as tetrahedra ( $n_c = 4, n_b = 6$ ), octahedra ( $n_c = 6, n_b = 12$ ), snub disphenoids ( $n_c = 8, n_b = 18$ ), and gyroelongate square dipyramids ( $n_c = 10, n_b = 24$ ). These structures are similar to the one-component structures that minimize the second moment of the mass distribution [9]. The corresponding polyhedra are shown below in Fig. 4.10 for easy visualization.

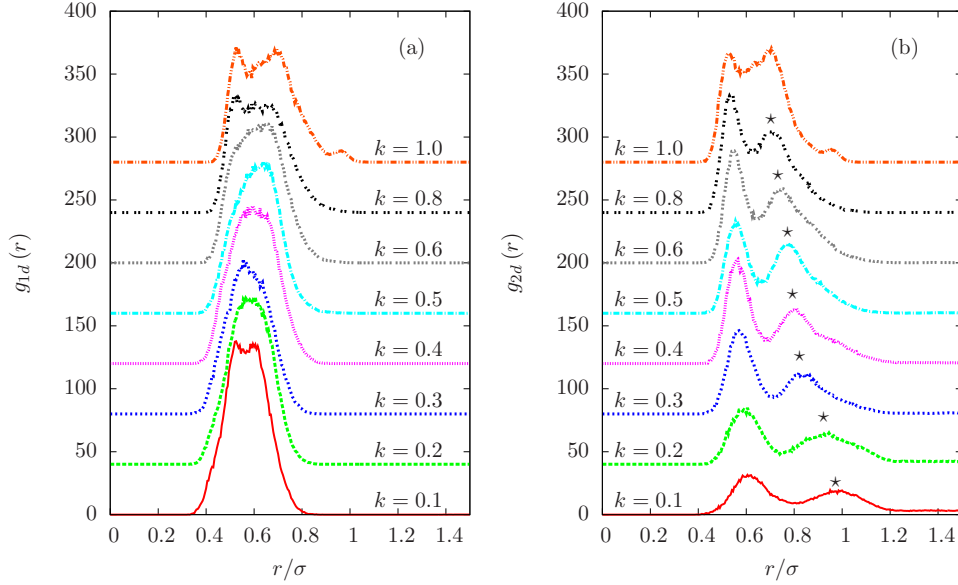


**Figure 4.6.:** Colloid-1-droplet (a) and colloid-2-droplet (b) radial distribution functions,  $g_{1d}(r)$  and  $g_{2d}(r)$ , respectively, as a function of the scaled distance  $r/\sigma$  after  $t = t_6$  ( $4.0 \times 10^5$  MC cycles). Results are shown for different energy ratios  $k$ . An asterisk is used as a guide to the eyes to trace the shift of the second peak. Curves are shifted upwards by 40 units for clarity. Reproduced with permission [129]. Copyright 2016, American Physical Society.

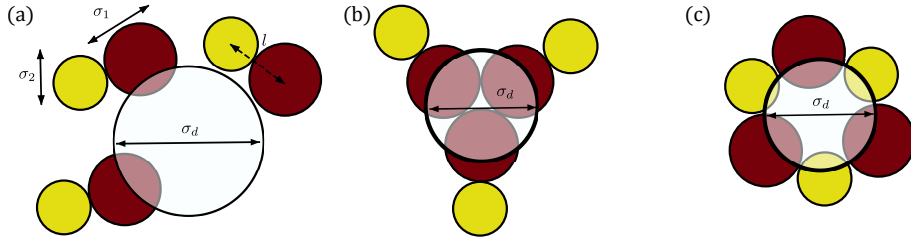


**Figure 4.7.:** Schematic diagram of the model of colloidal dumbbells and droplets (a) after the initial stage some dumbbells are trapped by the droplet (b) the droplet shrinks and pulls colloid 1 together, but keeps the colloid 2 far apart at  $k = 0.1$ , (c) the droplet shrinks and pulls both colloid 1 and colloid 2 together at  $k = 1$ .

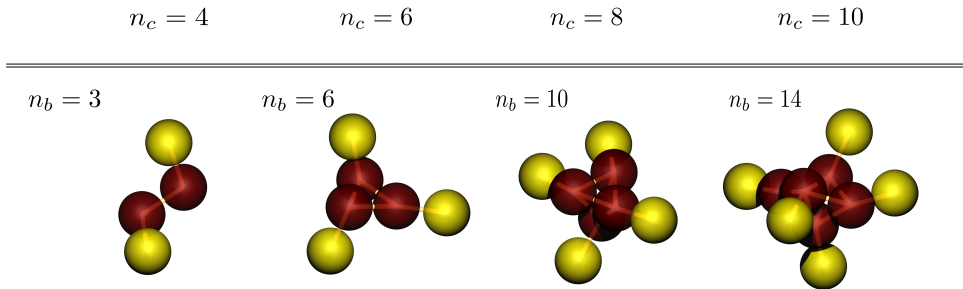


**Figure 4.8.:** Typical open clusters found in the final stage of simulations at  $k = 0.1$ . The red- and yellow-colored spheres represent colloid-1 and colloid-2 spheres in each dumbbell, respectively. For each cluster with the same number of constituent colloids the bond number  $n_b$  is used to distinguish whether a cluster is an open or closed structure. The wire frame connecting the colloid centers represents the bond skeleton. Reproduced with permission [129]. Copyright 2016, American Physical Society.

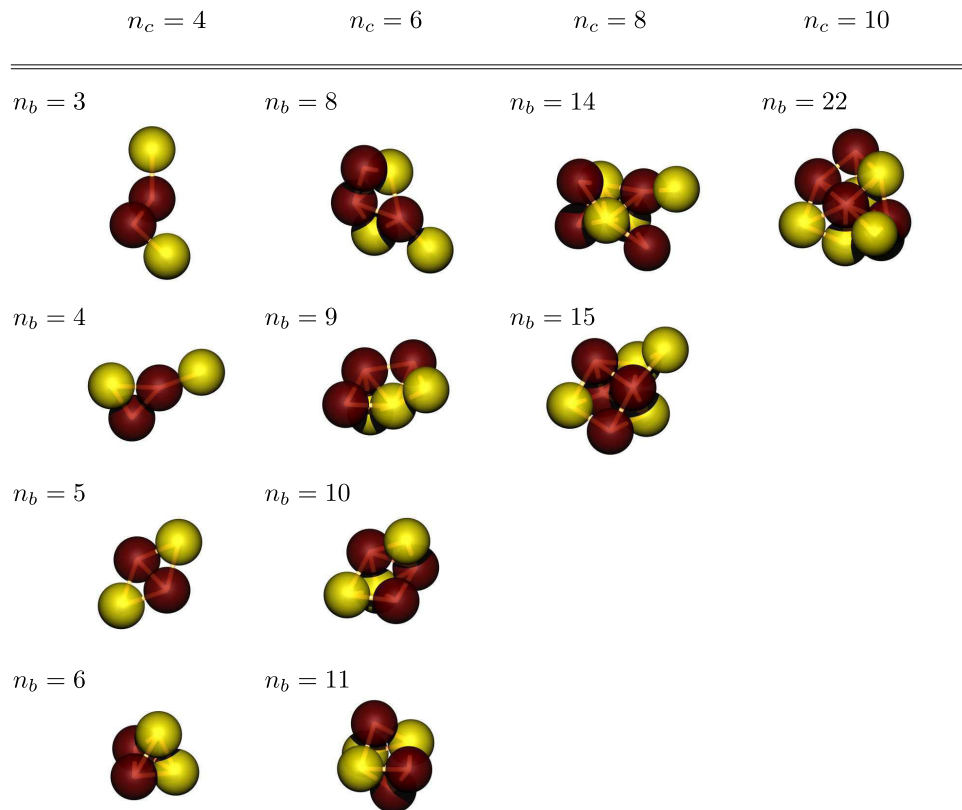


**Figure 4.9.:** Same as Fig. 4.8, but for  $k = 0.5$ . Reproduced with permission [129]. Copyright 2016, American Physical Society.

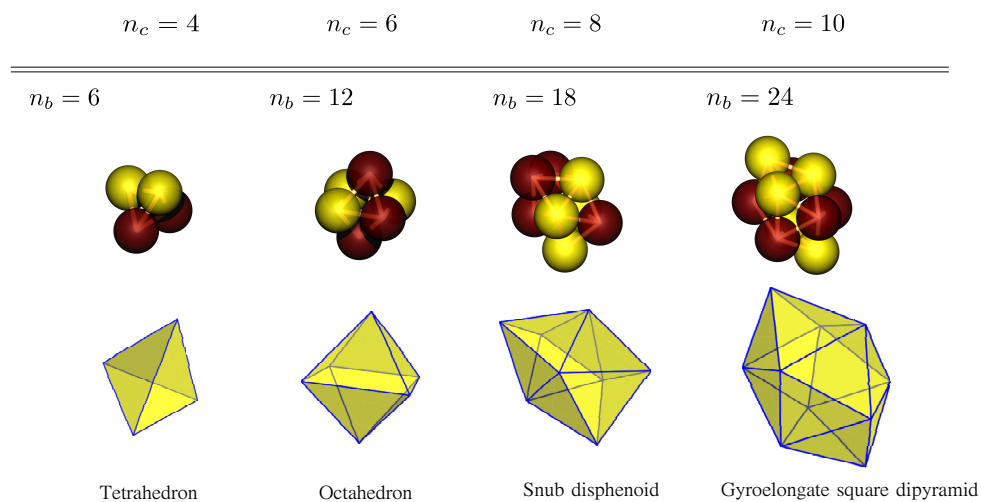


**Figure 4.10.:**  $M_2$ -minimal structures found in the final stage of the computer simulations at  $\sigma_1 = \sigma_2$  and  $\gamma_1 = \gamma_2 = 100k_B T/\sigma_2^2$ . Each column includes the number of colloids  $n_c$  with a corresponding bond-number  $n_b$ , the cluster structure and its polyhedron just below. Reproduced with permission [129]. Copyright 2016, American Physical Society.

### Stacked histograms

Figure 4.11 shows stacked histograms of the number of clusters  $N_{n_c}$  with  $n_c$  colloids. The height of each differently colored bar is proportional to the number of clusters with the bond number  $n_b$ . For a small value of  $k$  a large fraction of clusters has an open structure, whereas for  $k = 1$  almost clusters have closed structure, and for  $k = 0.3 - 0.7$  a variety of intermediate structures can be found. These observations are in good agreement with our results for colloid-droplet radial distribution functions, as discussed above.

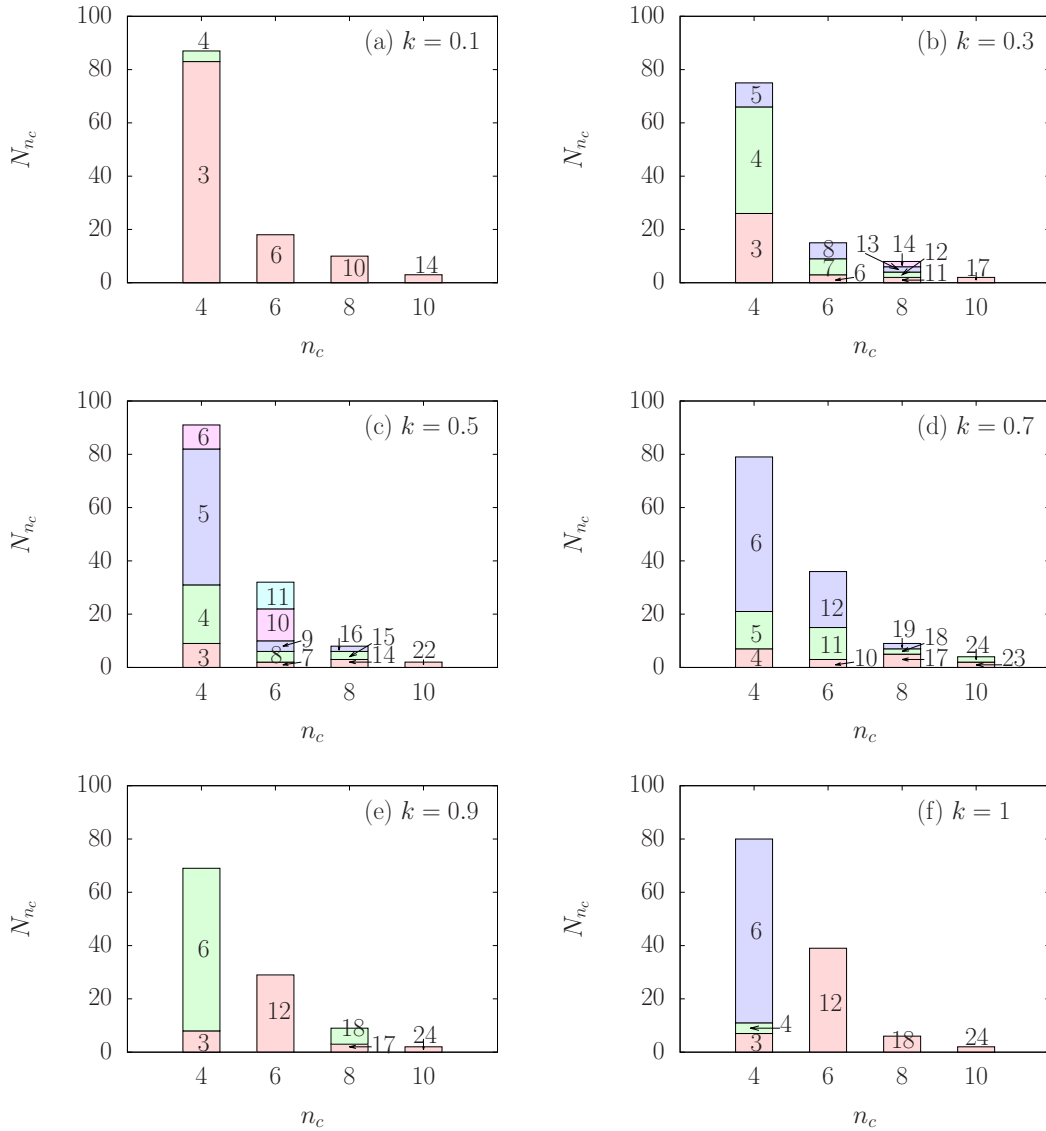


**Figure 4.11.:** Distribution of the number of clusters  $N_{n_c}$  as a function of the number of colloids  $n_c$  in the cluster in the final stage of simulation. Results are shown for different energy ratios (a)  $k = 0.1$ , (b)  $k = 0.3$ , (c)  $k = 0.5$ , (d)  $k = 0.7$ , (e)  $k = 0.9$ , and (f)  $k = 1$  at  $\sigma_1 = \sigma_2 = \sigma$  and  $\gamma = 100k_B T/\sigma_2^2$ . The colored region is labeled with the bond number  $n_b$ . Reproduced with permission [129]. Copyright 2016, American Physical Society.

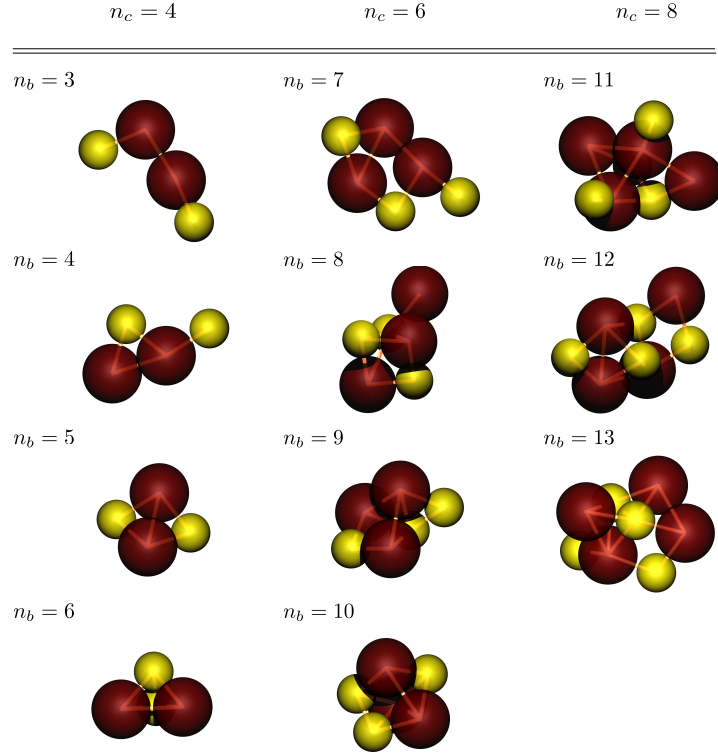


**Figure 4.12.:** Intermediate structures found in the final stage of the simulations at  $\sigma_1 = 1.5\sigma_2$  and  $\gamma = 40k_B T/\sigma_2^2$ .

### 4.3.2. Symmetric wetting properties and asymmetric sizes

We next investigate the cluster assembly of colloidal dumbbells built with spheres of different diameters but same wetting properties, which are obtained by the interfacial tension  $\gamma_1 = \gamma_2 \equiv \gamma$ . Firstly, the simulations are carried out with the setting values  $\gamma = 10, 40$  and  $100k_B T/\sigma_2^2$ , and the diameter ratio  $\sigma_1/\sigma_2 = 1.5, 2.0$ . We note that a size asymmetry between the colloids forming the dumbbells causes an asymmetry in colloid-droplet adsorption energies, as given in Eqs. (4.5) and (4.6).

Examples of the obtained cluster structures at  $\sigma_1 = 1.5\sigma_2$  are shown in Fig. 4.12 for  $\gamma = 40k_B T/\sigma_2^2$ . It can be seen that the structures found are the same as those shown in Figs. 4.8 and 4.9 for asymmetric wetting properties.

We analyze the size distribution of the clusters. Figure 4.13 shows stacked histograms of the number of clusters  $N_{n_c}$  with  $n_c$  colloids for different values of  $\gamma$ . For the case  $\sigma_1 = 1.5\sigma_2$  and  $\gamma = 10k_B T/\sigma_2^2$  [Figs. 4.13(a)], all clusters have open structures with  $n_b = 3$ . In addition, we do not find a cluster with a high  $n_c$  because the Yukawa repulsion and the thermal fluctuations dominate over the adsorption energy between colloids and droplets that keeps the colloids in a compact arrangement. On the other hand, in the case of  $\gamma = 40k_B T/\sigma_2^2$  [Figs. 4.13(b)] we observe many clusters of bond number  $n_b$  in the range 3-6, corresponding to intermediate structures. Finally, when  $\gamma = 100k_B T/\sigma_2^2$ , the adsorption energy between colloids and droplets is much larger than the total repulsive energy. Therefore, we observe mostly closed structures [Fig. 4.13(c)]. At a larger size asymmetry of  $\sigma_1 = 2.0\sigma_2$ , but at the same interfacial tension  $\gamma = 40, 100 k_B T/\sigma_2^2$

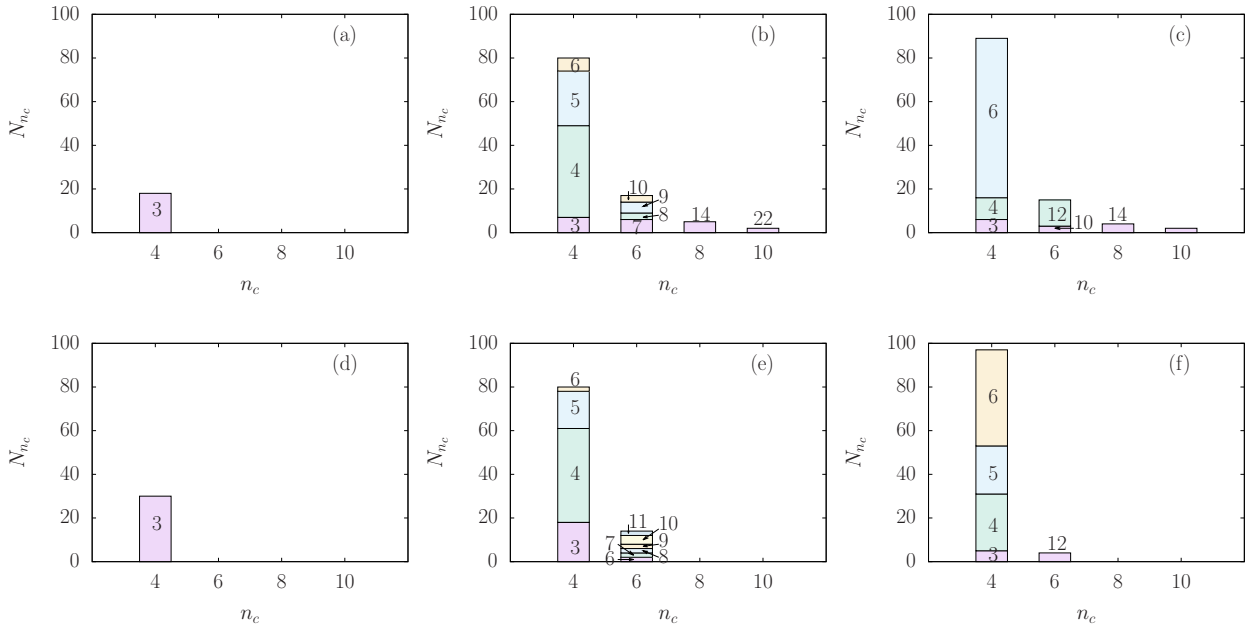


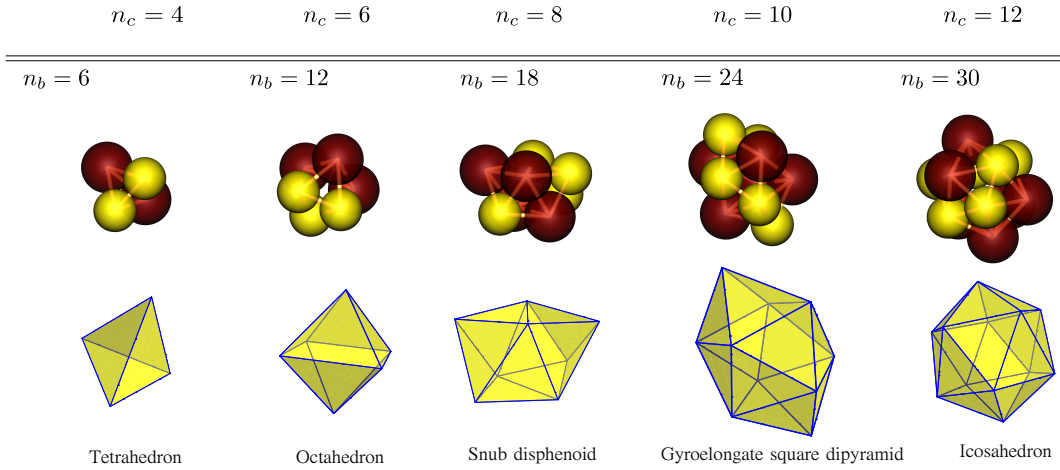
**Figure 4.13.:** Distribution of the number of clusters  $N_{n_c}$  as a function of the number of colloids  $n_c$  in the final stage of simulation. Results are for different interfacial tensions as indicated (a), (d)  $\gamma = 10k_{\text{B}}T/\sigma_2^2$ ; (b), (e)  $\gamma = 40k_{\text{B}}T/\sigma_2^2$  and (c), (f)  $\gamma = 100k_{\text{B}}T/\sigma_2^2$  at  $\sigma_1 = 1.5\sigma_2$  and  $\sigma_1 = 2.0\sigma_2$ , respectively. The numerical label in differently colored regions indicates the bond number  $n_b$ . Reproduced with permission [129]. Copyright 2016, American Physical Society.

[Fig. 4.13(b),(f) and 4.13(c),(f)] we observe a decrease of the number of large clusters, while the yield of smaller clusters increases.

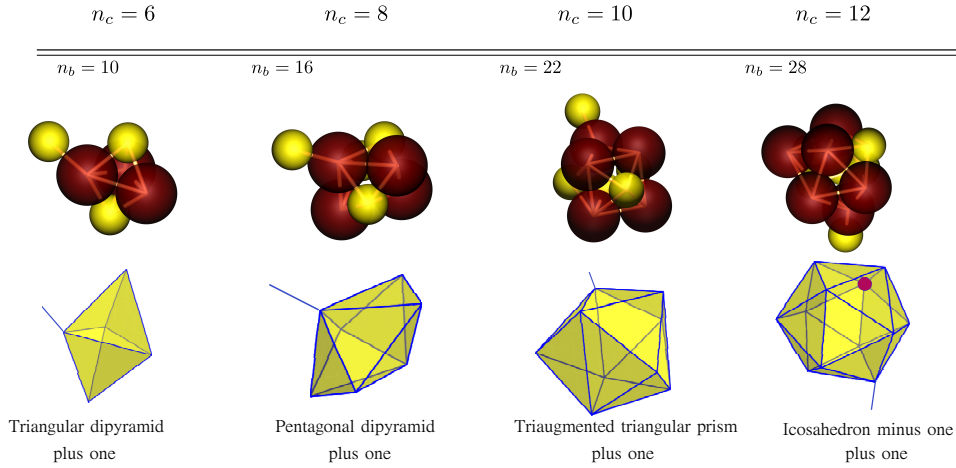
In order to further analyze the change of the cluster structures due to the change in the size ratios, we attempt to obtain larger clusters by the simulations with a higher value of the colloid and droplet packing fraction ( $\eta_c = 0.03$  and  $\eta_d = 0.15$ , respectively). The colloid 1-droplet and colloid 2-droplet adsorption energy are kept at a fixed value of  $\gamma_1 = \gamma_2 \equiv \gamma = 100k_{\text{B}}T/\sigma_2^2$  in the following simulations.

Figure 4.14 shows cluster structures obtained for the size ratio  $\sigma_1/\sigma_2 = 1.2$ . Compared to the cluster structures of symmetric size dumbbells given in Fig. 4.10, we do not find any new structure. This indicates that the uniqueness of compact cluster of colloidal dumbbells is kept until  $\sigma_1/\sigma_2 = 1.2$ . However, as the size ratio increases, e.g.  $\sigma_1/\sigma_2 = 1.5$ , there are some additional structures found, as shown in Fig. 4.15. In particular, the  $n_c$ -sphere cluster, except for the cluster with  $n_c = 12$ , can be decomposed into one  $(n_c - 1)$ -sphere clusters with the polyhedral configuration that minimizes  $M_2$  and one particle outside this polyhedron. For example, the 6-sphere cluster (left of Fig. 4.15) is composed of one 5-sphere cluster (triangular dipyramid) and one adding particle. The cluster structure with  $n_c = 12$  is identical to the icosahedron except for one missing particle inside the icosahedron (marked by a red filled circle) but plus another one outside the polyhedron. Further increasing of the size ratio, e.g.  $\sigma_1/\sigma_2 = 2.0$ , generates more different isomers that are very similar to the intermediate structures (see Fig. 4.12).

Figure 4.16 shows stacked histograms of the number of clusters  $N_{n_c}$  with  $n_c$  colloids for several different size ratios at  $\gamma_1 = \gamma_2 \equiv \gamma = 100k_{\text{B}}T/\sigma_2^2$ . For  $\sigma_1/\sigma_2 \leq 1.2$  [Figs. 4.16(a) and (b)]



**Figure 4.14.:** Cluster structures found (above) for  $\sigma_1/\sigma_2 = 1.2$  in the final stage of the simulations and corresponding polyhedra (below) for visualization the geometric arrangement.



**Figure 4.15.:** Same as Fig. 4.14, but for  $\sigma_1/\sigma_2 = 1.5$ . Only additional structures not found at  $\sigma_1/\sigma_2 = 1.2$  are shown. The thin blue line stand for the bond skeleton and the red-colored big dot represent the missing colloid.

only a unique  $n_c$ -isomers is found, except for  $n_c = 4$ . For the size ratio  $\sigma_1/\sigma_2 > 1.2$ , e.g.  $\sigma_1/\sigma_2 = 1.5$ , Fig. 4.16(c) shows two different structures: one belongs to  $M_2$ -minimal isomers with  $n_c$  colloids and the other isomers with  $n_c - 1$  colloids plus one particle (as above shown in Figs. 4.14 and 4.15, respectively). Finally, when  $\sigma_1/\sigma_2 \geq 1.7$ , e.g.  $\sigma_1/\sigma_2 = 2.0$ , we find a variety of different isomers of open, intermediate and closed structures. We interpret the occurrence of open, intermediate structures as a direct result of the spatial hindrance of type-1 colloids against the bond formation between type-2 colloids at large size ratios.

## 4.4. Conclusions

In this chapter, using kinetic Monte Carlo simulations we have investigated the cluster assembly of colloidal dumbbells via emulsion droplet evaporation. Each colloidal dumbbell is composed of two colloidal spheres separated by a distance that can be fluctuated in a small range. Colloids interact via a short-ranged attractive and longer-ranged repulsive interaction whose interaction

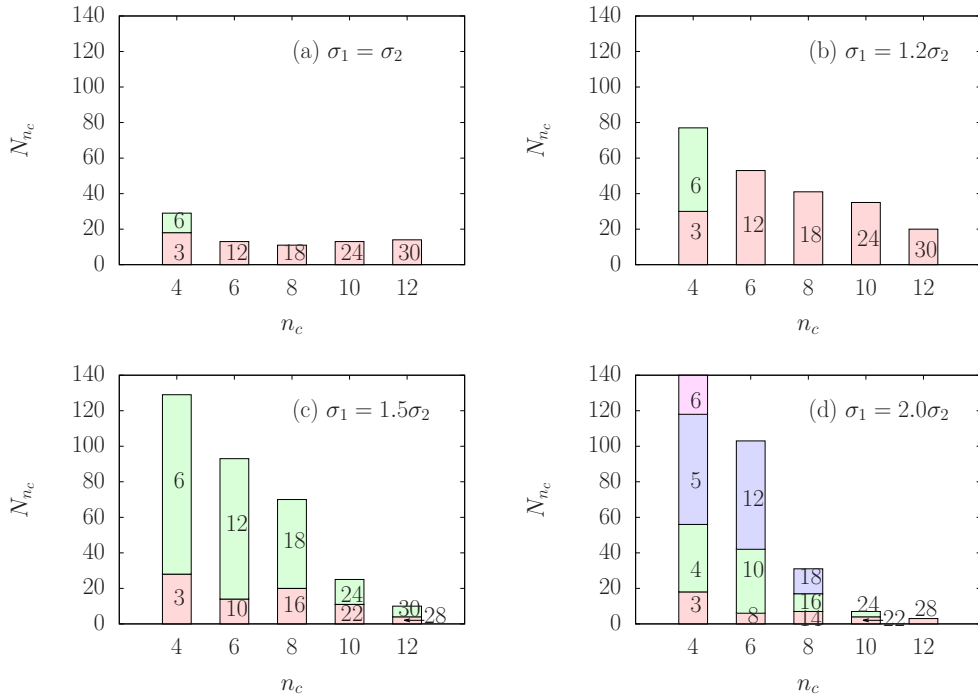


**Figure 4.16.:** Distribution of the number of clusters  $N_{n_c}$  as a function of the number of colloids  $n_c$  in the cluster in the final stage of simulation. Results are shown for different size ratios (a)  $\sigma_1/\sigma_2 = 1$ , (b)  $\sigma_1/\sigma_2 = 1.2$ , (c)  $\sigma_1/\sigma_2 = 1.5$ , and (d)  $\sigma_1/\sigma_2 = 2.0$  at  $\gamma_1 = \gamma_2 \equiv \gamma = 100k_B T/\sigma_2^2$ ,  $\eta_c = 0.03$  and  $\eta_d = 0.15$ . The numerical label in differently colored regions indicates the bond number  $n_b$ .

strength is chosen to avoid avoid spontaneous formation of clusters, and to ensure that physical bonds between colloids are permanent. The droplet-droplet interaction is a hard-core repulsion with an effective hard-sphere diameter chosen so that any two droplets cannot merge due to a shared colloid. The colloid-droplet adsorption interaction is aimed at modeling the Pickering effect having a minimum at the droplet surface. To model the evaporation of droplets in experiments, the droplet diameter shrinks at a fixed rate.

In the system of colloidal dumbbells with symmetric sizes, the colloid 1-droplet adsorption energy is kept at a fixed value, while the colloid 2-droplet adsorption varies continuously. Droplet-colloid radial distribution functions indicate that both colloid-1 and colloid-2 spheres can be captured and freely diffuse on the droplet surface. Choosing a smaller colloid 2-droplet energy leads to an increase of the probability of colloid-2 detachment from the droplet surface. In agreement with typical cluster structures in the final stage of simulation we found that clusters with the same number of constituent colloids can produce a variety of different isomers. The bond number was used to assess whether an isomer is open or closed. Histograms show that a larger fraction of open isomers can be obtained by decreasing the colloid 2-droplet adsorption energy

Similar results were obtained in the asymmetric dumbbell system. Whether open, intermediate, or closed structures are formed strongly depends on the interfacial tension of both colloid 1 and colloid 2 and their relative sizes. This results from competing Yukawa repulsion, colloid-droplet adsorption interactions, and thermal fluctuations. However, choosing a larger size of colloid 1 compared to colloid 2 could lead to a decrease in the number of large clusters. Furthermore, when the adsorption energies of the droplets with both types of colloids are much larger

than the Yukawa repulsion and thermal fluctuation, we find unique  $M_2$ -minimal isomers for size ratios less than 1.2, two distinct isomers for size ratios in the range from 1.2 to 1.7, and a variety of different isomers for size ratio larger than 1.7.

Although closed structures have been reported in many studies of the assembly of single component spheres [9, 11, 13], the open and intermediate structures found here have not yet been observed in experiments. Experimentally, the colloid-colloid interaction can be controlled by the pH, salt concentration and composition of solution [166]. Meanwhile, the colloid-droplet interaction depends on the contact angle, interfacial tension, and particle size [125]. Therefore, our result could be useful to guide experimental work for preparing increasingly complex building blocks for the assembly of nanostructured materials.

## Chapter 5.

# Crystal structure in binary hard-sphere mixtures with droplets anisotropically bonded to colloids

### 5.1. Introduction

Colloidal self-assembly into crystal structures has attracted much attention due to potential applications such as chemical sensors [35, 167], macroporous [36, 168, 169] and photonic materials [34, 170]. In searching for a structure with three-dimensional complete photonic band gap in the visible region, the diamond lattice is one of the most desirable structures [171, 172]. To date, however, such a structure has not been yet experimentally fabricated although several theoretical suggestions on the basis of colloidal self-assembly have been proposed. Tkachenko [173] first showed theoretically that the diamond lattice can be achieved by self-organization of DNA-covered colloids. The key elements of that scheme are colloidal spheres covered with short single-stranded DNA molecules to induce type-dependent interactions between colloids. These interactions are selective, reversible and tunable. The formation of the diamond structure has been observed in computer simulations of a single-component system of colloids whose surfaces are decorated with attractive patches that are distributed in tetrahedral symmetry [37]. However, crystallization to the diamond structure requires systems with a seed crystal or complicated directional dependent pair potential [37]. Since then, many efforts have been made towards the exploration of the very rich phase diagram of tetrahedral patchy particles [174–180]. Unfortunately, the diamond phase only occurs in a very narrow range in density [176, 180]. Additionally, at low pressures and finite temperatures the diamond is energetically comparable to a BCC solid. The diamond solid is only stabilized when the entropy increases, that is when the interaction range decreases. As pressure increases, the BCC solid becomes favored [176]. Doye *et al.* [38] also indicated that the crystallization from the single-component system of tetrahedral patchy colloids might not be straightforward because of the potentially frustrating effects of the variety of local structures that are possible in the liquid phase. Therefore, an alternative strategy is to use a binary mixture of colloids [39]. Here we give an overview of the structural behavior found in binary mixtures with several different types of interactions that have been widely studied in the literature.

#### 5.1.1. Binary mixtures of additive hard spheres

Monodispersed hard-sphere system have been widely used as a simple model to explain many fundamental properties of fluids, crystals and glasses [112, 181, 182]. Despite the lack of both

attraction and directionality in the pair interaction potential the hard-sphere model reveals interesting phase behavior, even for the case of a single component. For example, hard-sphere suspensions are fluid at low volume packing fractions,  $\phi < \phi_f$  ( $\phi_f = 0.494$  is freezing packing fraction), but fluid-solid coexistence until the melting packing fraction  $\phi_m = 0.545$  is reached [112, 181, 183]. The system which continues to crystallize above melting packing fraction is referred to as the solid. At  $\phi = 0.7405$ , the stable solid phase turns out to be FCC/HCP crystal phase which is the maximum value of the volume packing fraction [184, 185]. The phase transition from a disordered, fluid-like structure to an ordered, solid-like structure is sometimes referred to as the Kirkwood-Alder transition.

In binary mixtures of additive hard-sphere particles, where the distance of closest approach between particles of different species is the arithmetic mean of the diameters of both species, the phase behavior and the structure types of (binary) colloidal crystals are more complicated due to the relevance of three control parameters: the size ratio, the total packing fraction and the relative composition. In pioneering work Sanders and Murray [186, 187] observed the long-ranged ordered binary arrays in natural gem opals and studied the superlattice structure of  $LS_2$  (atomic analog  $AlB_2$ ) and  $LS_{13}$  (atomic analog  $NaZn_{13}$ ) where L (S) are large (small) particles. In the  $LS_2$  structure the large spheres form a simple hexagonal lattice and the small spheres form a honeycomb layer between the layers of the large spheres. The structure of  $LS_{13}$  consists of a simple cubic lattice with the large spheres located at the corners of the cube. The cube contains a body-centered small sphere surrounded by twelve spheres in an icosahedral cluster. From the packing fraction curves as a function of the size ratio of the particles,  $\gamma = r_S/r_L$  (where  $r_S$  and  $r_L$  are the radii of the small and the large spheres, respectively), the authors argued that the superlattice structure type will be stable if its maximum volume fraction is greater than 0.74, otherwise two separated monodispersed phases (FCC or HCP) of pure L and pure S would probably be favorable. For a radius ratio  $\gamma$  between 0.3 and 1, of these only LS (NaCl-type) and  $LS_2$  can satisfy this condition, whereas the  $AB_{13}$  structure slightly deviates from it. For  $\gamma < 0.3$ , a series of possible structures  $LS_n$  ( $n = 3, 4$ ) with high packing fractions are obtained by filling the cavities in a closed-packed array of large spheres by the smaller spheres.

The formation of superlattice structures in binary mixtures of charged latex particles with different particle sizes was first investigated in a series of experimental studies of Hachisu and Yoshimura. The authors found at least five different structures, including  $CaCu_5$ ,  $NaZn_{13}$ ,  $AlB_2$ ,  $MgCu_2$ -type structure and a structure with a stoichiometry of  $AB_4$  having no atomic analog [188–190]. The occurrence of a certain structure depends on the size ratio, the particle concentration and on the electrolyte concentration. The authors showed that the electrostatic repulsive forces between charged particles could not explain the spontaneous formation of these structures. Therefore, the mechanism of crystal formation must be due to some entropy effect [188]. The phase transition from a disordered phase to an ordered binary crystals upon increase of the particle concentration is considered as an extension of the Kirkwood-Alder transition for monodisperse hard-spheres [112].

To date, much of the binary hard-sphere system research is motivated by the observations of Sanders, Murray and of Hachisu, Yoshimura. Experimentally, the structure of the  $LS_2$  and  $LS_{13}$ -type crystal have been found with size ratios 0.35 – 0.58 and 0.43 – 0.58, respectively, in

hard-sphere like colloidal systems [191–194]. Monte Carlo simulations [195–198] and cell model calculations [199] have provided a consistent explanation for the stability of these structures. For size ratios  $\gamma < 0.42$  it was found theoretically [199, 200] and in computer simulations [200] that the stable phase is the NaCl/NiAs-type structure. The structure of NaCl and NiAs are formed by repeating the FCC unit cell and the HCP unit cell, respectively. In both structures, the small spheres occupy the octahedral sites formed by the large spheres. Cottin *et al.* [199] examined several other structures with a stoichiometry of LS (i.e. the ZnS- and NaTl-type structure), or with a stoichiometry of  $LS_2$  (the  $CaF_2$ -type structure) and found that, in the cell theory approach, these structures would not be stable (the structures will be described in Sec. 5.3.1). The thermodynamic and structural properties of binary hard-sphere mixtures has been widely investigated by means of weighted density functional theory [201–203] and fundamental measure density functional theory [204–208]. Phase diagrams revealed that a change in the diameter ratio  $\gamma$  of 15% has a dramatic effect on the phase diagram [202]. In particular, the melting curve evolves from spindle-like ( $0.94 < \gamma < 1$ ) into azeotropic ( $0.92 < \gamma < 0.94$ ) to eutectic shape ( $0.85 < \gamma < 0.92$ ) [202]. A list of all structures which have been predicted to be stable in the phase diagrams of binary hard-spheres obtained from computer simulations for various size ratios  $\gamma$  was given in [209]. Recently Hopkins *et al.* [210, 211] investigated the densest packing of binary hard-sphere mixtures and predicted a large number of crystal structures with uncommon stoichiometries, such as  $LS_6$ ,  $LS_{10}$ ,  $LS_{11}$ ,  $L_2S_4$ ,  $L_3S_7$ ,  $L_6S_6$ , which pack denser than monodisperse FCC/HCP packings. However, the thermodynamic stability of such structures has not yet been confirmed.

### 5.1.2. Binary mixtures of oppositely charged colloids

Electrostatic interactions play an important role in the self-assembly of particles into crystal structures. Experimentally, suspensions of oppositely charged particles were found to form equilibrium phases, i.e. ionic colloidal crystals, that belong to a set of binary structures, e.g. CsCl-,  $LS_6$ -,  $LS_8$ -, NaCl- and NiAs-type lattice obtained under different conditions [2]. Interestingly, some of these ( $LS_6$ -,  $LS_8$ - and NiAs-type) have not been observed before for colloidal systems, but are indeed stable according to the calculations of Madelung energies and computer simulations [2]. Based on a simulated annealing technique, Hynninen [212] *et al.* predicted binary crystal structures of oppositely charged colloids for size ratio 0.31, exhibiting novel structures but also colloidal analogs of doped fullerene  $C_{60}$  structures. Three of the predicted structures ( $A_6C_{60}^{bcc}$ ,  $LS_8^{fcc}$  and  $LS_8^{hcp}$ ) were also observed experimentally. The presence of a diversity of the ionic colloidal crystal structures that are not found in atomic systems comes from the fact that the stoichiometry of these structures is not dictated by charge neutrality.

### 5.1.3. Binary colloid-droplet mixtures

As discussed previously in Chap. 3 and 4, the Pickering effect has been widely used to stabilize emulsions, but also to produce colloidal clusters. Koos and Willenbacher found experimentally that the addition of an immiscible nonwetting fluid to a stable colloidal suspension leads to the formation of emulsion droplets that act as a bonding agent between the colloidal particles [213]. A

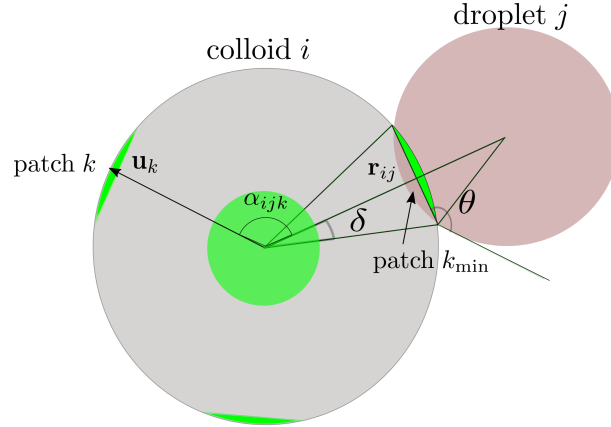


**Figure 5.1.:** Illustration of one tetrahedral patchy colloid and one droplet. Colloid  $i$  (gray sphere) has four patches (green parts) determined by a set of unit vectors  $\{\mathbf{u}_i^k\}$  ( $k = 1 - 4$ ) and patch size of half-opening angle  $\delta$ . Droplet  $j$  (pink sphere) is located at the colloid surface.  $\alpha_{ij}^k$  is the angle formed between patch  $k$  on colloid  $i$  and the vector  $\mathbf{r}_{ij}$  connecting the centers of colloid  $i$  and droplet  $j$ , and  $k_{\min}$  is the patch that minimizes the magnitude of this angle. The case shown is when  $\alpha_{ij}^{k_{\min}} = 0$ , i.e. the patch  $k_{\min}$  points along the direction of the vector  $\mathbf{r}_{ij}$ . The contact angle  $\theta$  is used to control the distance between colloid  $i$  and droplet  $j$ .

transition from a fluid to a gel driven by the formation of a network of colloidal particles bonded by emulsion droplets was found in the experiment and then supported by computer simulation results [214]. In particular, although the formation of colloidal crystal structures has not yet been observed experimentally in Pickering emulsions, Fortini [214] found in computer simulations that at a high concentration of emulsion droplets the colloid-droplet mixtures can self-assemble into a binary crystal. However, the author has not identified the structure type of this binary crystal.

In this chapter we focus on the regime of high packing fraction of particles in order to investigate the different types of crystal structures of binary colloid-droplet mixtures. We extend the model of a directional independent colloid-droplet pair interaction [214] to a highly directional interaction where each colloid is bonded to four droplets in a tetrahedral arrangement (the molecular analog is methane  $\text{CH}_4$ ). Using packing arguments [215] together with computer simulations we find several different interesting structures of binary crystals such as ZnS (the two-component analog of the diamond lattice) and  $\text{CaF}_2$ ; these structures have been predicted to be unstable in binary hard-sphere mixtures [199]. Therefore, our result could be useful to guide experimental work for synthesizing such structures with the aim of their use for practical applications, such as 3D complete photonic-bandgap materials.

This chapter is organized as follows. In Sec. 5.2 we introduce the model of pair interactions and methods used to simulate and calculate close-packing curves. In Secs. 5.3.1 and 5.3.2 we present the results for structural behavior obtained from close-packing curves and computer simulations, respectively. We end with conclusions in Sec. 5.4.

## 5.2. Model and methods

We study a mixture of  $N_c$  patchy colloidal particles of diameter  $\sigma_c$  and  $N_d$  droplets of diameter  $\sigma_d$ . Colloid-colloid and droplet-droplet pair interaction are taken to be hard-sphere pair

interaction potentials,

$$\phi_{ii}(r) = \begin{cases} \infty & r < \sigma_i, \\ 0 & \text{otherwise,} \end{cases} \quad (5.1)$$

where  $i = c$  represent the colloid-colloid interaction and  $i = d$  is the droplet-droplet interaction.

The patchy colloid-droplet pair interaction modeling the Pickering effect is defined as

$$\phi_{cd}(\mathbf{r}_{ij}, \alpha_{ijk_{\min}}) = u_{\text{PW}}(r_{ij})f(\alpha_{ijk_{\min}}), \quad (5.2)$$

where  $r_{ij}$  and  $\mathbf{r}_{ij}$  is the distance and the vector connecting the centers of colloid  $i$  and droplet  $j$ , respectively;  $\alpha_{ijk}$  is the angle between the vector  $\mathbf{r}_{ij}$  and patch  $k$ ;  $k_{\min}$  is the patch that minimizes this angle (see Fig. 5.1); and  $u_{\text{PW}}(r_{ij})$  is an isotropic parabolic well (PW) of depth  $\epsilon$ , as used in Ref. [214], given by

$$u_{\text{PW}}(r) = \begin{cases} A(r - B)^2 + C, & r < \frac{\sigma_d + \sigma_c}{2}, \\ 0, & \text{otherwise,} \end{cases} \quad (5.3)$$

with parameters  $A, B$  and  $C$  given by

$$\begin{aligned} A &= \frac{(-\epsilon + \sqrt{\epsilon^2 + r_0^2})}{2r_0^2}, \\ B &= \frac{\sigma_d + \sigma_c}{2} - r_0, \\ C &= \frac{(\epsilon - \sqrt{\epsilon^2 + r_0^2})}{2}, \end{aligned} \quad (5.4)$$

where

$$r_0 = \frac{\sigma_d}{2}(1 + \cos \theta), \quad (5.5)$$

with  $\theta$  being the contact angle between droplets and colloids, that is used to control the range of the interaction.

The parabolic potential  $u_{\text{PW}}(r)$  is modulated by the factor  $f(\mathbf{r}_{ij}, \alpha_{ijk_{\min}})$ , which is a Gaussian-like function that depends on the alignment of patches with the colloid-droplet distance vector  $\mathbf{r}_{ij}$ . This potential is quite similar to that used by Noya *et al.* [216]

$$f(\mathbf{r}_{ij}, \alpha_{ijk_{\min}}) = \exp\left(-\frac{4\alpha_{ijk_{\min}}^2}{\delta^2}\right), \quad (5.6)$$

where  $\delta$  is the half-opening angle about a unit vector  $\mathbf{u}_i^k$  which determines the widths of patches. Obviously, as  $1/\delta \rightarrow 0$  the anisotropic potential in Eq. (5.2) become isotropic. When the patch  $k_{\min}$  is pointing along the direction of the vector  $\mathbf{r}_{ij}$ ,  $f(\mathbf{r}_{ij}, \alpha_{ijk_{\min}})$  has a maximum value of 1. As shown in Fig. 5.1, the half-opening angle  $\delta$  is related to the contact angle  $\theta$  and diameter ratio by

$$\sin \delta = \frac{\sigma_d}{\sigma_c} \sin \theta. \quad (5.7)$$

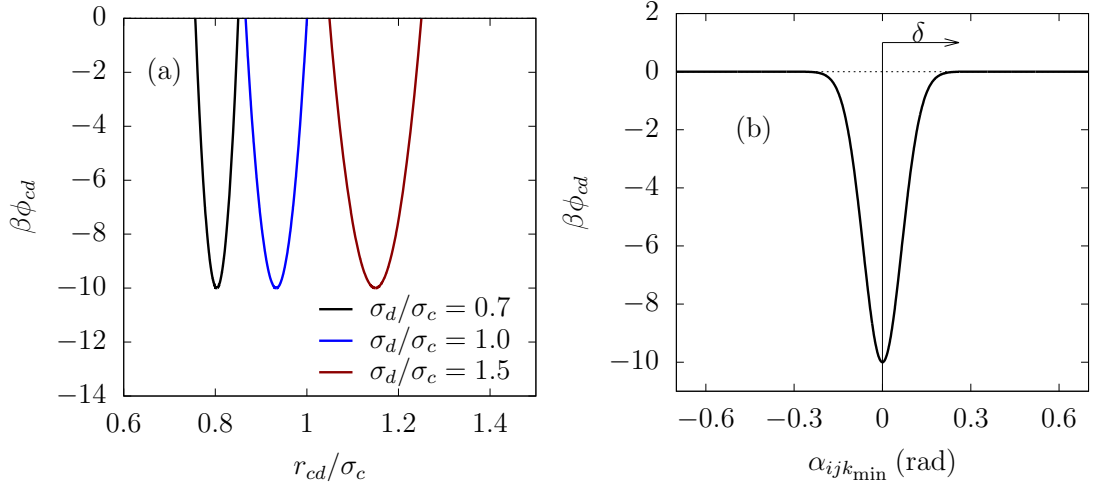


**Figure 5.2.:** (a) Colloid-droplet pair interaction as a function of the distance between colloids and droplets for different size ratios at  $\alpha_{ijk_{\min}} = 0$ .  $\beta = 1/k_{\text{B}}T$  is the inverse temperature. The potential well has a minimum value of  $10k_{\text{B}}T$  at a distance  $r = B$ . (b) Colloid-droplet potential as a function of  $\alpha_{ijk_{\min}}$  at a fixed value of the half-opening angle  $\delta = 0.26$  rad and  $r = B$ .

The surface coverage  $\chi$  is the same that defined in Sec. 3.2.1. Recall that

$$\chi = n_p \sin^2 \left( \frac{\delta}{2} \right), \quad (5.8)$$

where  $n_p$  is the number of patches.

Combination of Eqs. (5.3) and (5.6) gives the colloid-droplet interaction (see Fig. 5.2 for an illustration of the colloid-droplet pair potential)

$$\phi_{cd}(\mathbf{r}_{ij}, \alpha_{ijk_{\min}}) = \begin{cases} [A(r - B)^2 + C] \exp \left( -\frac{4\alpha_{ijk_{\min}}^2}{\delta^2} \right), & r < \frac{\sigma_d + \sigma_c}{2}, \\ 0, & \text{otherwise.} \end{cases} \quad (5.9)$$

The total interacting energy is the sum of all colloid-colloid, droplet-droplet, and colloid-droplet pair interactions

$$\frac{U_{\text{tot}}}{k_{\text{B}}T} = \sum_{i < j}^{N_c} \phi_{cc}(|\mathbf{r}_i - \mathbf{r}_j|) + \sum_{i < j}^{N_d} \phi_{dd}(|\mathbf{R}_i - \mathbf{R}_j|) + \sum_i^{N_c} \sum_j^{N_d} \phi_{cd}(\mathbf{r}_i - \mathbf{R}_j, \alpha_{ijk_{\min}}), \quad (5.10)$$

where  $k_{\text{B}}$  is the Boltzmann constant,  $T$  is the temperature,  $\mathbf{r}_i$  is the center-of-mass position of colloid  $i$ , and  $\mathbf{R}_j$  is the center-of-mass position of droplet  $j$ .

We carry out Metropolis Monte Carlo (MC) simulations in the  $NVT$  ensemble with  $10^7$  MC cycles for equilibration and  $10^5$  MC cycles for production. In each MC cycle all particles are attempted to be moved once on average. The droplets can only move translationally, whereas the colloids can both translate and rotate with adjustable trial moves to achieve an acceptance probability of around 50%. The initial random configuration of non-overlapping spherical particles is prepared in a cubic box with periodic boundary condition. The simulations are carried out for total numbers of colloids and droplets in the range 500 – 1000, i.e. at different particle packing

fractions. To improve the statistical quality each physical quantity is simulated in five independent runs and then averaged.

One of the major theoretical goals in research of colloidal crystals is to predict which crystal structure will be formed if the components of the system and their interactions are given. One relevant approach in predicting crystal structures involves free energy calculations of different structural proposals. From these results one would select the structure with the lowest free energy as that one is to occur in nature. An alternative way to predict crystal structures for hard sphere (-like) systems is to deal with packing arguments. The fundamental reason for using packing arguments is that crystal structures with a higher closed-packed density permit a larger local free volume for each sphere, resulting in a higher translational entropy and therefore a lower free energy. Parthé [215] first used packing arguments to explain binary atomic structure types. By using a principle of maximizing of the packing fraction, Murray and Sanders [187] enquired how binary systems of hard spheres might arrange into the structures found in gem opals. In particular, experimental observations of binary nanoparticle superlattices [217, 218], colloidal crystals [2, 192, 219] and theoretical predictions [220, 221] can be well explained by packing arguments.

The packing fraction is defined as the fraction of the space filled by the spheres. By convention, in systems of atomic or pure hard-spheres the packing fraction is determined with an assumption that particles are non-overlapping spheres. In our current model, however, colloidal spheres can overlap with droplets due to the Pickering effect. Hence, the space filled by spheres is the total space occupied by the hard-core spheres minus the space of overlapping regions.

According to Villars [222], there are 147 classical atomic structures adopted by roughly 5000 binary compounds. This large number of these structures results from a combination of composition, crystal system (unit-cell dimensions), space group and occupation number. In the particular case of hard-core systems, Filion *et al.* [221] and Hopkins *et al.* [210, 211] predicted additional crystal structures for which an atomic analog was not found. Fortunately, if we restrict our considerations to a given coordination number of 4 (with regular tetrahedral symmetry) then a much smaller number of crystal structures needs to be considered.

Two sets of spheres (A,B) represent droplets and colloids, respectively. Let  $q = \sigma_d/\sigma_c$  be the size ratio between droplets and colloids. Based on an approach proposed by Parthé [215] and Sanders [187], we calculate the packing fraction  $\phi(q)$  and total energy  $U_{\text{tot}}(q)$  as a function of  $q$  for the crystal structures with regular tetrahedral symmetry. The advantage of the packing fraction is that neither the radii of spheres nor the lattice parameters are needed for construction. In a set of crystal structures of interest the structure which has the highest packing fraction and lowest energy at a specific value of  $q$  will more likely occur than any other structures [187].

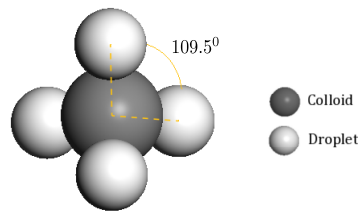


**Figure 5.3.:** Sketch of one tetrahedral patchy colloid (gray sphere) and four droplets (white spheres). The bond angles are approximately  $109.5^\circ$ .

## 5.3. Results and discussion

### 5.3.1. Close-packing calculation for structures of regular tetrahedral bond distribution

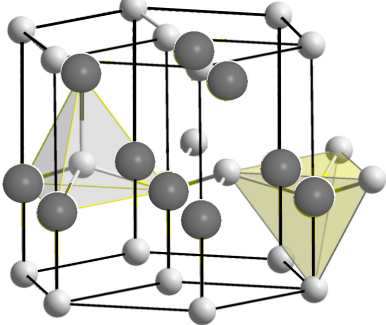
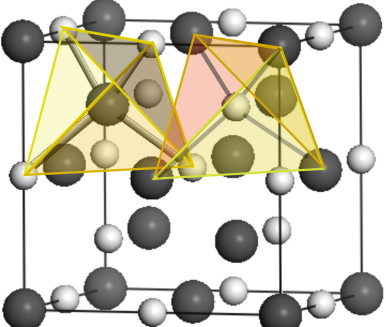
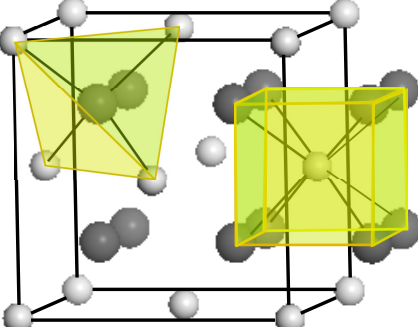
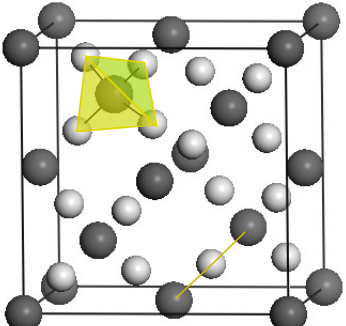
In a regular tetrahedral structure, a central colloid has four droplets that are located at the corners of a tetrahedron such that the bond angles are  $\sim 109.5^\circ$  (see Fig. 5.3). From the crystallographic data for known atomic structure types [222] we find a small number of the structure types that possess a regular tetrahedral bond distribution of the atom B with the atom A. We stress that the constraint condition for A-B-A bond angle is  $\sim 109.5^\circ$ , whereas B-A-B bond angles are arbitrary. In the binary mixture of colloids and droplets, this condition is equivalent to the droplet-colloid-droplet bond angle of  $109.5^\circ$ . These structures are given in Tab. 5.1.

Each structure (type) is characterized by the coordination number for A and B atoms. For example, in the fluorite structure each A atom is surrounded by 8 nearest neighbor atoms B, while each B atom has 4 nearest neighbor atoms A. Therefore, the environment type of the fluorite structure is denoted as 8/4.

**Table 5.1.:** Structure types found with the regular tetrahedral distribution of A-B-A bond angle.

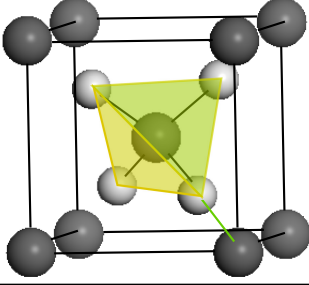
Stoichiometry	Structure Type	Structure	Environment type (A/B)
AB	Zinc Blende (ZnS)		4/4
Continued on next page			

Table 5.1 – continued from previous page

Stoichiometry	Structure Type	Structure	Environment type (A/B)
AB	Wurtzite (ZnS)		4/4
AB	Zintl phase (NaTl)		4/4
AB <sub>2</sub>	Fluorite (CaF <sub>2</sub> )		8/4
A <sub>2</sub> B	$\beta$ – Cristobalite (O <sub>2</sub> Si)		2/4

Continued on next page

Table 5.1 – continued from previous page

Stoichiometry	Structure Type	Structure	Environment type (A/B)
$A_2B$	Cuprite ( $Cu_2O$ )		2/4

In the next section, we compute close-packing curves for all above structure types. Comparison of these close-packing curves together with the total energy of the system gives a prediction for stable structures that are more likely to occur.

#### Zinc blende structure type (ZnS)

The zinc blende structure is named after the mineral zinblende (sphalerite) in which the two types of spheres form two interpenetrating FCC lattices. The zinc blende structure has two regular tetrahedral symmetries: each droplet is surrounded by four colloids, and conversely, each colloid is surrounded by four droplets, positioned at four vertices of the regular tetrahedron [see Fig. 5.4(a)].

The complete close-packing curve ( $\phi$  versus  $q$ ) for the zinc blende structure is shown in Fig. 5.6 (on log scales). We discuss each branch of the close-packing curve separately in the following

##### (a) Colloid-colloid contact (B-B contact)

For small  $q$  the positions of the droplet spheres are not uniquely defined and colloid-colloid contacts occur as shown in Fig. 5.4(b), and hence  $a = 2\sqrt{2}r_c$  with  $a$  the cubic unit cell parameter. The packing fraction for this branch of the close-packing curve is given by

$$\phi = \frac{4 \times \frac{4}{3}\pi r_c^3 + 4 \times \frac{4}{3}\pi r_d^3}{a^3} = \frac{\pi(q^3 + 1)}{3\sqrt{2}}, \quad (5.11)$$

where the factor 4 in front of the volume of the colloid and the droplet is the number of colloids and droplets in the unit cell.

As  $q$  increases, the droplet spheres touch and then at a particular value of  $q$  overlap with their nearest neighbor colloid spheres [Fig. 5.4(b)]. The overlap distance is directly related to the contact angle, the droplet radius and the colloid radius. When the overlap occurs we have

$$\begin{aligned} a &= 2\sqrt{2}r_c, \\ \frac{a\sqrt{3}}{4} &= r_d + r_c - r_0, \end{aligned} \quad (5.12)$$

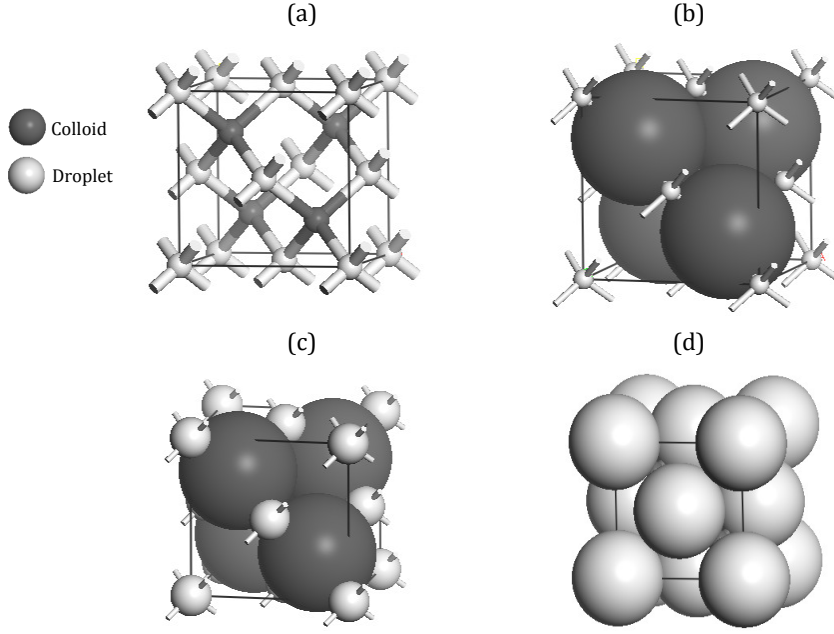


**Figure 5.4.:** Sketches of the structure and possible arrangements of zinc blende structure type (ZnS). (a) Cubic unit cell containing 4 Zn atoms (bright spheres) and 4 S atoms (dark spheres), the bond between the Zn and S atom is indicated by a line connecting them together. (b) Arrangement with Zn-Zn (colloid-colloid) contact. (c) Arrangement with Zn-S (colloid-droplet) overlapping and (d) Arrangement with S-S (droplet-droplet) contact in the unit cell.

where  $r_0$  is given by Eq. (5.5). One obtain a bound for  $q$  ( $q \leq q_1$ )

$$q_1 = \frac{1 - \sqrt{3/2}}{\cos \theta}. \quad (5.13)$$

(b) *Colloid-droplet overlap (A-B overlap)*

For  $q > q_1$  the colloidal spheres are no longer in contact with each other, but the droplets and colloidal spheres still overlap, thus

$$\phi = \frac{4\frac{4}{3}\pi r_c^3 + 4\frac{4}{3}\pi r_d^3 - 16V_0}{a^3}, \quad (5.14)$$

where  $V_0$  is the volume of the intersection region formed by one colloid and one droplet sphere, given by

$$V_0 = \frac{\pi(r_d + r_c - B)^2(B^2 + 2Br_c + 2Br_d - 3r_c^2 - 3r_d^2 + 6r_cr_d)}{12B}, \quad (5.15)$$

where  $B$  is the center-center distance between the droplet and the colloid at which the parabolic well has a minimum [see Eq. (5.4)]. Multiplication by the factor 16 in Eq. (5.14) is due to the number of bonds between the colloids and droplets in the unit cell. Equation (5.14) for the second branch of the close-packing curve becomes

$$\phi = \frac{\pi\sqrt{3} \{4 + q^3(3q - 4) + q \cos \theta [4(q^3 - 3q^2 - 1) + q^2 \cos \theta (6q + 4 \cos \theta - q \cos^2 \theta)]\}}{16(q \cos \theta - 1)^4}, \quad (5.16)$$

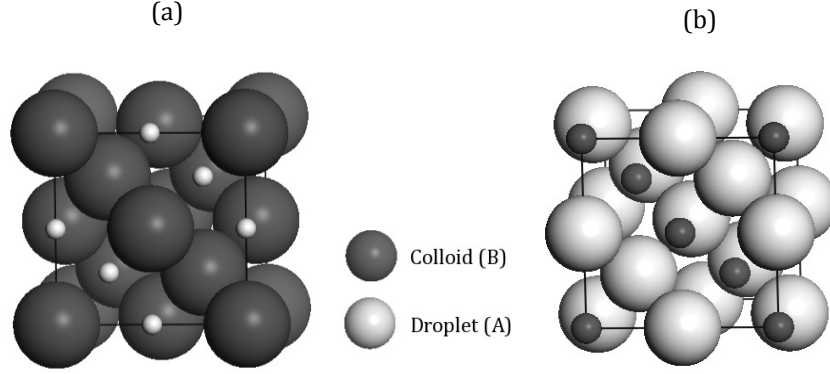


**Figure 5.5.:** Sketches of possible arrangements of NaTl. Differently from ZnS shown in Fig. (5.4), there are only two available arrangements in the unit cell of NaTl. (a) Tl-Tl (colloid-colloid) contact and (b) Na-Na (droplet-droplet) contact. The colloid-droplet overlap is forbidden.

As  $q$  is large enough, the droplet spheres can touch each other and the overlaps between the colloid and droplet spheres are still kept. We have the second bound  $q_2$  ( $q \leq q_2$ ) [see Fig. 5.4(d)]

$$\begin{aligned} a\sqrt{2} &= 4r_d, \\ \frac{a\sqrt{3}}{4} &= r_d + r_c - r_0, \end{aligned} \quad (5.17)$$

i.e.,

$$q_2 = \frac{1}{\cos \theta + \sqrt{3}/2}. \quad (5.18)$$

(c) *Droplet-droplet contact (A-A contact)*

For  $q > q_2$  the positions of the colloidal spheres become no longer unique and droplets are in contact with each other [Fig. 5.4(d)]. The packing fraction  $\phi$  is similar to that of the colloid-colloid contact, but  $a = 2\sqrt{2}r_d$ , therefore

$$\phi = \frac{\pi\sqrt{2}}{6} \left( \frac{1 + q^3}{q^3} \right). \quad (5.19)$$

### Wurtzite structure type (ZnS)

The wurtzite and zinc blende structure belong a set of homeotect structure types; i.e. every A atom has the same number of nearest A neighbors and the same number of nearest B neighbors, and, conversely, every B atom has the same number of nearest A neighbors and B neighbor atoms. Therefore, the wurtzite and zinc blende structure have the same close-packing curve [215, 223].

### Zintl structure type (NaTl)

The compound NaTl is a classical example of a Zintl phase whose thallium (B) partial structure is the diamond lattice (Tab. 5.1). However, different from all structures shown in Tab. 5.1, in Fig. 5.6, the close-packing curve for the NaTl structure has only two branches, one for B-B contact [Fig. 5.5(a)] and the other for A-A contact [Fig. 5.5(b)]. This means that A-B overlap (droplet-colloid overlap) is impossible, and hence the NaTl structure cannot be a candidate for

stable structures based on the Pickering emulsion technique.

(a) *Colloid-colloid contact (B-B contact)*

The packing fraction for this branch of the close-packing curve is given by

$$\phi = \frac{\pi\sqrt{3}}{16} (1 + q^3), \quad (5.20)$$

with  $0 \leq q \leq 1$ .

(b) *Droplet-droplet contact (A-A contact)*

$$\phi = \frac{\pi\sqrt{3}}{16} \left( \frac{1 + q^3}{q^3} \right), \quad (5.21)$$

with  $q \geq 1$ .

Similarly, we calculate the close-packing curves for the  $\text{CaF}_2$ - and  $\beta$  cristobalite-structure. The results are given below.

**Flourite structure type ( $\text{CaF}_2$ )**

(a) *Colloid-colloid contact (B-B contact)*

$$\phi = \frac{\pi}{12} (2 + q^3), \quad (5.22)$$

with  $0 \leq q \leq \frac{1 - \sqrt{3}}{\cos \theta}$ .

(b) *Droplet-colloid overlap (A-B overlap)*

$$\phi = \frac{\pi\sqrt{3} [32 - 48q^3 + 45q^4 + 8q \cos \theta (6q^3 - 9q^2 - 4) + q^3 (20q \cos 2\theta + 8 \cos 3\theta - q \cos 4\theta)]}{64(q \cos \theta - 1)^4}, \quad (5.23)$$

with  $\frac{1 - \sqrt{3}}{\cos \theta} < q \leq \frac{1}{\cos \theta + \sqrt{3/2}}$ .

(c) *Droplet-droplet contact (A-A contact)*

$$\phi = \frac{\pi\sqrt{2}}{6} \left( \frac{1 + q^3}{q^3} \right), \quad (5.24)$$

with  $q > \frac{1}{\cos \theta + \sqrt{3/2}}$ .

**$\beta$  - Cristobalite structure type ( $\text{O}_2\text{Si}$ )**

(a) *Colloid-colloid contact (B-B contact)*

If there is only B-B contact, then the A diameter must be zero. Hence,  $q = 0$  and  $\phi = 0.34$  as B spheres are located at the positions of the diamond lattice.

(b) *Droplet-colloid overlap (A-B overlap)*

$$\phi = \frac{\pi\sqrt{3} \{4 + 3q^4 - q \cos \theta [4 + 12q^2 + q^2 \cos \theta (q \cos^2 \theta - 4 \cos \theta - 6q)]\}}{64 (q \cos \theta - 1)^4}, \quad (5.25)$$

$$\text{with } 0 < q \leq \frac{1}{\cos \theta + \sqrt{3/2}}.$$

(c) *Droplet-droplet contact (A-A contact)*

$$\phi = \frac{\pi}{12\sqrt{2}} \frac{1 + 2q^3}{q^3}, \quad (5.26)$$

$$\text{with } q > \frac{1}{\cos \theta + \sqrt{3/2}}.$$

### Cuprite structure type (Cu<sub>2</sub>O)

(a) *Colloid-colloid contact (B-B contact)*

Similarly to the  $\beta$ -Cristobalite structure, only B-B contact occurs if the A diameter is zero, and hence  $\phi = 0.68$  as B spheres are located at body-center cubic positions.

(b) *Droplet-colloid overlap (A-B overlap)*

$$\phi = \frac{\pi\sqrt{3} \{4 + 3q^4 - q \cos \theta [4 + 12q^2 + q^2 \cos \theta (q \cos^2 \theta - 4 \cos \theta - 6q)]\}}{32 (q \cos \theta - 1)^4}, \quad (5.27)$$

$$\text{with } 0 < q \leq \frac{1}{\cos \theta + \sqrt{3/2}}.$$

(c) *Droplet-droplet contact (A-A contact)*

$$\phi = \frac{\pi}{6\sqrt{2}} \frac{(1 + 2q^3)}{q^3}, \quad (5.28)$$

$$\text{with } q > \frac{1}{\cos \theta + \sqrt{3/2}}.$$

We first consider the close-packing curves in our models for a special case where the contact angle  $\theta$  between the droplet and the colloid is  $180^\circ$ , i.e. binary hard-sphere mixtures. Next, we discuss the close-packing curves for the contact angle  $\theta$  of  $140^\circ$  aimed at modeling the Pickering effect.

### Binary hard-sphere mixtures

Figure 5.6 shows the packing fraction  $\phi$  as a function of  $q$  for all structures listed in Tab. 5.1 at  $\theta = 180^\circ$ . Each structure is characterized by its own individual close-packing curve, except that the ZnS-zinc blende and the ZnS-wurtzite structure have the same one since they belong to the same homeotect structure [223]. The curves of ZnS and CaF<sub>2</sub> show three distinct branches corresponding to B-B contact, A-B contact and A-A contact regions, the NaTl structure has no

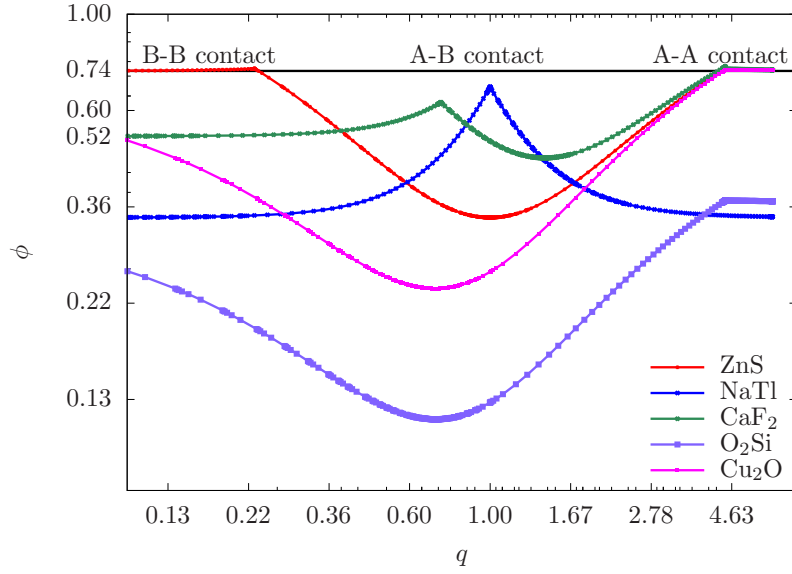


**Figure 5.6.:** Close-packing curve  $\phi$  for binary mixtures having the ZnS, NaTl, CaF<sub>2</sub>, O<sub>2</sub>Si and Cu<sub>2</sub>O structure as a function of  $q = \sigma_d/\sigma_c$  at  $\theta = 180^\circ$ . A black solid line is added to indicate the maximum packing fraction (0.74) of a monodisperse system of hard spheres corresponding to FCC or HCP. Notice the log scales.

A-B contact region, while O<sub>2</sub>Si and Cu<sub>2</sub>O has no B-B contact region. These results are identical to those calculated by Parthé [215, 223].

From the close-packing curves obtained, one can predict the phase diagram at infinite pressures because, for a given size ratio  $q$ , stable structures have the largest packing fraction. Hence we may expect ZnS ( $0 < q \leq 0.22$ ), monodisperse FCC/HCP (0.22-4.45) and ZnS/CaF<sub>2</sub>/Cu<sub>2</sub>O ( $q \geq 4.45$ ). However, these structures are predicted with the assumption of a regular tetrahedral bond angle about the colloids, which is not required for the binary hard-sphere mixtures. Theoretically, the binary hard-sphere mixtures with the highest packing fraction at infinite pressures include NaCl/NaAs ( $0 < \gamma \leq 0.44$ ), HgBr<sub>2</sub> (0.44-0.48), AuTe<sub>2</sub> (0.48-0.53), AlB<sub>2</sub> (0.53-0.62), FCC/HCP ( $\gamma \geq 0.62$ ) with  $\gamma = r_S/r_L$  being the radius ratio of the small and large hard spheres [221]. Recall that the definition of  $q$  as the size ratio between droplets and colloids ( $q = \sigma_d/\sigma_c = r_d/r_c$ ) in our model is different from that of  $\gamma$  for binary hard-sphere mixtures. The difference here is the fact that two species of particles of binary hard-sphere mixtures are only distinguished from each other by their size but not from the coordination number (the environment type).

In contrast, at finite pressures, the free energy calculations in the literature have predicted stable structure types as follows: NaCl ( $0.2 < \gamma < 0.42$ ), AlB<sub>2</sub> (0.42-0.59), NaZn<sub>13</sub> (0.48-0.62) and Laves phases (0.74-0.84) [39, 195, 196, 199, 200, 202]. However, the Laves phases have not the highest packing fraction at  $\gamma = 0.82$ . Instead, a number of structures which pack better than the Laves phases such as  $\alpha$ IrV,  $\gamma$ CuTi, AuTe<sub>2</sub> and Ag<sub>2</sub>Se was found [221]. Experimentally, the structure of AlB<sub>2</sub> and NaZn<sub>13</sub>-type crystals have been observed in natural Brazil opals [186], binary colloidal crystals [188, 189, 191, 192, 224] and mixtures of nanoparticles [225]. Crystals with a stoichiometry AB, including NaCl/NaAs and CsCl were observed experimentally in a variety of mixtures [192, 226–230]. Further binary colloidal crystals of MgCu<sub>2</sub> (Laves phases),

$\text{CaCu}_5$  and  $\text{AB}_4$  (having no atomic analogue) were reported by Yoshimura and Hachisu [189].

### Binary colloid-droplet mixtures

As was described above, numerous investigations have focused on binary mixtures consisting of hard-sphere like particles. Here the formation of complex structures is driven purely by entropic (packing) contribution to the free energy [195, 196]. Adding a soft pair interaction between the two components has a significant effect on the stability of the binary crystals that are stable for hard spheres. Furthermore, a variety of new structure types could form [226, 228].

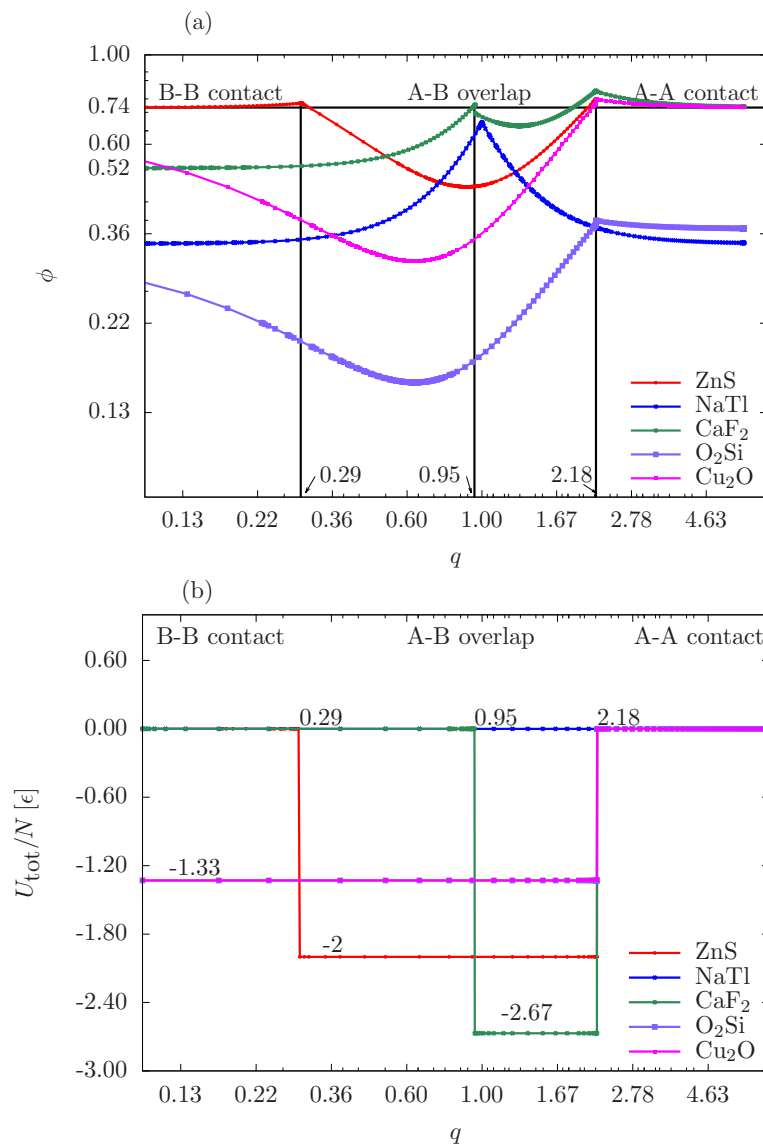


**Figure 5.7.:** (a) Close-packing curve for binary mixtures having the ZnS, NaTl,  $\text{CaF}_2$ ,  $\text{O}_2\text{Si}$  and  $\text{Cu}_2\text{O}$  structure at  $\theta = 140^\circ$ , (b) The scaled total energy per particle  $U_{\text{tot}}/N$  with  $N$  being the total number of particles is plotted against the size ratio for different structures.

Figure 5.7(a) shows close-packing curves for the structures listed in Tab. 5.1 at the contact

**Table 5.2.:** Structures predicted for different values of size ratio  $q$  at infinite pressure and  $\theta = 140^\circ$ .

Size ratio ( $q = \frac{\sigma_d}{\sigma_c}$ )	Structure Type
$q < 0.29$	Cu <sub>2</sub> O
$0.29 < q < 0.95$	ZnS
$0.95 < q < 2.18$	CaF <sub>2</sub>
$q > 2.18$	FCC/HCP of droplets+fluid of colloids

angle  $\theta = 140^\circ$ . Compared to the case of  $\theta = 180^\circ$  (Fig. 5.6), the close-packing curves for  $\theta = 140^\circ$  have the same number of branches, but the A-B branches are shifted upwards. This can be explained by the following argument. According to Eq. (5.14), as the contact angle decreases, the decrease in the denominator is faster than that in the nominator. Consequently,  $\phi$  increases with the decrease in the contact angle. An exception is the close-packing curve of NaTl that exhibits no change because of absence of the overlap region between spheres.

To determine the stability of each perfect crystal structure we calculate the total energy per particle. For example, in a unit cell of the CaF<sub>2</sub>-structure there are 32 colloid-droplet bonds corresponding to the total energy  $U_{\text{tot}} = -32\epsilon$  per unit cell, with  $\epsilon$  the colloid-droplet adsorption energy of one bond given by Eqs. (5.3) and (5.4). In addition, one unit cell of the CaF<sub>2</sub> structure consists of 8 colloids and 4 droplets, and therefore the total energy per particle is  $-32\epsilon/(8+4) = -2.67\epsilon$ . The calculated total energy per particle for several perfect structures at  $\theta = 140^\circ$  is shown in Fig. 5.7(b).

Taken together, the close-packing curves [Fig. 5.7(a)] and the total energy per particle [Fig. 5.7(b)] give the prediction of stable phases at infinite pressures, as shown in Tab. 5.2. Apparently, the structural phase transitions occur at discontinuity points of the close-packing curves [Fig. 5.7(a)], e.g. at  $q = 0.29$  (phase transition from Cu<sub>2</sub>O to ZnS),  $q = 0.95$  (ZnS-CaF<sub>2</sub>) and  $q = 2.18$  (CaF<sub>2</sub>-FCC/HCP of droplets with a dispersed fluid of colloids). Recall that these bound values of  $q$  are determined from Eqs. (5.13), (5.18) and (5.22) for a given value of  $\theta = 140^\circ$ . Therefore, for different contact angles, we can map out the phase diagram in the  $(\theta - q)$  representation, as shown in Fig. 5.8.

### 5.3.2. Simulation results

#### Phase diagram in the droplet packing fraction-energy plane

Fortini [214] simulated a mixture of hard-sphere particles and emulsion droplets, in which the colloid-droplet pair interaction is isotropic, using Brownian dynamics simulations. The author found that binary crystals can self-assemble at a high concentration of emulsion droplets. In the present study, we extend Fortini's model in order to investigate patchy colloids where the colloid-droplet interaction depends not only on the interparticle distance but also on the droplet's orientation relative to the colloid.

First, we check stable phases of the colloid-droplet mixture using Monte Carlo simulations for the case of the isotropic colloid-droplet interaction, as given in Eq. (5.2) with  $f(\mathbf{r}_{ij}, \alpha_{ijk_{\min}}) = 1$ .

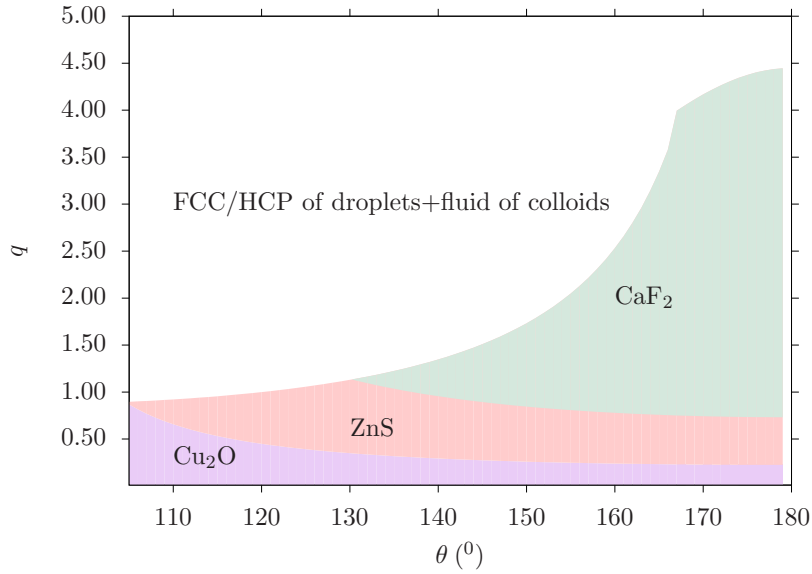


**Figure 5.8.:** Phase behavior of binary colloid-droplet mixtures at infinite pressures. The vertical and horizontal axes are the size ratio  $q$  and the contact angle  $\theta$  between droplets and colloids, respectively.

This potential is exactly the same as that was employed by Fortini [214]. Figure 5.10 shows the resulting phase diagram of the energy  $\epsilon [k_B T]$  against the droplet packing fraction  $\phi_d$  at a fixed value of the colloid packing fraction  $\phi_c = 0.1$ , the size ratio  $q = \frac{\sigma_d}{\sigma_c} = 1.5$  and the contact angle  $\theta = 150^\circ$ . We observe a low energy region of the homogeneous fluid, a higher energy region of gas-liquid coexistence, and a region of binary crystals at high packing fraction of the droplet. This result shows good agreement with the phase diagram that was reported in Ref. [214], showing a critical point and triple point. Here we determine each state point in Fig. 5.9 by collecting five independent runs and use the snapshot in the final stage of simulations in order to visualize.

Typical snapshots of three state points at  $\epsilon = 4k_B T$  at different droplet packing fractions are shown in Fig. 5.10, where large green spheres represent droplets, smaller brown spheres represent colloids. In Fig. 5.10(a) ( $\phi_d = 0.15$ ), a dense fluid consisting of both colloids and droplets and a dilute gas of colloids are observed. Subsequently increasing the droplet packing fraction to  $\phi_d = 0.3$  leads to the formation of homogeneous fluid [Fig. 5.10(b)]. Finally, when the droplet packing fraction reaches 0.5, a mixture of a binary crystal and the fluid is formed [Fig. 5.10(c)].

To determine the type of the crystal structure given in Fig. 5.10(c), we use the average local bond order parameters for each particle species (droplet and colloid) together with the colloid-droplet radial distribution function,  $g_{cd}(r)$ , and the nearest-neighbor coordination number (see detail in Sec. 2.3). Figure 5.11(a) shows a snapshot of the binary colloid-droplet mixture in the final stage of the simulation run. The particles are colored based on the average bond order parameters. An FCC/HCP coexistence region for both the droplets and colloids can be observed. In addition, a small number of BCC clusters and liquid particles are present. The colloid-droplet radial distribution function [Fig. 5.11(b)] shows well-defined peaks characteristic of a crystalline solid, indicating that the droplets and colloids are arranged into a highly ordered structure. From these observations and the first coordination number (between the colloid and droplet) of nearly 6 [inset of Fig. 5.11(b)] suggest that the simulated structure is analogous to the NaCl(NiAs)

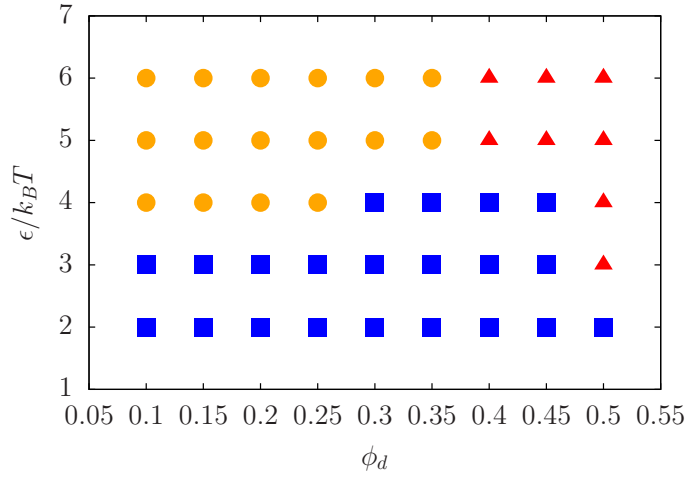


**Figure 5.9.:** Phase diagram in the droplet packing fraction-energy plane for a binary mixture with isotropic colloid-droplet potential for a set of parameters,  $\phi_c = 0.1$ ,  $q = \frac{\sigma_d}{\sigma_c} = 1.5$ ,  $\theta = 150^\circ$ . Squares indicate fluid phases, circles represent gas-liquid coexistence and triangles represent liquid-crystal coexistence. Each state point is determined by visual inspection of simulation snapshots.

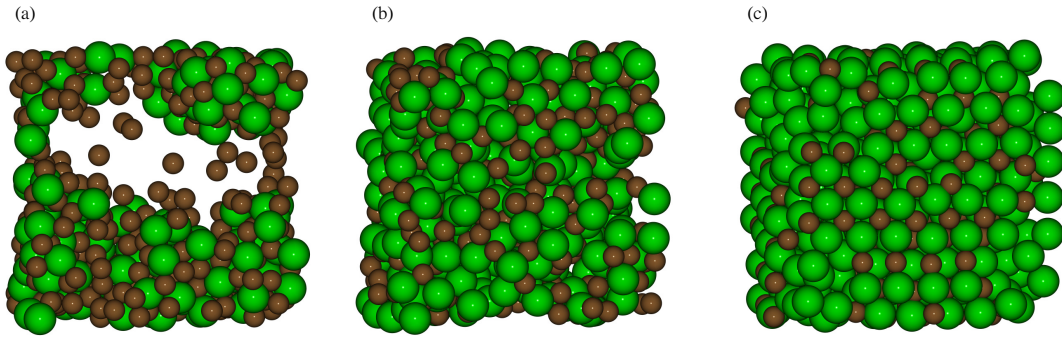


**Figure 5.10.:** Typical snapshots of binary colloid-droplet mixtures in the final stage of the simulations at  $\phi_c = 0.1$ ,  $q = \frac{\sigma_d}{\sigma_c} = 1.5$  and  $\epsilon = 4k_B T$  (a)  $\phi_d = 0.15$  gas-liquid coexistence (b)  $\phi_d = 0.3$  homogeneous fluid and (c)  $\phi_d = 0.5$  liquid-crystal coexistence. Large green spheres indicate droplets, while smaller brown spheres indicates colloids.

structure that is identical to an FCC(HCP) array of large droplets, and small colloids occupy all the octahedral holes in the FCC(HCP) lattice, and vice versa.

In comparison to the completely isotropic colloid-droplet interaction model, we consider the anisotropic colloid-droplet potential by introducing the modulating function  $f(\mathbf{r}_{ij}, \alpha_{ijk_{\min}})$ , given by Eq. (5.6) depending on the minimal angle  $\alpha_{ijk_{\min}}$  and the distance vector  $\mathbf{r}_{ij}$ . Figure 5.12(a) and 5.12(c) show snapshots in the final stage of the simulation for two different surface coverages of attractive patches:  $\chi = 1$  and  $\chi = 0.67$ , respectively. For  $\chi = 1$  we observe an FCC/HCP phase of droplets and a dispersed fluid of colloids, as shown in Fig. 5.12(a). At a lower surface coverage ( $\chi = 0.67$ ), only a homogeneous fluid phase is observed [Fig. 5.12(b)]. In the insets of Fig. 5.12(c) and (d), the nearest-neighbor coordination number is 4, in accordance with the tetrahedral bond orientation of the droplets with the colloids.

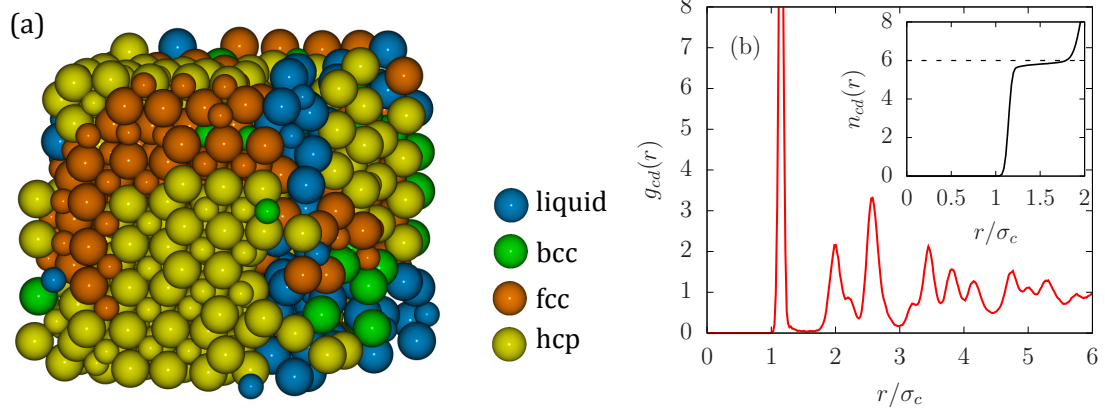


**Figure 5.11.:** (a) Snapshot in the final stage of the simulation run for a model of completely isotropic colloid-droplet interaction,  $\theta = 150$ ,  $\epsilon = 4k_{\text{B}}T$ ,  $\phi_c = 0.1$ ,  $\phi_d = 0.50$ ,  $q = \frac{\sigma_d}{\sigma_c} = 1.5$ . Large spheres represent droplets and smaller spheres represent colloids. The local structure for each particle is shown in different colors as indicated. (b) colloid-droplet radial distribution function  $g_{cd}(r)$  as a function of the scaled distance  $r/\sigma_c$ . Shown in the inset is the number of droplets  $n_{cd}(r)$  as a function of the distance  $r/\sigma_c$  from a reference colloid, which is determined by integration of  $g_{cd}(r)$ .

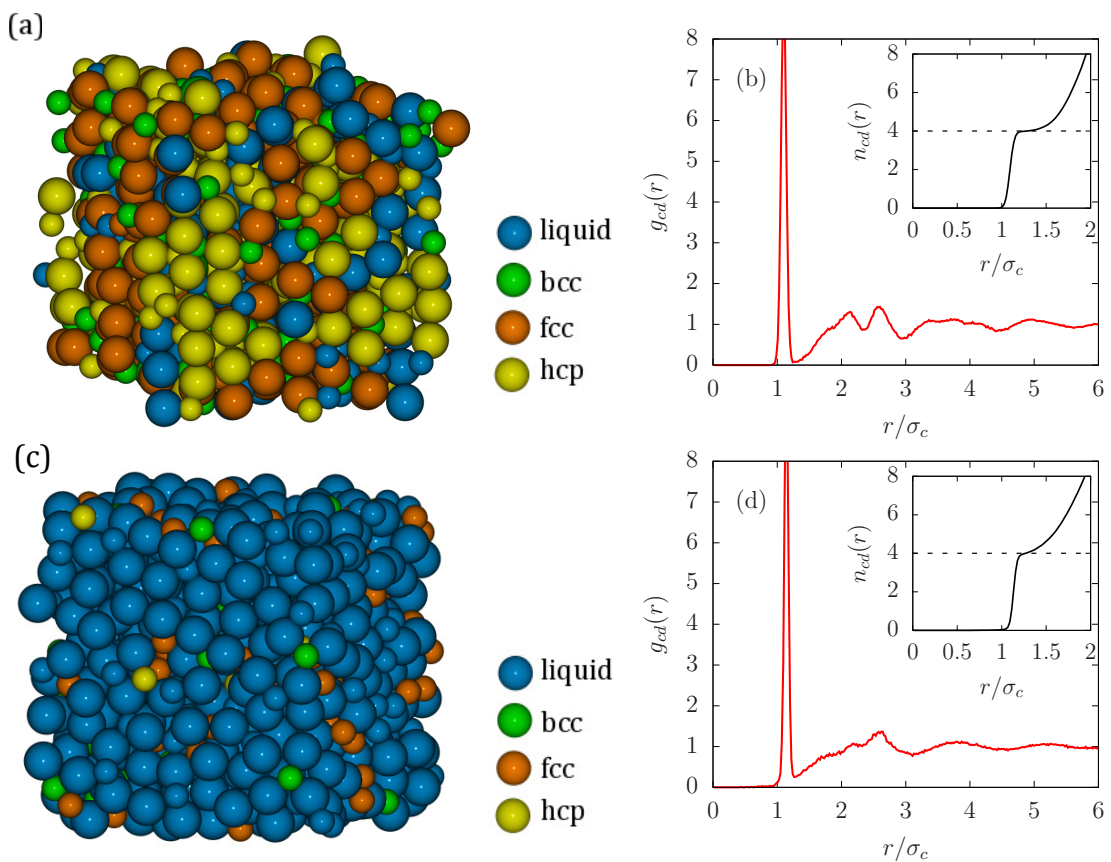


**Figure 5.12.:** Same as Fig. 5.11, but for the model of tetrahedral patchy colloid-droplet interaction. (a) and (b) for  $\chi = 1$ ; (c) and (d) for  $\chi = 0.67$ .

### Structural stability at different size ratios

To examine the stability of crystal structures as predicted by the close-packing curves and energy curves given in Fig. 5.7 and Tab. 5.2, we carry out Monte Carlo simulations for different size ratios  $q = 0.22, 0.75$  and  $0.97$  at a fixed contact angle  $\theta = 140^\circ$ . In addition, in order to ensure state points within the crystal phase region the energy  $\epsilon$  is set to  $10k_B T$  (see Fig. 5.9). The total packing fraction and composition are predetermined according to each structure of interest, e.g. for the  $\text{Cu}_2\text{O}$ -structure we fix  $\phi_c = 0.387$ ,  $\phi_d = 0.015$  and  $\frac{N_d}{N_c} = 2$ , for the  $\text{ZnS}$ -structure  $\phi_c = 0.348$ ,  $\phi_d = 0.146$  and  $\frac{N_d}{N_c} = 1$ . In the case of the  $\text{CaF}_2$ -structure, its total packing fraction ( $\phi = 0.748$ ) is so high that an initialization from a random configuration of droplets and colloids could not be performed within our present algorithm, and hence we set the composition of the  $\text{CaF}_2$ -structure to be the same as the  $\text{ZnS}$ -structure. As a result, once the  $\text{CaF}_2$ -structure is formed, it will have some missing bonds, or equivalently some vacancies. Despite the lack of some bonds, the structure  $\text{CaF}_2$  is still easily detected by analyzing the radial distribution functions and angular distribution functions. We consider the structural stability for each size ratio  $q$  as follows.

(a)  $q = 0.27$

From the snapshots in Figs. 5.13(a) and 5.13(b), we do not find the  $\text{Cu}_2\text{O}$  crystalline phase for the  $q = 0.27$  ratio. This is supported by the result of an absence of long-ranged peaks in the colloid-droplet radial distribution function [Fig. 5.13(c)]. Moreover, Figure 5.13(d) shows a low probability distribution of the angles of droplet-colloid-droplet (D-C-D) triplet at  $109.05^\circ$ , indicating a low probability of finding droplets on the colloid surface. This result can be explained as follows. Since the attractive area of colloids (depicted by dark blue parts on the colloidal sphere), which is related to the droplet size, is quite small, the probability of capturing the droplets at the colloid surface is low, and therefore the system behaves nearly as a highly asymmetric binary hard-sphere mixture, which was shown to be fluid phase at  $q = 0.2$  [231].

(b)  $q = 0.75$

Results obtained for the  $q = 0.75$  are shown in Fig. 5.14. In Fig. 5.14(a), most of the colloids and droplets assemble into a periodic three-dimensional lattice where each colloid (dark yellow sphere) is surrounded by four droplets (green spheres) located at the attractive patches (blue regions) of this colloid. Fig. 5.14(b) shows the snapshot of the system in which each particle is colored corresponding to its state. A coexistence phase of FCC and HCP for both droplets and colloids can be observed. The colloid-droplet radial distribution function shows well-defined long-ranged peaks characteristic for a specific crystal phase. Furthermore, the coordination number as a function of the scaled distance [see in the inset of Fig. 5.14(c)] and angular distribution functions [Fig. 5.14(d)] strongly confirm the regular tetrahedral bond of droplets with the colloids and vice versa. These results enable us to classify the phase of the colloid-droplet mixture at  $q = 0.75$  as the  $\text{ZnS}$  crystal structure (see zinc blende/wurtzite phase in Tab. 5.1).

(c)  $q = 0.97$

For  $q = 0.97$  the perfect  $\text{CaF}_2$  structure, as given by Tab. 5.2, requires such a very high volume packing fraction ( $\phi_c = 0.514$ ,  $\phi_d = 0.234$ ,  $\frac{N_c}{N_d} = 2$ ) that the random initialization of non-

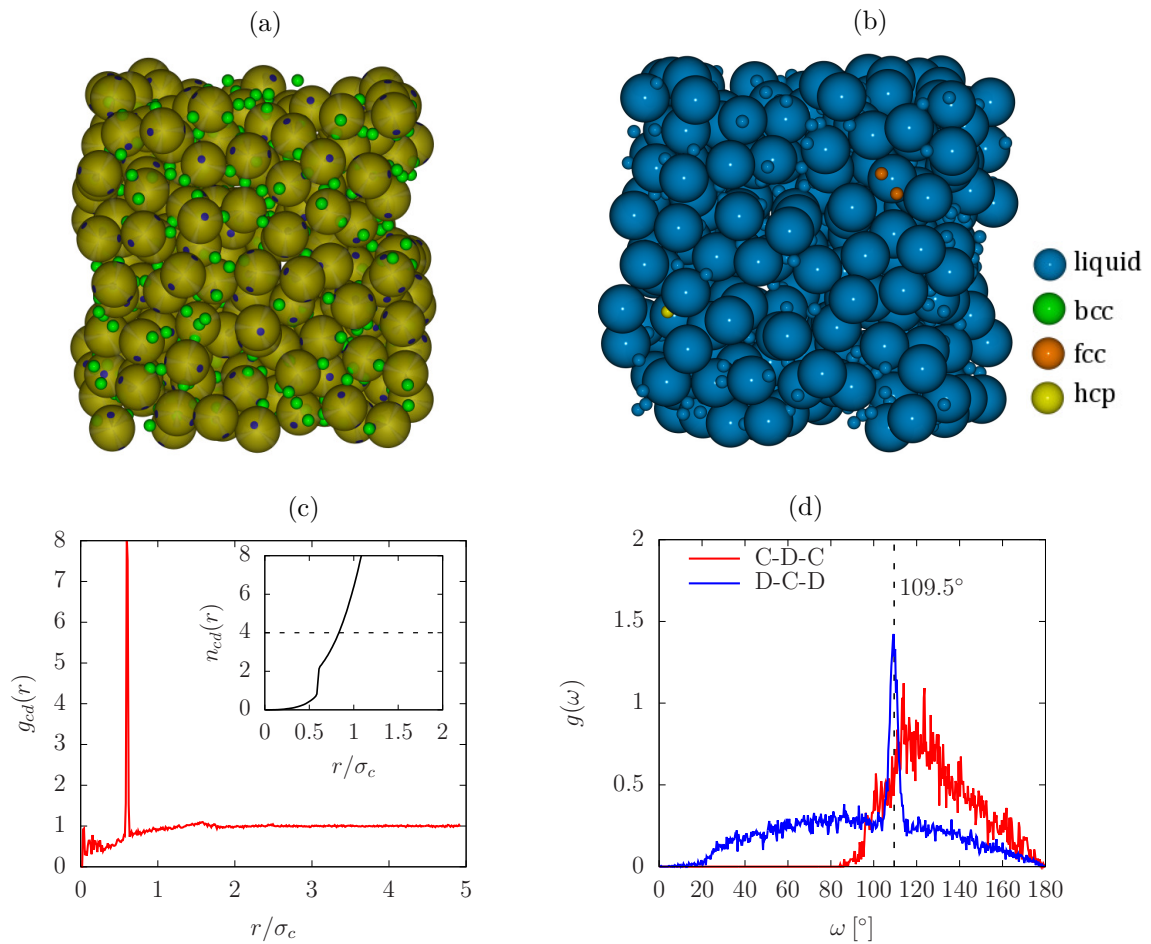


**Figure 5.13.:** (a) Snapshot of the colloid-droplet mixture in the final stage of the computer simulation at  $q = 0.27$ ,  $\phi_c = 0.387$ ,  $\phi_d = 0.015$ ,  $\frac{N_d}{N_c} = 2$ . Colloids with (blue) patches are represented by large dark yellow spheres, droplets are represented by small green spheres. (b) Same as (a) but the state of each particle is identified by the local average bond order parameters. (c) Colloid-droplet radial distribution function  $g_{cd}(r)$  (the coordination number function  $n_{cd}(r)$  is shown in the inset) as a function of the scaled distance  $r/\sigma_c$ . (d) Angular distribution function  $g(\omega)$  of colloid-droplet-colloid (red line) and droplet-colloid-droplet (blue line) angles. The label  $109.05^\circ$  marks the bond angle of a regular tetrahedron.

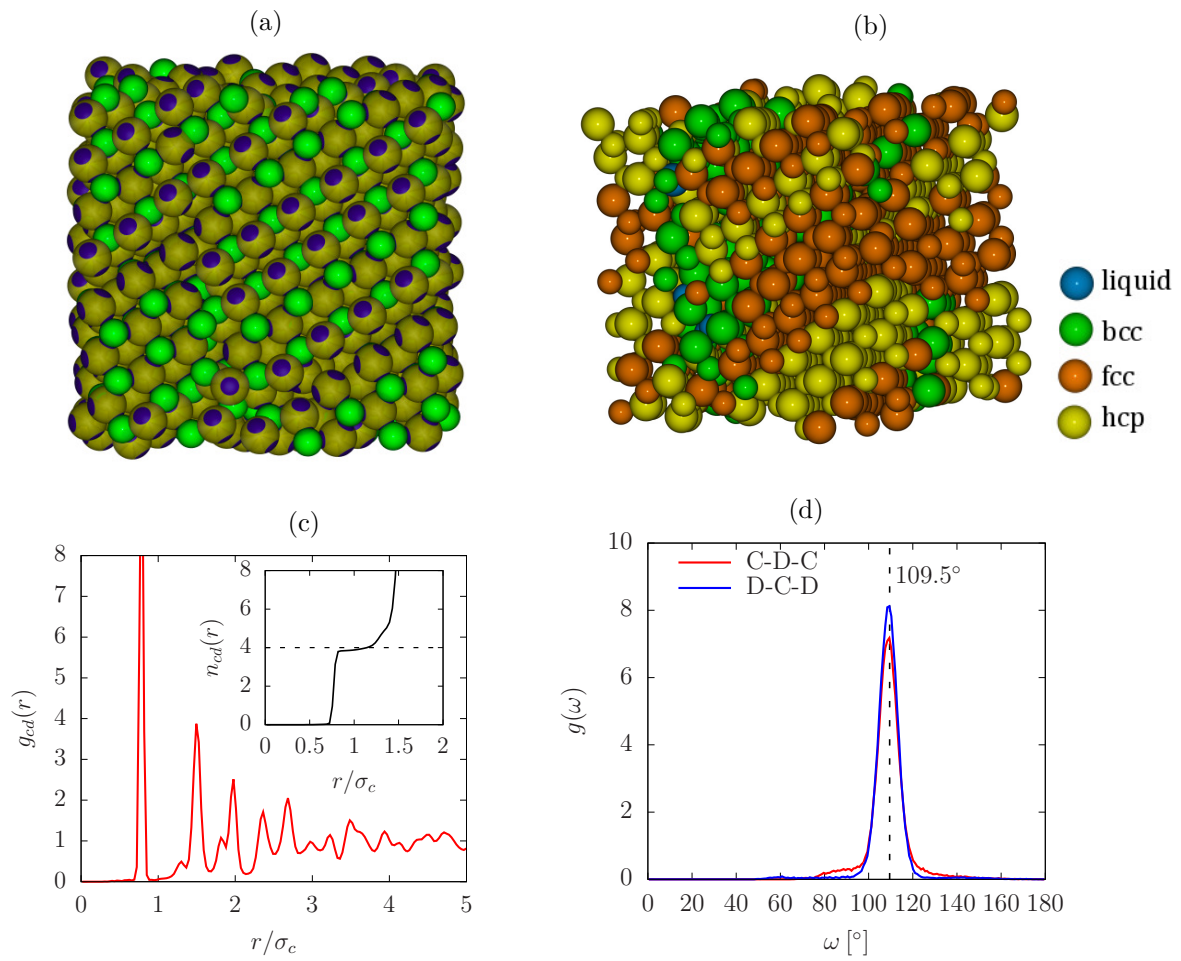


**Figure 5.14.:** Same as Fig. 5.13 but for  $q = 0.75$ ,  $\phi_c = 0.348$ ,  $\phi_d = 0.146$ , and  $\frac{N_d}{N_c} = 1$ .

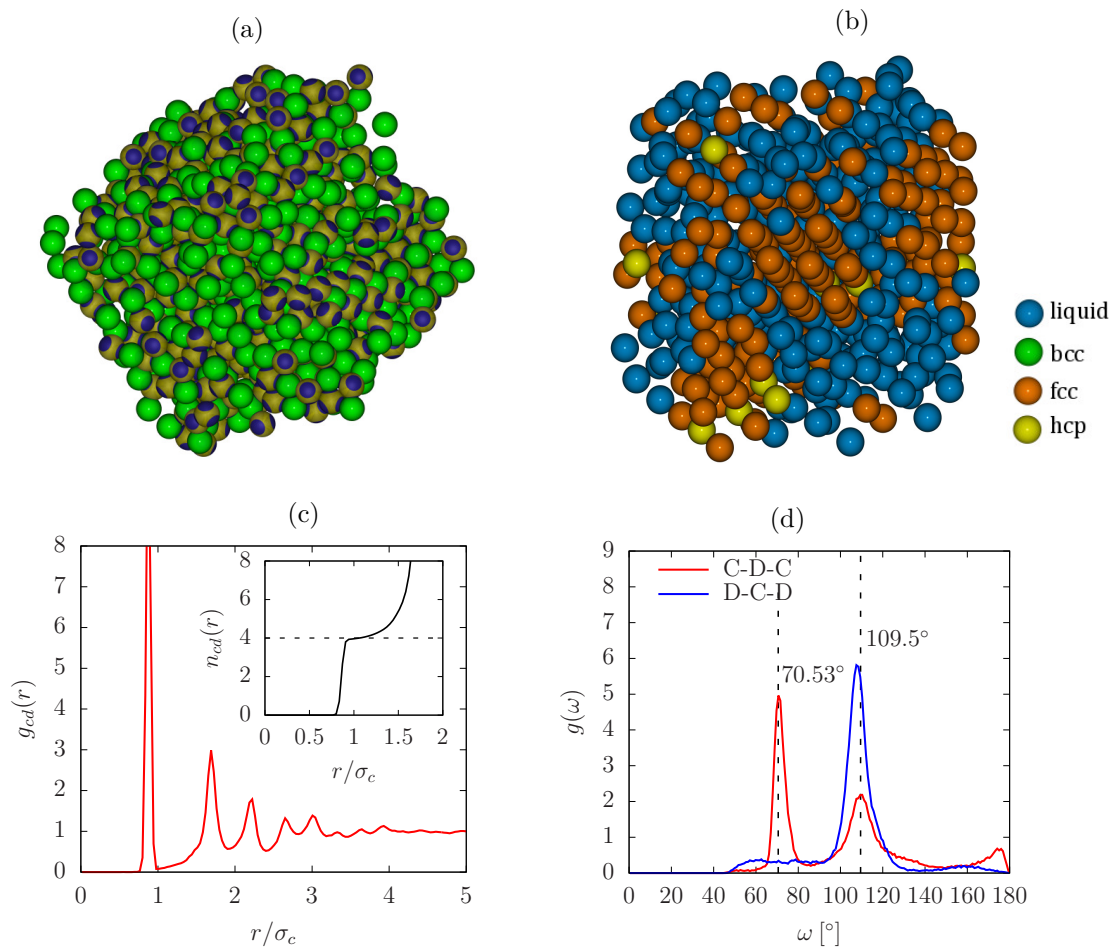


**Figure 5.15.:** Same as Fig. 5.13 but for  $q = 0.97$ ,  $\phi_c = 0.257$ ,  $\phi_d = 0.234$ , and  $\frac{N_d}{N_c} = 1$ . The labels  $70.53^\circ$ ,  $109.05^\circ$  indicate two pronounced peaks characteristic of the  $\text{CaF}_2$  structure.

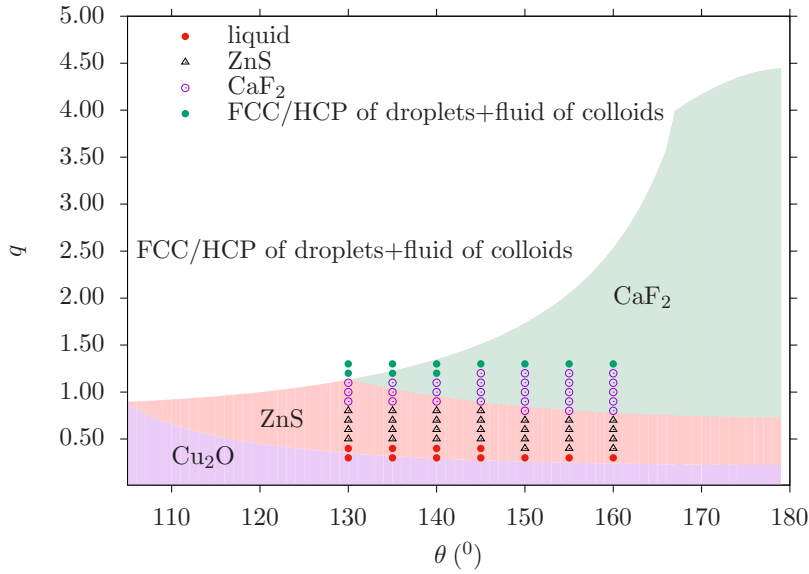


**Figure 5.16.:** Phase behavior of binary colloid-droplet mixtures determined by the theoretical prediction at infinite pressures (differently colored regions) and by computer simulation (differently shaped points). The vertical and horizontal axes are the size ratio  $q$  and contact angle  $\theta$  between droplets and colloids, respectively.

overlapping spheres does not work. Therefore, we restrict our consideration to  $\frac{N_c}{N_d} = 1$  to obtain a lower colloid packing fraction  $\phi_c = 0.257$ . Although this consideration leads to many vacancies in the  $\text{CaF}_2$  crystal structure once it is formed, we are able to detect reliably the  $\text{CaF}_2$  structure by means of radial (angular) distribution functions.

Similarly to the above descriptions for  $q = 0.27$  and  $q = 0.75$ , the visual inspection of the colloid-droplet mixture for  $q = 0.97$ , as shown in Fig. 5.15(a), indicates the presence of ordered structures. The observation of these ordered particles is more difficult due to the missing bonds in the simulated structure as compared to the perfect  $\text{CaF}_2$  structure. On the other hand, because the colloids assemble into a simple cubic lattice (see in Tab. 5.1) that is undetectable using average bond order parameters [65], we remove them from the snapshot of Fig. 5.15(b) in order to clarify the state of droplets. Combination of the visual snapshots and analysis of radial (angular) distribution functions [Figs. 5.15(c)-(d)] enables us to identify the resulting colloid-droplet mixture as the  $\text{CaF}_2$ -liquid coexistence.

(d)  $q = 1.5$

As mentioned above in Sec. 5.3.2, for  $q = 1.5$  at  $\chi = 1$  the stable phase in the final stage of the simulation is coexistence between the FCC/HCP of droplets and a fluid of colloids [see Fig. 5.12(a)]. This result also shows good agreement with that predicted by the theoretical prediction of the close-packing calculation.

#### Comparison of $(q, \theta)$ phase diagram: theory and simulation

Figure 5.16 shows a comparison of the phase diagram ( $q$  vs  $\theta$ ) obtained from the theoretical prediction (differently colored regions) and the simulation result (differently shaped symbols). We

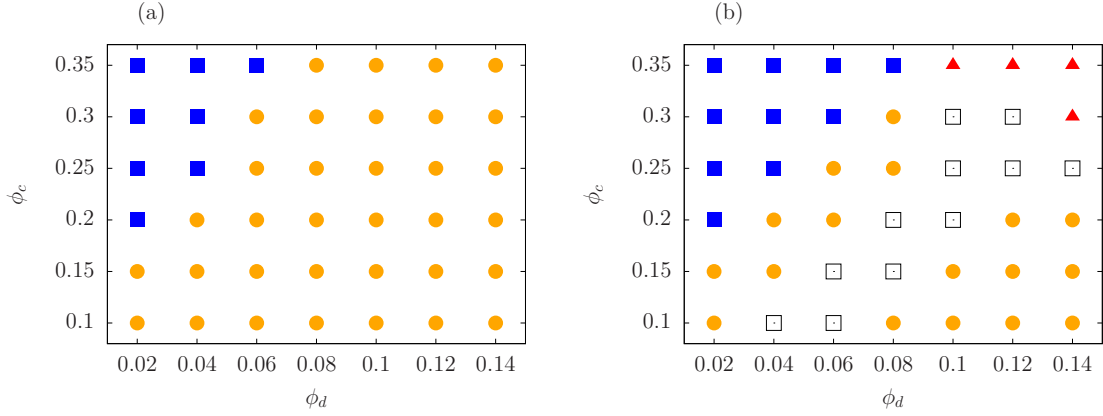


**Figure 5.17.:**  $(\phi_d, \phi_c)$  phase diagrams of the colloid-droplet binary mixture with the diameter ratio  $q = 0.75$  and parameters  $\theta = 140^\circ$ ,  $\epsilon = 10k_B T$  (a) isotropic colloid-droplet pair potential, (b) anisotropic colloid-droplet pair potential. The symbols indicate the following phases as detected by visual inspection: ■, fluid; ●, gas+liquid; □, ZnS+gas, ▲, ZnS+liquid.

find that the simulated state points of ZnS,  $\text{CaF}_2$  show good agreement with the phase regions predicted from the theoretical calculation, whereas at low ( $q < 0.3 - 0.4$ ) or high ( $q > 1.3$ ) values of  $q$  a discrepancy of the simulation result from the theoretical prediction can be observed. We interpret this discrepancy as a direct result of the finite pressure considered in the computer simulations.

#### Phase diagram in the droplet-colloid packing fraction plane for the diameter ratio $q = 0.75$

In order to investigate the equilibrium phases for the ZnS structure, which was shown to be a promising candidate for 3D complete photonic band gap materials [41], we carry out simulations for each state point in the  $(\phi_d, \phi_c)$  plane for  $q = 0.75$ . We consider two cases: isotropic and anisotropic colloid-droplet pair interaction. As shown in Figs. 5.17(a) and (b), for both cases, we find a region where the fluid is stable (marked by ■) and a region where gas-liquid separation occurs (●). In addition to that, for the anisotropic colloid-droplet pair interaction we find a region where the system separates into a gas and a ZnS crystal (□) and another region where the system separates into a fluid and a ZnS crystal (▲). Although these phases have not yet been observed experimentally in Pickering emulsions, the results could provide a useful way to obtain the ZnS structure from colloid-droplet mixtures.

### 5.3.3. Influence of symmetry of patch geometry on the crystal structure of droplet-colloid mixtures

It is well known that the stable crystal structure of a binary atomic compound depends not only on the composition, concentration, atomic size but also on the coordination number (valence) as well as the bond angles between atoms. A variety of questions arises naturally in the binary crystals of colloid-droplet mixtures, i.e. how the crystal structure of systems changes if the patch arrangement on the colloid surface changes or how the patch variability such as size, position, strength of the attraction affects the resulting crystal structure. In principle, a variety of types of patch arrangement on the colloid surface are possible based on cluster configurations (see Chap. 3)

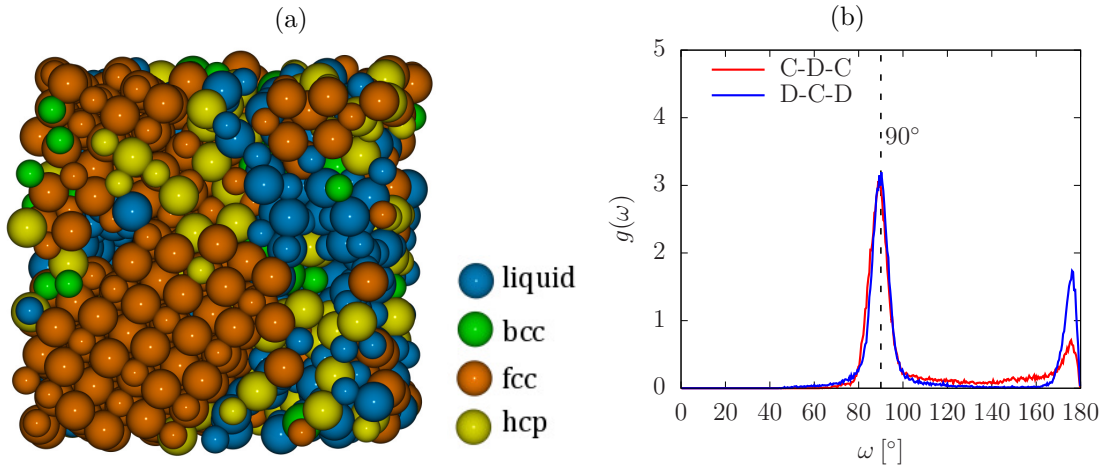


**Figure 5.18.:** Snapshot, angular distribution functions for a colloid-droplet system where patches are arranged in square plane symmetry. (a) Snapshot of the simulation with large (small) spheres represent colloids and droplets, respectively. (b) Angular distribution functions for the colloid-droplet-colloid (C-D-C) and droplet-colloid-droplet (D-C-D). The parameters are used for simulations,  $q = 0.70$ ,  $\theta = 140^\circ$ ,  $\phi_c = 0.375$ ,  $\phi_d = 0.128$ ,  $\epsilon = 10k_B T$ ,  $N_d/N_c = 1$ .

and recent experimental findings [40]. Here we present briefly the obtained results by computer simulations for some particular cases of the patch arrangement. A generator of many types of the patch arrangement on the colloid surface is given in Appendix C.

#### Patches arranged in a square plane

As the name of square planar symmetry suggests, each colloid has its four droplets positioned at the corners of a square in the same plane about a central colloid. As shown in Fig. 5.18(a), for a typical set of parameters (justified below) that we used in the simulations, the resulting equilibrium phase consists of two interpenetrating FCC/HCP lattices with the bond angle between colloids with droplets (and vice versa) equaling nearly  $90^\circ$  [Fig. 5.18(b)]. To the best of our knowledge, this crystal structure has no atomic analog.

#### Patches arranged in an octahedron

In octahedral patchy symmetry, each colloid has its six droplets arranged around a central colloid, defining the vertices of an octahedron. The resulting phase of the octahedral patchy colloid-droplet mixture, at  $q = 0.7$ , is very similar to that of the planar square patchy colloid-droplet mixture, as above described, but with the important difference that the colloid-droplet coordination number equals six instead of four. Therefore, the octahedral patchy colloid-droplet mixture belongs to the NaCl/NiAs structure.

## 5.4. Conclusions

In this chapter a binary patchy colloid-droplet mixture was studied by means of Metropolis Monte Carlo simulations, in combination with calculation of close-packing curves. The colloid-

colloid and droplet-droplet pair interactions are taken to be purely hard-core potentials, while the colloid-droplet pair interaction is an attractive well that is parabolically dependent on distance in order to model the Pickering emulsion. The cross interaction is modulated by a Gaussian-like function to characterize a directional colloid-droplet pair interaction. Although the Gaussian-like potential is used as a generic model, its corresponding quantities can be controlled by the asymmetric wetting property of the colloid surface with the droplets, i.e. attractive parts are partial wetting, whereas the repulsive parts correspond to non-wetting or drying.

For the diameter ratio  $q = 1.5$  we found that at a high concentration of emulsion droplets the system can self-assemble into a binary NaCl/NiAs crystal structure for an isotropic colloid-droplet pair potential, but into an FCC/HCP-fluid phase coexistence for a tetrahedral patchy colloid-droplet pair potential at a high value of the surface coverage. A further decrease in the surface coverage leads to the formation of homogeneous fluids.

The analysis of the close-packing curves and total energy for a set of perfect structure proposals that possess regularly tetrahedral bond angles enables one to predict stable crystal structures at infinite pressures. The simulation results show the stability of the ZnS, CaF<sub>2</sub> structure, FCC/HCP phase of large spheres with a dispersed fluid of small spheres, which is in good agreement with the theoretical predictions for a specific range of size ratios, i.e.  $q = 0.4 - 1.3$ . The discrepancy of theoretical predictions from simulations appears at low and high size ratios. More precisely, only the homogeneous fluid phase is observed at  $q = 0.27$  instead of the Cu<sub>2</sub>O phase as predicted by theory. In addition, FCC/HCP-fluid phase coexistence can be observed in the simulation at  $q = 1.5$  instead of the CaF<sub>2</sub> structure. Note also that although micro- or nano-sized colloidal crystals of ZnS and CaF<sub>2</sub> are promising in photonic applications, they have not yet been synthesized in experiments. Therefore, our simulation results can be a useful guide to prepare these structures.

Furthermore, the  $(\phi_d, \phi_c)$ - phase diagram at  $q = 0.75$  in the case of the anisotropic interaction exhibits a rich variety of phases compared to that of an isotropic interaction. We found that ZnS-gas and ZnS-fluid phase separations are possible.

Based on a unique configuration of colloidal clusters, as mentioned in Chap. 3, we examined crystal structures for colloid-droplet mixtures in which the patches on the colloid surface are arranged in a well-defined polyhedron. As an example of octahedral patch symmetry, the NaCl/NiAs crystal structure can be observed. However, there is no atomic analog to the crystal structure of binary mixtures with patches arranged in square plane symmetry. These findings suggest that binary mixtures of patchy colloids and emulsion droplets could provide a unique way to control the formation of increasingly complex crystal structures.

## Chapter 6.

### Summary and conclusions

This thesis is concerned with the structural behavior of mixtures of colloidal particles and emulsion droplets. We focus on two typical structural motifs: colloidal clusters and colloidal crystals. Interparticle potentials are chosen as isotropic and anisotropic pair-interaction potentials. The anisotropy is due to the orientations of two colloids (Janus colloids), the orientations of droplets relative to colloids (patchy colloids), or the hydrophilic property of two constituent colloids in a dumbbell (colloidal dumbbells) with droplets.

We first consider the case of a binary mixture of Janus colloids and droplets in Chap. 3. Colloids interact via a longed-ranged repulsion and a shorter-ranged attraction modulated by an anisotropic Kern and Frenkel potential. The droplet-droplet pair interaction is a hard-core potential with an effective hard-sphere diameter chosen so that any two droplets cannot merge. The colloid-droplet interaction is an attractive well at the droplet surface in order to model the Pickering effect. To mimic droplet evaporation process in experiments, the droplet diameter shrinks at a fixed rate. We used kinetic Monte Carlo simulations with small displacement steps to mimic the dynamics. The results obtained may be summarized as follows.

The analysis of the dynamics of the cluster formation via radial distribution functions, together with the monitoring the kinetics of colloids, shows a large fraction of colloidal clusters formed at the droplet surface, in contrast to a very small fraction of spontaneously formed clusters. Moreover, the total energy and the obtained number of clusters were monitored as a function of Monte Carlo time, demonstrating the stability of clusters against thermal agitation. Using the Einstein relationship for the translational diffusion coefficient of clusters and the physical time, together with the Stokes-Einstein equation for diffusion of spherical particles, we derived an MC time of tens of seconds. Although this time is significantly smaller than the time scales of experiments that typically last tens of minutes, we do not expect the simulation time to affect the final cluster configurations.

The fraction of attractive surface on the colloid (coverage) was used to control the strength of the anisotropic attraction. When the coverage varies from unity to zero, the pair potential smoothly interpolates between the isotropic square-well to the isotropic hard-sphere potential. Compared to a common set of  $M_2$ -minimal clusters (the quantity  $M_2$  is the second moment of the mass distribution) when the coverage is greater than 0.30, we find some particular isomeric structures with well-defined configurations at coverage of 0.25, namely the square dipyramid, augmented triangular prism, square antiprism, sphenocorona, and augmented sphenocorona. Choosing a smaller value of coverage could lead to additional isomers with open structures as a direct

result of the increasingly repulsive interaction in the Kern-Frenkel potential. This result suggests that the formation of  $M_2$ -nonminimal isomers is directly related to the repulsive interaction between colloids. We stress that some of those structures (square dipyramid, augmented triangular prism, square antiprism) have been observed experimentally, the reason why they are present instead of  $M_2$ -minimal structures is still unclear. Therefore, our findings could provide a possible explanation but also be useful to guide experimental work. The analysis of an order parameter for the clusters indicates the occurrence of spherical micelles within a narrow range of coverage extending from about 0.20 to 0.30, in good agreement with the behavior of the colloid-droplet radial distribution function. In particular, using an orientational order parameter of clusters, we find that the order parameter of  $M_2$ -nonminimal clusters is slightly larger than that of  $M_2$ -minimal clusters at the same number of constituent colloids and coverage. Therefore, the maximization of the order parameter might be a condition for the formation of  $M_2$ -nonminimal clusters. A more detailed study of the cluster configuration of Janus colloids that maximizes the order parameter seems to be interesting for future work.

In addition to the cluster structures, we analyze the cluster size distribution, based on histograms, and find no significant change as the surface coverage varies. We interpret this as a direct result of a high attractive well between the colloids that we chose in the computer simulation. However, larger clusters can be obtained by increasing the colloid packing fraction. Similarly to an example of tetrahedral clusters used as building blocks, we investigated the supercluster formation from building blocks such as triangular clusters and tetrahedral clusters. All clusters are composed of Janus colloids. The superclusters obtained from the assembly of tetrahedral clusters via emulsion droplet evaporation have unique configurations, e.g. octahedral dipyramid and supertetrahedron. Such superstructures are identical to those assembled by tetrahedral building blocks composed of isotropic colloids. The questions of which structures will be formed when various building blocks (the same or different species) are used, and which of physical quantities could describe their packings, are still open.

In Chapter 4, we extended the basic model of Janus colloids to colloidal dumbbells in order to study the cluster formation of a binary mixture of colloidal dumbbells and droplets. Each dumbbell consists of two spherical colloids, labeled colloidal species 1 and colloidal species 2, with different sizes or dissimilar wettabilities. We discuss the results in two parts.

First, we consider the colloidal system with symmetric sizes but asymmetric wetting properties. The colloid 1-droplet adsorption energy is kept at a fixed value, which is significantly greater than the Yukawa repulsive interaction and the thermal energy. The colloid 2-droplet adsorption energy is controlled by varying the interfacial tension. The analysis of the colloid-droplet radial distribution during the modeled evaporation indicates a random distribution of both colloidal species at the droplet surface. By choosing an appropriate strength of the colloid 2-droplet adsorption energy, a certain number of colloidal species 2 can escape from the droplet surface due to thermal fluctuations and Yukawa repulsive forces. As a result, a variety of different isomers with open, intermediate and closed structures is found, in accordance with visual inspection of simulation snapshots. In particular, open structures with a compact core and protruding arms have not been observed in clusters of monodispersed colloids.

Secondly, in colloidal systems with asymmetric sizes but symmetric wetting properties, we also

find open, intermediate, and closed structures similar to those described above. However, choosing a large colloid 1-colloid 2 size ratio decreases the number of large clusters. Furthermore, at large colloid-droplet adsorption energies compared to the Yukawa repulsion and thermal fluctuations, we find unique  $M_2$ -minimal isomers when the size ratio is smaller than 1.2. For the size ratio in the range 1.2 – 1.7, two coexisting isomers:  $M_2$ -minimal isomer with  $n_c$  colloids and  $M_2$ -minimal isomer with  $(n_c - 1)$  colloids (plus one outside) are observed. A further increase in the size ratio leads to a variety of different isomers with more complex configurations.

In Chapter 5, we focus on the crystal structures of a binary patchy colloid-droplet mixture. To characterize the dissimilarity of the surface properties (patch) of colloids with droplets, we introduced the anisotropic contribution to the colloid-droplet pair interaction. The calculation of close-packing curves, together with the total energy, for various binary atomic compounds with tetrahedral bonds predicts the stability of different crystal structures at infinite pressure, including the  $\text{Cu}_2\text{O}$ -,  $\text{ZnS}$ -,  $\text{CaF}_2$ -structures, and FCC/HCP of droplets with a dispersed fluid of colloids. The theoretical predictions have been tested against the results of standard Monte Carlo simulations and good agreement is found at droplet-colloid size ratios in an intermediate range. However, a discrepancy between theoretical predictions and simulations appears at low or high size ratios. For example, at size ratio of 0.27 we do not observe the  $\text{Cu}_2\text{O}$  structure predicted by close-packing considerations. This result may be interpreted either as a low probability of finding droplets on the attractive parts of colloids or the effect of the finite pressure in simulations.

In agreement with the result obtained by Brownian dynamics simulations in previous work, we found the region of gas-liquid and fluid-solid separations. Furthermore, systems with anisotropic pair interaction potentials display even richer behavior, such as  $\text{ZnS}$ -gas coexistence and  $\text{ZnS}$ -fluid coexistence, as compared to that of the isotropic pair interaction potential.

We examined the influence of the patch arrangement on crystal structures. As an example, in the case of the square planar geometry, we found a particular crystal structure, described as two interpenetrating FCC/HCP lattices with bond angles of  $90^\circ$ . Such a structure has no atomic analogue. Given the recent progress in the synthesis of patchy colloids with valence and specific directional bonding we suggest that patchy colloid-droplet emulsions could, in principle, be a promising way towards the preparation of novel and complex crystal structures.

# Appendices

## Appendix A.

### Cluster analysis

#### A.1. Cluster criterion

A cluster is defined as an set of  $n$  colloidal particles connected by a network of bonds, meaning that starting from one colloid it is possible to reach all other colloids in the cluster through bonds. In our simulation, it is important to be able to identify colloids belonging to clusters. The clusters are either via droplet evaporation or they are formed spontaneously.

There are many different clustering criteria for determining whether a colloid belongs to a cluster or not. One method of doing so is based on the attractive energy that binds a colloid to other colloids already in the cluster [232]. A less time-consuming method that we employ is based on the criterion of the interparticle distance<sup>1</sup>, so that if colloid  $i$  is already in the cluster, colloid  $j$  will be also included if  $r_{ij} < \sigma_c + \Delta$ , where  $\sigma_c$  is the colloid diameter and  $\Delta$  is the width of the square well interparticle potential. For colloidal clusters formed via droplet evaporation the distance between the colloids and droplet satisfies the condition  $r_{id} < (\sigma_d + \sigma_c)/2$  with  $(\sigma_d + \sigma_c)/2 > 0$  and  $\sigma_d$  being the droplet diameter, where  $i$  refers to colloid and  $d$  to droplet.

Starting with the first colloid (colloid 1) we compute its distance from all other colloids in the system which lie within a sphere of cutoff radius,  $r_c = 2.5\sigma_c$ . Each particle that satisfies the condition  $r_{1i} < \sigma_c + \Delta$  where  $i$  runs from 2 to  $N_c$ ,  $N_c$  is the total number of colloids, will be added to a set of neighbors of colloid 1. Next, we consider colloid 2 in a similar way and check against all remaining colloids. Finally, we obtain an array of size  $N_c$  containing the sets of neighbors of each colloid.

With the sets of neighbors for all colloids, we head for the composition of clusters. Starting again with colloid 1, we label all its neighbors and their respective neighbors with an identity number. Then we proceed to the next colloid that has not been labeled yet and eventually reach the stage where all colloids have been assigned an identity. Finally, each identity number corresponds to a cluster.

---

<sup>1</sup>Algorithm and C functions for cluster analysis can be found in Ref. [232]

## A.2. Cluster initialization

In order to investigate the formation of superclusters via droplet evaporation, we start by randomly distributing small colloidal clusters with a specific structure, such as dumbbell, triangular and tetrahedral cluster in the cubic box and with random orientations. Furthermore, these clusters are initially located outside all the droplets. We employed the PACKMOL package developed by Martínez *et al.* [233] to generate initial configurations. This program considers the distribution of clusters in the box as a packing problem. Therefore, the colloids belong to different clusters have to be apart a certain distance from each other and from the droplets. We describe briefly a derivation that is based largely on the work of Martínez *et al.* [233].

Consider a mixture of  $N_d$  droplets of diameter  $\sigma_d$  and  $N$  colloidal clusters each formed by two spherical colloids. For each  $i = 1, \dots, N$ , let  $n_c(i)$  to be the number of colloids of the  $i$ -th cluster. Here  $n_c = 2$  (dumbbell cluster),  $n_c = 3$  (triangular cluster),  $n_c = 4$  (tetrahedral cluster). Each cluster is represented by the Cartesian coordinates of its colloids. The arithmetic average of the Cartesian coordinates of the colloids is the barycenter. We assume that the origin is the barycenter of all the colloids. Thus, the coordinates of the  $j$ th colloid of the  $i$ th cluster are

$$\mathbf{r}^{ij} = (x^{ij}, y^{ij}, z^{ij}). \quad (\text{A.1})$$

Suppose that the  $i$ -th cluster is sequentially rotated around the axes  $x$ ,  $y$  and  $z$  by the angles  $\boldsymbol{\theta}^i = (\theta_1^i, \theta_2^i, \theta_3^i)$ . This can be done via a rotation matrix  $R(\boldsymbol{\theta}^i)$  given by

$$R(\boldsymbol{\theta}^i) = \begin{pmatrix} c_1^i c_2^i c_3^i - s_1^i s_3^i & s_1^i c_2^i c_3^i + c_1^i s_3^i & -s_2^i c_3^i \\ -c_1^i c_2^i s_3^i - s_1^i c_3^i & -s_1^i c_2^i s_3^i + c_1^i c_3^i & -s_2^i s_3^i \\ c_1^i s_2^i & s_1^i s_2^i & c_2^i \end{pmatrix}, \quad (\text{A.2})$$

where  $s_k^i = \sin \theta_k^i$  and  $c_k^i = \cos \theta_k^i$  for  $k = 1, 2, 3$ . For the translation of  $i$ -th cluster its barycenter becomes  $\mathbf{b}^i = (b_1^i, b_2^i, b_3^i)$ . Therefore, the coordinates of a colloid will be changed from  $\mathbf{r}^{ij}$  to  $\mathbf{r}'^{ij} = (x'^{ij}, y'^{ij}, z'^{ij})$ , where

$$\mathbf{r}'^{ij} = \mathbf{b}^i + R(\boldsymbol{\theta}^i)\mathbf{r}^{ij}. \quad (\text{A.3})$$

The next step is to find angles  $\boldsymbol{\theta}^i$  and displacements  $\mathbf{b}^i$ ,  $i = 1, \dots, N$ , in such a way that  $\mathbf{r}'^{ij}$  satisfies the given constraints. In addition, two colloids  $j, j'$  of two clusters  $i, i'$  have to have a minimum-distance from each other

$$\|\mathbf{r}^{ij} - \mathbf{r}^{i'j'}\| \geq d_{\text{tol}}, \quad (\text{A.4})$$

where  $d_{\text{tol}}$  is a specified tolerance given by the user (e.g.  $d_{\text{tol}} = \sigma_c + \Delta$ , see Appex. A.1 for details). The symbol  $\|\cdot\|$  represent the usual Euclidian distance.

If  $n^{ij}$  is the number of constraints which apply to the  $j$ th colloid of the  $i$ th cluster. In practice, the constraints may be applied to a subset of colloids of all the clusters of the same type, or to

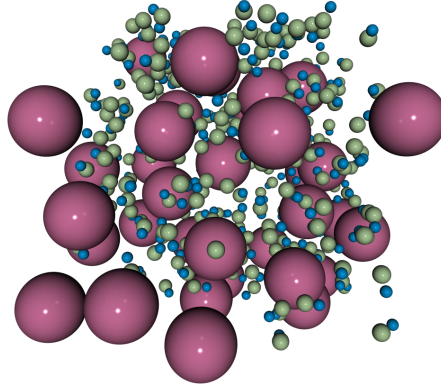


**Figure A.1.:** Initial configuration packed by PACKMOL. The droplet spheres are colored in dark pink, the two colloidal spheres in each dumbbell are colored in light yellow and blue, respectively. The number of colloidal dumbbells and droplets in the system are 250 and 35, respectively.

all the colloids of a cluster. These geometrical constraints can be written as

$$g_l^{ij}(\mathbf{r}^{ij}) \leq 0, \quad l = 1, \dots, n^{ij}. \quad (\text{A.5})$$

Given the position of the colloid, the quantity  $g_l^{ij}(\mathbf{r}^{ij})$  is positive if the constraint is fulfilled and negative otherwise. Equation (A.4) and (A.5) are called objective functions and can be taken together to form the function:

$$f(\mathbf{b}, \boldsymbol{\theta}) = \sum_{i=1}^N \sum_{j=1}^{n_c} \left( \sum_{i'=i+1}^N \sum_{j'=1}^{n_c} \max\{0, d_{\text{tol}}^2 - \|\mathbf{r}^{ij} - \mathbf{r}^{i'j'}\|^2\}^2 \right) + \sum_{i=1}^N \sum_{j=1}^{n_c} \left( \sum_{l=1}^{n^{ij}} \max\{0, g_l^{ij}(\mathbf{r}^{ij})\}^2 \right), \quad (\text{A.6})$$

where  $\mathbf{b} = (\mathbf{b}^1, \dots, \mathbf{b}^i) \in \mathbb{R}^{3N}$  and  $\boldsymbol{\theta} = (\theta^1, \dots, \theta^i) \in \mathbb{R}^{3N}$ .  $f(\mathbf{b}, \boldsymbol{\theta})$  vanish when both objectives are fulfilled otherwise it will be positive. This implies that the function  $f(\mathbf{b}, \boldsymbol{\theta})$  can be minimized. Since  $f(\mathbf{b}, \boldsymbol{\theta})$  is continuous, it can be differentiated to first order and the global function is reached when  $f(\mathbf{b}, \boldsymbol{\theta}) = 0$ .

As an example, in Fig. A.1, we show an initial configuration, built by PACKMOL, of a ternary mixture of droplets of diameter (large spheres) and colloidal dumbbells formed by two spherical colloids of different sizes (small spheres).

A model input file for PACKMOL used to generate the initial configuration given in Fig. A.1 is

```
tolerance 1.25
filetype xyz
output outdroplet.xyz

structure colloid.xyz
```

```

number 250
resnumbers 0
inside box -15. -15. -15. 15. 15. 15.
atoms 1
    radius 0.5
end atoms
atoms 2
    radius 0.75
end atoms
end structure
structure droplet.xyz
number 35
resnumbers 0
inside box -15. -15. -15. 15. 15. 15.
radius 3.0
end structure

```

The structure of a dumbbell and droplet are given in xyz format

```

2
dumbbell
H          0.0          0.0          3.6
C          0.0          0.0          5.0

and

1
droplet
D          0.0          0.0          0.0

```

### A.3. Cluster analysis and visualization

When a specific number of colloids packs together to form a closed cluster in the final stage of the computer simulation, the cluster structure belongs to a set of convex polyhedra that we are able to relatively distinguish from each other by the number of vertices and number of edges of the polyhedra, or equivalently by the number of constituent colloids  $n_c$  and the number of bonds  $n_b$  of the cluster.

Here we use ‘PolyhedronData’ data built-in Mathematica software to search the possible polyhedra with a given value of  $n_c$  and  $n_b$ , and then match our cluster structures obtained from the simulations with these polyhedra. The code used in Mathematica to search the polyhedra is

```

list = PolyhedronData[All];
For[i = 1, i < 195, i++,
  If[PolyhedronData[list[[i]], "VertexCount"] == nc, Print[list[[i]]]]]

```

```
For[i = 1, i < 195, i++,  
  If[PolyhedronData[list[[i]], "EdgeCount"] == nb, Print[list[[i]]]]]
```

where the upper limit in the **For** loop refers to the maximal number of polyhedra built in Mathematica. To visualize these polyhedra, for example, icosahedron

```
Graphics3D[{ Opacity [.5], EdgeForm[{ Thick, Blue }], FaceForm[Yellow],  
  PolyhedronData["Icosahedron", "Faces"]}, Lighting -> "Neutral",  
  Boxed -> False]
```

## Appendix B.

### Cell lists and neighbor lists

In Monte Carlo simulations, the energy calculation is the most time-consuming part. For a system of  $N$  particles and with pairwise additive interactions, we need to evaluate  $N(N-1)/2$  pair interactions, that corresponds to a computation time scaling as  $N^2$ . To reduce the computation time we incorporate cell lists and neighbor lists of cells [42]. The method is particularly useful for hard-core interactions as in our current model. In this case, only particles within a specific cut-off radius need to be considered. We first describe some important aspects of the cell list method for a single-component system and later extend straightforwardly to two-component systems.

The simulation box is divided into smaller cells of side equal to slightly larger than the cut-off radius. Suppose that each particle in a given cell interacts with the particles in the same cell or in first neighboring cells. As a result, the cell list scales as  $N$  instead of  $N^2$ .

In the initial stage of the simulation the particles are stored in cell by using two arrays: first array  $hoc(i)$ , called head-of-chain, stores the index of the first particle found inside the  $n$ th cell. To this particle the next particle in the cell is linked via the linked-list array (second array),  $ll(i)$ . In other words, the list array stores the particle index that follows particle  $i$  on the list. If the value of the  $ll(i)$  is 0 no more particles are in the cell.

In the case of the colloid-droplet mixture, we need to 3 different linked lists where the cell side length for interacting species  $\alpha$  and  $\beta$  (with  $\alpha, \beta = 1, 2$ ) has to be slightly larger than  $(\sigma_\alpha + \sigma_\beta)/2$  with  $\sigma_\alpha, \sigma_\beta$  being the diameter of species  $\alpha, \beta$ , respectively.

## Appendix C.

### Generator of patch arrangement in polyhedra

Small clusters with well-defined structures can be used as building blocks for fabrication of patchy colloids with various numbers of patches,  $n = 1 - 7$  or higher [40]. Depending on the arrangement of the attractive patches in different symmetries, the colloids may have a spherical or ellipsoidal shape (see Tab. C.1). The Cartesian coordinates of attractive patches for each polyhedron are calculated by assuming that the shortest length between two patches is unity, and the center-of-mass of the colloids located at the origin. Once these patchy coordinates of the colloid are known, we generate a random orientation of the colloid using the following steps. Firstly, generate a rotation axis which is uniformly distributed on the unit sphere, then generate a random angle  $\theta$  in a certain range  $[-\delta\theta, \delta\theta]$  and finally perform the desired rotation by  $\theta$  about the rotation axis. This procedure is repeated for all particles.

**Table C.1.:** Vertex coordinates in familiar polyhedra,  $n$  is the number of attractive patches.

$n$	Name	Vertex coordinates	Colloidal shape
4	Tetrahedron	$\{0, 0, 0.61237\}, \{-0.28868, -0.5, -0.20412\}, \{-0.28868, 0.5, -0.20412\}, \{0.57735, 0, -0.20412\}$	sphere
4	Square planar	$\{0.5, 0.5, 0\}, \{-0.5, 0.5, 0\}, \{-0.5, -0.5, 0\}, \{0.5, -0.5, 0\}$	sphere
5	Triangular dipyramid	$\{0, 0, -0.81650\}, \{0, 0, 0.81650\}, \{-0.28868, -0.5, 0\}, \{-0.28868, 0.5, 0\}, \{0.57735, 0, 0\}$	ellipsoid
5	Square dipyramid	$\{0, 0, 0.70711\}, \{0, -0.70711, 0\}, \{0, 0.70711, 0\}, \{-0.70711, 0, 0\}, \{0.70711, 0, 0\}$	ellipsoid
6	Octahedron	$\{-0.70711, 0, 0\}, \{0, 0.70711, 0\}, \{0, 0, -0.70711\}, \{0, 0, 0.70711\}, \{0, -0.70711, 0\}, \{0.70711, 0, 0\}$	sphere
7	Pentagonal dipyramid	$\{0, 0, -0.52573\}, \{0, 0, 0.52573\}, \{0.85065, 0, 0\}, \{0.26287, -0.80902, 0\}, \{0.26287, 0.80902, 0\}, \{-0.68819, -0.5, 0\}, \{-0.68819, 0.5, 0\}$	ellipsoid
7	Augmented triangular prism	$\{-0.28868, -0.5, -0.5\}, \{-0.28868, -0.5, 0.5\}, \{-0.28868, 0.5, -0.5\}, \{-0.28868, 0.5, 0.5\}, \{0.57735, 0, -0.5\}, \{0.57735, 0, 0.5\}, \{0.49789, 0.86237, 0\}$	ellipsoid
8	Snub disphenoid	$\{-0.5, 0, 0\}, \{0, -0.5, 1.5679\}, \{0, 0.5, 1.5679\}, \{0, -0.64458, 0.57837\}, \{0, 0.64458, 0.57837\}, \{0.5, 0, 0\}, \{-0.64458, 0, 0.98949\}, \{0.64458, 0, 0.98949\}$	ellipsoid
8	Square antiprism	$\{-0.5, -0.5, -0.42045\}, \{-0.5, 0.5, -0.42045\}, \{0, -0.70711, 0.42045\}, \{0, 0.70711, 0.42045\}, \{0.5, -0.5, -0.42045\}, \{0.5, 0.5, -0.42045\}, \{-0.70711, 0, 0.42045\}, \{0.70711, 0, 0.42045\}$	sphere
9	Triaugmented triangular prism	$\{-0.28868, -0.5, -0.5\}, \{-0.28868, -0.5, 0.5\}, \{-0.28868, 0.5, -0.5\}, \{-0.28868, 0.5, 0.5\}, \{0.57735, 0, -0.5\}, \{0.57735, 0, 0.5\}, \{-0.99578, 0, 0\}, \{0.49789, -0.86237, 0\}, \{0.49789, 0.86237, 0\}$	ellipsoid
10	Gyroelongated square dipyramid	$\{-0.5, -0.5, -0.42045\}, \{-0.5, 0.5, -0.42045\}, \{0, 0, -1.1276\}, \{0, 0, 1.1276\}, \{0, -0.70711, 0.42045\}, \{0, 0.70711, 0.42045\}, \{0.5, -0.5, -0.42045\}, \{0.5, 0.5, -0.42045\}, \{-0.70711, 0, 0.42045\}, \{0.70711, 0, 0.42045\}$	ellipsoid
10	Sphenocorona	$\{0, -0.5, 0\}, \{0, 0.5, 0\}, \{-0.85273, 0.5, 0.52236\}, \{-0.5, 0, 1.3133\}, \{-0.85273, -0.5, 0.52236\}, \{0.85273, 0.5, 0.52236\}, \{0.5, 0, 1.3133\}, \{0.85273, -0.5, 0.52236\}, \{0, 0.78943, 0.95720\}, \{0, -0.78943, 0.95720\}$	ellipsoid
11	Augmented sphenocorona	$\{-0.809758, -0.747109, 0.403072\}, \{-0.741888, 0.0483709, -0.199088\}, \{-0.505598, 0.132451, 0.768952\}, \{-0.222068, 0.840101, 0.121772\}, \{-0.205598, 0.590101, -0.846328\}, \{-0.0921482, -0.706059, -0.292168\}, \{0.144142, -0.621989, 0.675872\}, \{0.444142, -0.164339, -0.939408\}, \{0.466242, 0.323661, 0.631202\}, \{0.642146, 0.592011, -0.315928\}, \{0.803776, -0.351049, -0.0251775\}$	ellipsoid
12	Icosahedron	$\{0, 0, -0.95106\}, \{0, 0, 0.95106\}, \{-0.85065, 0, -0.42533\}, \{0.85065, 0, 0.42533\}, \{0.68819, -0.5, -0.42533\}, \{0.68819, 0.5, -0.42533\}, \{-0.68819, -0.5, 0.42533\}, \{-0.68819, 0.5, 0.42533\}, \{-0.26287, -0.80902, -0.42533\}, \{-0.26287, 0.80902, -0.42533\}, \{0.26287, -0.80902, 0.42533\}, \{0.26287, 0.80902, 0.42533\}$	sphere

## Bibliography

- [1] T. Cosgrove, *Colloid science: principles, methods and applications* (Blackwell Publishing Ltd., Oxford, 2010).
- [2] M. E. Leunissen, C. G. Christova, A.-P. Hynninen, C. P. Royall, A. I. Campbell, A. Imhof, M. Dijkstra, R. van Roij, and A. van Blaaderen, “Ionic colloidal crystals of oppositely charged particles”, *Nature* **437**, 235 (2005).
- [3] S. C. Glotzer, M. J. Solomon, and N. A. Kotov, “Self-assembly: from nanoscale to microscale colloids”, *AIChE J.* **50**, 2978 (2004).
- [4] A. van Blaaderen, “CHEMISTRY: colloidal molecules and beyond”, *Science* **301**, 470 (2003).
- [5] E. W. Edwards, D. Wang, and H. Möhwald, “Hierarchical organization of colloidal particles: from colloidal crystallization to supraparticle chemistry”, *Macromol. Chem. Phys.* **208**, 439 (2007).
- [6] S. Sacanna and D. J. Pine, “Shape-anisotropic colloids: building blocks for complex assemblies”, *Curr. Opin. Colloid Interface Sci.* **16**, 96 (2011).
- [7] C. S. Plüsch and A. Wittemann, “Shape-tailored polymer colloids on the road to become structural motifs for hierarchically organized materials”, *Macromol. Rapid Commun.* **34**, 1798 (2013).
- [8] E. Duguet, A. Desert, A. Perro, and S. Ravaine, “Design and elaboration of colloidal molecules: an overview”, *Chem. Soc. Rev.* **40**, 941 (2011).
- [9] V. N. Manoharan, M. T. Elsesser, and D. J. Pine, “Dense packing and symmetry in small clusters of microspheres”, *Science* **301**, 483 (2003).
- [10] C. S. Wagner, Y. Lu, and A. Wittemann, “Preparation of submicrometer-sized clusters from polymer spheres using ultrasonication”, *Langmuir* **24**, 12126 (2008).
- [11] M. Hoffmann, C. S. Wagner, L. Harnau, and A. Wittemann, “3D brownian diffusion of submicron-sized particle clusters”, *ACS Nano* **3**, 3326 (2009).
- [12] C. Wagner, B. Fischer, M. May, and A. Wittemann, “Templated assembly of polymer particles into mesoscopic clusters with well-defined configurations”, *Colloid. Polym. Sci.* **288**, 487 (2010).
- [13] I. Schwarz, A. Fortini, C. S. Wagner, A. Wittemann, and M. Schmidt, “Monte Carlo computer simulations and electron microscopy of colloidal cluster formation via emulsion droplet evaporation”, *J. Chem. Phys.* **135**, 244501 (2011).
- [14] E. Lauga and M. P. Brenner, “Evaporation-driven assembly of colloidal particles”, *Phys. Rev. Lett.* **93**, 238301 (2004).
- [15] G. R. Yi, V. N. Manoharan, E. Michel, M. T. Elsesser, S. M. Yang, and D. J. Pine, “Colloidal clusters of silica or polymer microspheres”, *Adv. Mater.* **16**, 1204 (2004).
- [16] V. N. Manoharan, “Colloidal spheres confined by liquid droplets: geometry, physics, and physical chemistry”, *Solid State Commun.* **139**, 557 (2006).
- [17] Y. S. Cho, G. R. Yi, S. H. Kim, D. J. Pine, and S. M. Yang, “Colloidal clusters of microspheres from water-in-oil emulsions”, *Chem. Mater.* **17**, 5006 (2005).
- [18] Y. S. Cho, G. R. Yi, J. M. Lim, S. H. Kim, V. N. Manoharan, D. J. Pine, and S. M. Yang, “Self-organization of bidisperse colloids in water droplets”, *J. Am. Chem. Soc.* **127**, 15968 (2005).
- [19] Y. S. Cho, G. R. Yi, Y. S. Chung, S. B. Park, and S. M. Yang, “Complex colloidal microclusters from aerosol droplets”, *Langmuir* **23**, 12079 (2007).
- [20] Y. Sun and Y. Xia, “Shape-controlled synthesis of gold and silver nanoparticles”, *Science* **298**, 2176 (2002).
- [21] E. Greyson, J. Barton, and T. Odom, “Tetrahedral zinc blende tin sulfide nano- and microcrystals”, *Small* **2**, 368 (2006).
- [22] R. Rice, R. Roth, and C. P. Royall, “Polyhedral colloidal ‘rocks’: low-dimensional networks”, *Soft Matter* **8**, 1163 (2012).
- [23] J. Henzie, M. Grünwald, A. Widmer-Cooper, P. L. Geissler, and P. Yang, “Self-assembly of uniform polyhedral silver nanocrystals into densest packings and exotic superlattices”, *Nat. Mater.* **11**, 131 (2012).
- [24] L. Helden, R. Roth, G. H. Koenderink, P. Leiderer, and C. Bechinger, “Direct measurement of entropic forces induced by rigid rods”, *Phys. Rev. Lett.* **90**, 048301 (2003).
- [25] C. M. van Kats, P. M. Johnson, J. E. A. M. van den Meerakker, and A. van Blaaderen, “Synthesis of monodisperse high-aspect-ratio colloidal silicon and silica rods”, *Langmuir* **20**, 11201 (2004).

- [26] P.-M. König, R. Roth, and S. Dietrich, “Depletion forces between nonspherical objects”, *Phys. Rev. E* **74**, 041404 (2006).
- [27] J. J. Crassous, A. M. Mihut, E. Wernersson, P. Pfeleiderer, J. Vermant, P. Linse, and P. Schurtenberger, “Field-induced assembly of colloidal ellipsoids into well-defined microtubules”, *Nat. Commun.* **5**, 5516 EP (2014).
- [28] P. M. Johnson, C. M. van Kats, and A. van Blaaderen, “Synthesis of colloidal silica dumbbells”, *Langmuir* **21**, 11510 (2005).
- [29] J. Du and R. K. O’Reilly, “Anisotropic particles with patchy, multicompartment and janus architectures: preparation and application”, *Chem. Soc. Rev.* **40**, 2402 (2011).
- [30] B. Peng, F. Smallenburg, A. Imhof, M. Dijkstra, and A. van Blaaderen, “Colloidal clusters by using emulsions and dumbbell-shaped particles: experiments and simulations”, *Angew. Chem. Int. Ed.* **52**, 6709 (2013).
- [31] F. Smallenburg and H. Löwen, “Close packing of rods on spherical surfaces”, *J. Chem. Phys.* **144**, 164903 (2016).
- [32] E. G. Teich, G. van Anders, D. Klotsa, J. Dshemuchadse, and S. C. Glotzer, “Clusters of polyhedra in spherical confinement”, *Proc. Natl. Acad. Sci.* **113**, E669 (2016).
- [33] Y. S. Cho and G. R. Yi, “Microwave-assisted self-organization of colloidal particles inside water-in-oil emulsions”, *J. Dispersion Sci. Technol.* **31**, 169 (2010).
- [34] J. D. Joannopoulos, P. R. Villeneuve, and S. Fan, “Photonic crystals: putting a new twist on light”, *Nature* **386**, 143 (1997).
- [35] J. H. Holtz, J. S. W. Holtz, C. H. Munro, and S. A. Asher, “Intelligent polymerized crystalline colloidal arrays: novel chemical sensor materials”, *Anal. Chem.* **70**, 780 (1998).
- [36] O. D. Velev and A. M. Lenhoff, “Colloidal crystals as templates for porous materials”, *Curr. Opin. Colloid Interface Sci.* **5**, 56 (2000).
- [37] Zhang, A. S. Keys, T. Chen, and S. C. Glotzer, “Self-assembly of patchy particles into diamond structures through molecular mimicry”, *Langmuir* **21**, 11547 (2005).
- [38] J. P. K. Doye, A. A. Louis, I.-C. Lin, L. R. Allen, E. G. Noya, A. W. Wilber, H. C. Kok, and R. Lyus, “Controlling crystallization and its absence: proteins, colloids and patchy models”, *Phys. Chem. Chem. Phys.* **9**, 2197 (2007).
- [39] A.-P. Hynninen, J. H. J. Thijssen, E. C. M. Vermolen, M. Dijkstra, and A. van Blaaderen, “Self-assembly route for photonic crystals with a bandgap in the visible region”, *Nat. Mater.* **6**, 202 (2007).
- [40] Y. Wang, Y. Wang, D. R. Breed, V. N. Manoharan, L. Feng, A. D. Hollingsworth, M. Weck, and D. J. Pine, “Colloids with valence and specific directional bonding”, *Nature* **491**, 51 (2012).
- [41] M. Maldovan, C. K. Ullal, W. C. Carter, and E. L. Thomas, “Exploring for 3D photonic bandgap structures in the 11 f.c.c. space groups”, *Nat. Mater.* **2**, 664 (2003).
- [42] D. Frenkel and B. Smit, *Understanding molecular simulation: from algorithms to applications* (Academic Press, California, 2009).
- [43] N. Metropolis, A. W. Rosenbluth, M. N. Rosenbluth, A. H. Teller, and E. Teller, “Equation of state calculations by fast computing machines”, *J. Chem. Phys.* **21**, 1087 (1953).
- [44] M. Matsumoto and T. Nishimura, “Mersenne twister: a 623-dimensionally equidistributed uniform pseudo-random number generator”, *ACM Trans. Model. Comput. Simul.* **8**, 3 (1998).
- [45] K. Binder and D. Heermann, *Monte Carlo simulation in statistical physics: an introduction* (Springer, Heidelberg, 2002).
- [46] P. Allen and D. Tildesley, *Computer simulation of liquids* (Clarendon Press, New York, 2009).
- [47] L Berthier and W Kob, “The Monte Carlo dynamics of a binary Lennard-Jones glass-forming mixture”, *J. Phys.: Condens. Matter* **19**, 205130 (2007).
- [48] S. Auer and D. Frenkel, “Prediction of absolute crystal-nucleation rate in hard-sphere colloids”, *Nature* **409**, 1020 (2001).
- [49] V. Y. Kiselev, D. Marenduzzo, and A. B. Goryachev, “Lateral dynamics of proteins with polybasic domain on anionic membranes: a dynamic Monte-Carlo study”, *Biophys. J.* **100**, 1261 (2011).
- [50] B. Cichocki and K. Hinsen, “Dynamic computer simulation of concentrated hard sphere suspensions”, *Physica A* **166**, 473 (1990).
- [51] W. Schaertl and H. Sillescu, “Brownian dynamics simulations of colloidal hard spheres. effects of sample dimensionality on self-diffusion”, *J. Stat. Phys.* **74**, 687 (1994).
- [52] D. M. Heyes and A. C. Brańka, “Monte Carlo as Brownian dynamics”, *Mol. Phys.* **94**, 447 (1998).
- [53] M. J. Kotelyanskii and U. W. Suter, “A dynamic Monte Carlo method suitable for molecular simulations”, *J. Chem. Phys.* **96**, 5383 (1992).

- [54] K. Kikuchi, M. Yoshida, T. Maekawa, and H. Watanabe, “Metropolis Monte Carlo method as a numerical technique to solve the Fokker—Planck equation”, *Chem. Phys. Lett.* **185**, 335 (1991).
- [55] X. Z. Cheng, M. B. A. Jalil, H. K. Lee, and Y. Okabe, “Mapping the Monte Carlo scheme to Langevin dynamics: a Fokker-Planck approach”, *Phys. Rev. Lett.* **96**, 067208 (2006).
- [56] E. Sanz and D. Marenduzzo, “Dynamic Monte Carlo versus Brownian dynamics: a comparison for self-diffusion and crystallization in colloidal fluids”, *J. Chem. Phys.* **132**, 194102 (2010).
- [57] F. Romano, C. De Michele, D. Marenduzzo, and E. Sanz, “Monte Carlo and event-driven dynamics of Brownian particles with orientational degrees of freedom”, *J. Chem. Phys.* **135**, 124106 (2011).
- [58] A. Patti and A. Cuetos, “Brownian dynamics and dynamic Monte Carlo simulations of isotropic and liquid crystal phases of anisotropic colloidal particles: a comparative study”, *Phys. Rev. E* **86**, 011403 (2012).
- [59] A. Fortini and M. Schmidt, “Computer simulations of colloidal transport on a patterned magnetic substrate”, *Phys. Rev. E* **83**, 041411 (2011).
- [60] S. Jabbari-Farouji and E. Trizac, “Dynamic Monte Carlo simulations of anisotropic colloids”, *J. Chem. Phys.* **137**, 054107 (2012).
- [61] A. Cuetos and A. Patti, “Equivalence of Brownian dynamics and dynamic Monte Carlo simulations in multicomponent colloidal suspensions”, *Phys. Rev. E* **92**, 022302 (2015).
- [62] J.-P. Hansen and I. R. McDonald, *Theory of simple liquids* (Academic Press, Burlington, 2006).
- [63] S. Le Roux and V. Petkov, “ISAACS – interactive structure analysis of amorphous and crystalline systems”, *J. Appl. Crystallogr.* **43**, 181 (2010).
- [64] P. J. Steinhardt, D. R. Nelson, and M. Ronchetti, “Bond-orientational order in liquids and glasses”, *Phys. Rev. B* **28**, 784 (1983).
- [65] W. Lechner and C. Dellago, “Accurate determination of crystal structures based on averaged local bond order parameters”, *J. Chem. Phys.* **129**, 114707 (2008).
- [66] A. Messiah, *Quantum mechanics* (North-Holland, Amsterdam, 1965).
- [67] J. S. van Duijneveldt and D. Frenkel, “Computer simulation study of free energy barriers in crystal nucleation”, *J. Chem. Phys.* **96**, 4655 (1992).
- [68] S. Winczewski, J. Dziedzic, and J. Rybicki, “A highly-efficient technique for evaluating bond-orientational order parameters”, *Comput. Phys. Commun.* **198**, 128 (2016).
- [69] J. P. Mithen and R. P. Sear, “State between liquid and crystal: locally crystalline but with the structure factor of a liquid”, *Cryst. Growth Des.* **16**, 3049 (2016).
- [70] P. G. de Gennes, “Soft matter”, *Rev. Mod. Phys.* **64**, 645 (1992).
- [71] J. Hu, S. Zhou, Y. Sun, X. Fang, and L. Wu, “Fabrication, properties and applications of Janus particles”, *Chem. Soc. Rev.* **41**, 4356 (2012).
- [72] A. Kumar, B. J. Park, F. Tu, and D. Lee, “Amphiphilic Janus particles at fluid interfaces”, *Soft Matter* **9**, 6604 (2013).
- [73] D. Dendukuri and P. S. Doyle, “The synthesis and assembly of polymeric microparticles using microfluidics”, *Adv. Mater.* **21**, 4071 (2009).
- [74] Z. Nie, W. Li, M. Seo, S. Xu, and E. Kumacheva, “Janus and ternary particles generated by microfluidic synthesis: design, synthesis, and self-assembly”, *J. Am. Chem. Soc.* **128**, 9408 (2006).
- [75] R. F. Shepherd, J. C. Conrad, S. K. Rhodes, D. R. Link, M. Marquez, D. A. Weitz, and J. A. Lewis, “Microfluidic assembly of homogeneous and Janus colloid-filled hydrogel granules”, *Langmuir* **22**, 8618 (2006).
- [76] K.-H. Roh, D. C. Martin, and J. Lahann, “Biphasic Janus particles with nanoscale anisotropy”, *Nat. Mater.* **4**, 759 (2005).
- [77] S. Bhaskar, J. Hitt, S.-W. L. Chang, and J. Lahann, “Multicompartmental microcylinders”, *Angew. Chem. Int. Ed.* **48**, 4589 (2009).
- [78] H. Y. Koo, D. K. Yi, S. J. Yoo, and D. Y. Kim, “A snowman-like array of colloidal dimers for antireflecting surfaces”, *Adv. Mater.* **16**, 274 (2004).
- [79] Z. Li, D. Lee, M. F. Rubner, and R. E. Cohen, “Layer-by-layer assembled Janus microcapsules”, *Macromolecules* **38**, 7876 (2005).
- [80] R. Erhardt, A. Böker, H. Zettl, H. Kaya, W. Pyckhout-Hintzen, G. Krausch, V. Abetz, and A. H. E. Müller, “Janus micelles”, *Macromolecules* **34**, 1069 (2001).
- [81] R. Erhardt, M. Zhang, A. Böker, H. Zettl, C. Abetz, P. Frederik, G. Krausch, V. Abetz, and A. H. E. Müller, “Amphiphilic Janus micelles with polystyrene and poly(methacrylic acid) hemispheres”, *J. Am. Chem. Soc.* **125**, 3260 (2003).
- [82] I. K. Voets, R. Fokkink, T. Hellweg, S. M. King, P. d. Waard, A. d. Keizer, and M. A. Cohen Stuart, “Spontaneous symmetry breaking: formation of Janus micelles”, *Soft Matter* **5**, 999 (2009).

- [83] H. Liang, S. Jiang, and S. Granick, "Simple method to produce Janus colloidal particles in large quantity", *Langmuir* **22**, 9495 (2006).
- [84] S. Jiang and S. Granick, "Janus balance of amphiphilic colloidal particles", *J. Chem. Phys.* **127**, 161102, – (2007).
- [85] S. Jiang, and S. Granick, "Controlling the geometry (Janus balance) of amphiphilic colloidal particles", *Langmuir* **24**, 2438 (2008).
- [86] F. Wurm and A. F. M. Kilbinger, "Polymeric Janus particles", *Angew. Chem. Int. Ed.* **48**, 8412 (2009).
- [87] A. Walther and A. H. E. Müller, "Janus particles: synthesis, self-assembly, physical properties, and applications", *Chem. Rev.* **113**, 5194 (2013).
- [88] L. Hong, A. Cacciuto, E. Luijten, and S. Granick, "Clusters of charged Janus spheres", *Nano Lett.* **6**, 2510 (2006).
- [89] D. Dendukuri, T. A. Hatton, and P. S. Doyle, "Synthesis and self-assembly of amphiphilic polymeric microparticles", *Langmuir* **23**, 4669 (2007).
- [90] A. Goyal, C. K. Hall, and O. D. Velev, "Phase diagram for stimulus-responsive materials containing dipolar colloidal particles", *Phys. Rev. E* **77**, 031401 (2008).
- [91] O. Cayre, V. N. Paunov, and O. D. Velev, "Fabrication of dipolar colloid particles by microcontact printing", *Chem. Commun.*, 2296 (2003).
- [92] K. Van Workum and J. F. Douglas, "Symmetry, equivalence, and molecular self-assembly", *Phys. Rev. E* **73**, 031502 (2006).
- [93] D. Suzuki, S. Tsuji, and H. Kawaguchi, "Janus microgels prepared by surfactant-free pickering emulsion-based modification and their self-assembly", *J. Am. Chem. Soc.* **129**, 8088 (2007).
- [94] S. Jiang, M. J. Schultz, Q. Chen, J. S. Moore, and S. Granick, "Solvent-free synthesis of Janus colloidal particles", *Langmuir* **24**, 10073 (2008).
- [95] M. Klokkenburg, R. P. A. Dullens, W. K. Kegel, B. H. Ern e, and A. P. Philipse, "Quantitative real-space analysis of self-assembled structures of magnetic dipolar colloids", *Phys. Rev. Lett.* **96**, 037203 (2006).
- [96] L. Hong, A. Cacciuto, E. Luijten, and S. Granick, "Clusters of amphiphilic colloidal spheres", *Langmuir* **24**, 621 (2008).
- [97] Q. Chen, J. K. Whitmer, S. Jiang, S. C. Bae, E. Luijten, and S. Granick, "Supracolloidal reaction kinetics of Janus spheres", *Science* **331**, 199 (2011).
- [98] F. Sciortino, A. Giacometti, and G. Pastore, "Phase diagram of Janus particles", *Phys. Rev. Lett.* **103**, 237801 (2009).
- [99] R. Fantoni, A. Giacometti, F. Sciortino, and G. Pastore, "Cluster theory of Janus particles", *Soft Matter* **7**, 2419 (2011).
- [100] R. Fantoni, "A cluster theory for a janus fluid", *Eur. Phys. J. B* **85**, 1 (2012).
- [101] F. Sciortino, A. Giacometti, and G. Pastore, "A numerical study of one-patch colloidal particles: from square-well to Janus", *Phys. Chem. Chem. Phys.* **12**, 11869 (2010).
- [102] M. S. Fern andez, V. R. Misko, and F. M. Peeters, "Self-assembly of Janus particles into helices with tunable pitch", *Phys. Rev. E* **92**, 042309 (2015).
- [103] E. Bianchi, A. Z. Panagiotopoulos, and A. Nikoubashman, "Self-assembly of Janus particles under shear", *Soft Matter* **11**, 3767 (2015).
- [104] M. M. Moghani and B. Khomami, "Self-assembly of spherical Janus particles in electrolytes", *Soft Matter* **9**, 4815 (2013).
- [105] J. Zhang, J. Jin, and H. Zhao, "Surface-initiated free radical polymerization at the liquid-liquid interface: a one-step approach for the synthesis of amphiphilic Janus silica particles", *Langmuir* **25**, 6431 (2009).
- [106] O. D. Velev, K. Furusawa, and K. Nagayama, "Assembly of latex particles by using emulsion droplets as templates. 1. Microstructured hollow spheres", *Langmuir* **12**, 2374 (1996).
- [107] O. D. Velev, K. Furusawa, and K. Nagayama, "Assembly of latex particles by using emulsion droplets as templates. 2. Ball-like and composite aggregates", *Langmuir* **12**, 2385 (1996).
- [108] O. D. Velev, and K. Nagayama, "Assembly of latex particles by using emulsion droplets. 3. Reverse (water in oil) system", *Langmuir* **13**, 1856 (1997).
- [109] B. P. Binks and T. S. Horozov, *Colloidal particles at liquid interfaces* (Cambridge University Press, Cambridge, 2006).
- [110] N. J. A. Sloane, R. H. Hardin, T. D. S. Duff, and J. H. Conway, "Minimal-energy clusters of hard spheres", *Discrete Comput. Geom.* **14**, 237 (1995).
- [111] N. Kern and D. Frenkel, "Fluid–fluid coexistence in colloidal systems with short-ranged strongly directional attraction", *J. Chem. Phys.* **118**, 9882 (2003).

- [112] B. J. Alder and T. E. Wainwright, “Phase transition for a hard sphere system”, *J. Chem. Phys.* **27**, 1208 (1957).
- [113] H. N. W. Lekkerkerker, W. C.-K. Poon, P. N. Pusey, A. Stroobants, and P. B. Warren, “Phase behaviour of colloid + polymer mixtures”, *Europhys. Lett.* **20**, 559 (1992).
- [114] M. Schmidt, H. Löwen, J. M. Brader, and R. Evans, “Density functional for a model colloid-polymer mixture”, *Phys. Rev. Lett.* **85**, 1934 (2000).
- [115] M. Dijkstra, “Phase behavior of hard spheres with a short-range Yukawa attraction”, *Phys. Rev. E* **66**, 021402 (2002).
- [116] L. Vega, E. de Miguel, L. F. Rull, G. Jackson, and I. A. McLure, “Phase equilibria and critical behavior of square-well fluids of variable width by Gibbs ensemble Monte Carlo simulation”, *J. Chem. Phys.* **96**, 2296 (1992).
- [117] H. Liu, S. Garde, and S. Kumar, “Direct determination of phase behavior of square-well fluids”, *J. Chem. Phys.* **123**, 174505 (2005).
- [118] H. Liu, S. K. Kumar, and F. Sciortino, “Vapor-liquid coexistence of patchy models: relevance to protein phase behavior”, *J. Chem. Phys.* **127**, 084902 (2007).
- [119] R. Fantoni, D. Gazzillo, A. Giacometti, M. A. Miller, and G. Pastore, “Patchy sticky hard spheres: Analytical study and Monte Carlo simulations”, *J. Chem. Phys.* **127**, 234507 (2007).
- [120] C. Gögelein, G. Nägele, R. Tuinier, T. Gibaud, A. Stradner, and P. Schurtenberger, “A simple patchy colloid model for the phase behavior of lysozyme dispersions”, *J. Chem. Phys.* **129**, 085102 (2008).
- [121] G. Foffi and F. Sciortino, “On the possibility of extending the Noro-Frenkel generalized law of correspondent states to nonisotropic patchy interactions”, *J. Phys. Chem. B* **111**, 9702 (2007).
- [122] J. de Graaf, N. Boon, M. Dijkstra, and R. van Roij, “Electrostatic interactions between Janus particles”, *J. Chem. Phys.* **137**, 104910 (2012).
- [123] R. Fantoni, *The Janus fluid: A theoretical perspective* (Springer, Heidelberg, 2013).
- [124] P. Pieranski, “Two-dimensional interfacial colloidal crystals”, *Phys. Rev. Lett.* **45**, 569 (1980).
- [125] R. Aveyard, B. P. Binks, and J. H. Clint, “Emulsions stabilised solely by colloidal particles”, *Adv. Colloid Interface Sci.* **100–102**, 503 (2003).
- [126] S. Whitelam, E. H. Feng, M. F. Hagan, and P. L. Geissler, “The role of collective motion in examples of coarsening and self-assembly”, *Soft Matter* **5**, 1251 (2009).
- [127] S. Whitelam, “Approximating the dynamical evolution of systems of strongly interacting overdamped particles”, *Mol. Simul.* **37**, 606 (2011).
- [128] H. E. A. Huitema and J. P. van der Eerden, “Can Monte Carlo simulation describe dynamics? a test on Lennard-Jones systems”, *J. Chem. Phys.* **110**, 3267 (1999).
- [129] H. Pham Van, A. Fortini, and M. Schmidt, “Assembly of open clusters of colloidal dumbbells via droplet evaporation”, *Phys. Rev. E* **93**, 052609 (2016).
- [130] T. Erber and G. M. Hockney, “Equilibrium configurations of N equal charges on a sphere”, *J. Phys. A: Math. Gen.* **24**, L1369 (1991).
- [131] B. W. Clare and D. L. Kepert, “The closest packing of equal circles on a sphere”, *Proc. R. Soc. London, Ser. A* **405**, 329 (1986).
- [132] Y.-S. Cho, T.-Y. Kim, G.-R. Yi, Y.-K. Kim, and C.-J. Choi, “Fabrication of colloidal clusters of polymer microspheres and nonspherical hollow micro-particles from Pickering emulsions”, *Bull. Korean Chem. Soc.* **33**, 159 (2012).
- [133] A. F. Demirörs, J. C. P. Stiefelhagen, T. Vissers, F. Smallenburg, M. Dijkstra, A. Imhof, and A. van Blaaderen, “Long-ranged oppositely charged interactions for designing new types of colloidal clusters”, *Phys. Rev. X* **5**, 021012 (2015).
- [134] S. Whitelam and S. A. F. Bon, “Self-assembly of amphiphilic peanut-shaped nanoparticles”, *J. Chem. Phys.* **132**, 074901 (2010).
- [135] G. Avvisati, T. Vissers, and M. Dijkstra, “Self-assembly of patchy colloidal dumbbells”, *J. Chem. Phys.* **142**, 084905 (2015).
- [136] J. Skilling, “Uniform compounds of uniform polyhedra”, *Math. Proc. Cambridge Philos. Soc.* **79**, 447 (1976).
- [137] A. Yethiraj and A. van Blaaderen, “A colloidal model system with an interaction tunable from hard sphere to soft and dipolar”, *Nature* **421**, 513 (2003).
- [138] J.-W. Kim, R. J. Larsen, and D. A. Weitz, “Synthesis of nonspherical colloidal particles with anisotropic properties”, *J. Am. Chem. Soc.* **128**, 14374 (2006).
- [139] E. Lee, Y.-H. Jeong, J.-K. Kim, and M. Lee, “Controlled self-assembly of asymmetric dumbbell-shaped rod amphiphiles: Transition from toroids to planar nets”, *Macromolecules* **40**, 8355 (2007).

- [140] M. Hoffmann, Y. Lu, M. Schrunner, M. Ballauff, and L. Harnau, “Dumbbell-shaped polyelectrolyte brushes studied by depolarized dynamic light scattering”, *J. Phys. Chem. B* **112**, 14843 (2008).
- [141] S. Chakraborty, J. A. Yang, Y. M. Tan, N. Mishra, and Y. Chan, “Asymmetric dumbbells from selective deposition of metals on seeded semiconductor nanorods”, *Angew. Chem. Int. Ed.* **49**, 2888 (2010).
- [142] D. Nagao, C. M. van Kats, K. Hayasaka, M. Sugimoto, M. Konno, A. Imhof, and A. van Blaaderen, “Synthesis of hollow asymmetrical silica dumbbells with a movable inner core”, *Langmuir* **26**, 5208 (2010).
- [143] D. Nagao, M. Sugimoto, A. Okada, H. Ishii, M. Konno, A. Imhof, and A. van Blaaderen, “Directed orientation of asymmetric composite dumbbells by electric field induced assembly”, *Langmuir* **28**, 6546 (2012).
- [144] K. Yoon, D. Lee, J. W. Kim, J. Kim, and D. A. Weitz, “Asymmetric functionalization of colloidal dimer particles with gold nanoparticles”, *Chem. Commun.* **48**, 9056 (2012).
- [145] J. D. Forster, J.-G. Park, M. Mittal, H. Noh, C. F. Schreck, C. S. O’Hern, H. Cao, E. M. Furst, and E. R. Dufresne, “Assembly of optical-scale dumbbells into dense photonic crystals”, *ACS Nano* **5**, 6695 (2011).
- [146] M. Marechal and M. Dijkstra, “Stability of orientationally disordered crystal structures of colloidal hard dumbbells”, *Phys. Rev. E* **77**, 061405 (2008).
- [147] A. F. Demirörs, P. M. Johnson, C. M. van Kats, A. van Blaaderen, and A. Imhof, “Directed self-assembly of colloidal dumbbells with an electric field”, *Langmuir* **26**, 14466 (2010).
- [148] G. Munao, D. Costa, A. Giacometti, C. Caccamo, and F. Sciortino, “Structure and phase behavior of colloidal dumbbells with tunable attractive interactions”, *Phys. Chem. Chem. Phys.* **15**, 20590 (2013).
- [149] G. Munao, P. O’Toole, T. S. Hudson, D. Costa, C. Caccamo, A. Giacometti, and F. Sciortino, “Phase separation and self-assembly of colloidal dimers with tunable attractive strength: from symmetrical square-wells to Janus dumbbells”, *Soft Matter* **10**, 5269 (2014).
- [150] J. D. McCoy, S. J. Singer, and D. Chandler, “A density functional treatment of the hard dumbbell freezing transition”, *J. Chem. Phys.* **87**, 4853 (1987).
- [151] S. J. Smithline, S. W. Rick, and A. D. J. Haymet, “Density functional theory of freezing for molecular liquids”, *J. Chem. Phys.* **88**, 2004 (1988).
- [152] S. J. Singer and R. Mumaugh, “Monte Carlo study of fluid–plastic crystal coexistence in hard dumbbells”, *J. Chem. Phys.* **93**, 1278 (1990).
- [153] C. Vega, E. P. A. Paras, and P. A. Monson, “Solid–fluid equilibria for hard dumbbells via Monte Carlo simulation”, *J. Chem. Phys.* **96**, 9060 (1992).
- [154] C. Vega, E. P. A. Paras, and P. A. Monson, “On the stability of the plastic crystal phase of hard dumbbell solids”, *J. Chem. Phys.* **97**, 8543 (1992).
- [155] C. Vega and P. A. Monson, “Plastic crystal phases of hard dumbbells and hard spherocylinders”, *J. Chem. Phys.* **107**, 2696 (1997).
- [156] G. A. Chapela and J. Alejandre, “Surface tension and orthobaric densities for vibrating square well dumbbells”, *J. Chem. Phys.* **132**, 104704 (2010).
- [157] G. A. Chapela, F. de Río, and J. Alejandre, “Molecular association of heteronuclear vibrating square-well dumbbells in liquid-vapor phase equilibrium”, *J. Chem. Phys.* **134**, 224105 (2011) [10.1063/1.3598480](https://doi.org/10.1063/1.3598480).
- [158] G. A. Chapela and J. Alejandre, “Liquid-vapor interfacial properties of vibrating square well chains”, *J. Chem. Phys.* **135**, 084126 (2011).
- [159] G. Munaò, P. O’Toole, T. S. Hudson, D. Costa, C. Caccamo, F. Sciortino, and A. Giacometti, “Cluster formation and phase separation in heteronuclear Janus dumbbells”, *J. Phys.: Condens. Matter* **27**, 234101 (2015).
- [160] R. Ni and M. Dijkstra, “Crystal nucleation of colloidal hard dumbbells”, *J. Chem. Phys.* **134**, 034501 (2011).
- [161] N. Heptner, F. Chu, Y. Lu, P. Lindner, M. Ballauff, and J. Dzubiella, “Nonequilibrium structure of colloidal dumbbells under oscillatory shear”, *Phys. Rev. E* **92**, 052311 (2015).
- [162] M. Marechal and M. Dijkstra, “Colloidal hard dumbbells under gravity: structure and crystallization”, *Soft Matter* **7**, 1397 (2011).
- [163] D. Zerrouki, J. Baudry, D. Pine, P. Chaikin, and J. Bibette, “Chiral colloidal clusters”, *Nature* **455**, 380 (2008).
- [164] F. Smalenburg, H. R. Vutukuri, A. Imhof, A. van Blaaderen, and M. Dijkstra, “Self-assembly of colloidal particles into strings in a homogeneous external electric or magnetic field”, *J. Phys.: Condens. Matter* **24**, 464113 (2012).
- [165] T. S. Skelton, Y. Chen, and S. A. F. Bon, “Hierarchical self-assembly of ‘hard-soft’ Janus particles into colloidal molecules and larger supracolloidal structures”, *Soft Matter* **10**, 7730 (2014).
- [166] E. Mani, E. Sanz, P. G. Bolhuis, and W. K. Kegel, “Stabilization of nanoparticle shells by competing interactions”, *J. Phys. Chem. C* **114**, 7780 (2010).

- [167] J. H. Holtz and S. A. Asher, “Polymerized colloidal crystal hydrogel films as intelligent chemical sensing materials”, *Nature* **389**, 829 (1997).
- [168] B. T. Holland, C. F. Blanford, T. Do, and A. Stein, “Synthesis of highly ordered, three-dimensional, macroporous structures of amorphous or crystalline inorganic oxides, phosphates, and hybrid composites”, *Chem. Mater.* **11**, 795 (1999).
- [169] P. Yang, A. H. Rizvi, B. Messer, B. F. Chmelka, G. M. Whitesides, and G. D. Stucky, “Patterning porous oxides within microchannel networks”, *Adv. Mater.* **13**, 427 (2001).
- [170] Y. A. Vlasov, X.-Z. Bo, J. C. Sturm, and D. J. Norris, “On-chip natural assembly of silicon photonic bandgap crystals”, *Nature* **414**, 289 (2001).
- [171] K. M. Ho, C. T. Chan, and C. M. Soukoulis, “Existence of a photonic gap in periodic dielectric structures”, *Phys. Rev. Lett.* **65**, 3152 (1990).
- [172] M. Maldovan and E. L. Thomas, “Diamond-structured photonic crystals”, *Nat Mater* **3**, 593 (2004).
- [173] A. V. Tkachenko, “Morphological diversity of dna-colloidal self-assembly”, *Phys. Rev. Lett.* **89**, 148303 (2002).
- [174] E. Bianchi, P. Tartaglia, E. Zaccarelli, and F. Sciortino, “Theoretical and numerical study of the phase diagram of patchy colloids: ordered and disordered patch arrangements”, *J. Chem. Phys.* **128**, 144504 (2008).
- [175] F. Romano, E. Sanz, and F. Sciortino, “Role of the range in the fluid crystal coexistence for a patchy particle model”, *J. Phys. Chem. B* **113**, 15133 (2009).
- [176] F. Romano, E. Sanz, and F. Sciortino, “Phase diagram of a tetrahedral patchy particle model for different interaction ranges”, *J. Phys. Chem.* **132**, 184501 (2010).
- [177] F. Romano, E. Sanz, and F. Sciortino, “Crystallization of tetrahedral patchy particles in silico”, *J. Phys. Chem.* **134**, 174502 (2011).
- [178] E. Bianchi, G. Doppelbauer, L. Filion, M. Dijkstra, and G. Kahl, “Predicting patchy particle crystals: variable box shape simulations and evolutionary algorithms”, *J. Phys. Chem.* **136**, 214102 (2012).
- [179] G. Doppelbauer, E. G. Noya, E. Bianchi, and G. Kahl, “Competing ordered structures formed by particles with a regular tetrahedral patch decoration”, *J. Phys.: Condens. Matter* **24**, 284124 (2012).
- [180] F. Smallenburg and F. Sciortino, “Liquids more stable than crystals in particles with limited valence and flexible bonds”, *Nat. Phys.* **9**, 554 (2013).
- [181] W. G. Hoover and F. H. Ree, “Melting transition and communal entropy for hard spheres”, *J. Chem. Phys.* **49**, 3609 (1968).
- [182] A. Mulero, *Theory and simulation of hard-sphere fluids and related systems* (Springer, Heidelberg, 2008).
- [183] P. N. Pusey and W. van Meegen, “Phase behaviour of concentrated suspensions of nearly hard colloidal spheres”, *Nature* **320**, 340 (1986).
- [184] P. G. Bolhuis, D. Frenkel, S.-C. Mau, and D. A. Huse, “Entropy difference between crystal phases”, *Nature* **388**, 235 (1997).
- [185] L. V. Woodcock, “Entropy difference between the face-centred cubic and hexagonal close-packed crystal structures”, *Nature* **385**, 141 (1997).
- [186] J. V. Sanders, “Close-packed structures of spheres of two different sizes I. Observations on natural opal”, *Philos. Mag. A* **42**, 705 (1980).
- [187] M. J. Murray and J. V. Sanders, “Close-packed structures of spheres of two different sizes II. The packing densities of likely arrangements”, *Philos. Mag. A* **42**, 721 (1980).
- [188] S. Hachisu and S. Yoshimura, “Optical demonstration of crystalline superstructures in binary mixtures of latex globules”, *Nature* **283**, 188 (1980).
- [189] S. Yoshimura and S. Hachisu, *Order formation in binary mixtures of monodisperse lattices* (Steinkopff, Darmstadt, 1983).
- [190] M. Hasaka, H. Nakashima, and K. Oki, “Structure of the Laves phase observed in polystyrene latexes”, *T. JPN. I. MET.* **25**, 65 (1984).
- [191] P. Bartlett, R. H. Ottewill, and P. N. Pusey, “Superlattice formation in binary mixtures of hard-sphere colloids”, *Phys. Rev. Lett.* **68**, 3801 (1992).
- [192] N. Hunt, R. Jardine, and P. Bartlett, “Superlattice formation in mixtures of hard-sphere colloids”, *Phys. Rev. E* **62**, 900 (2000).
- [193] A. B. Schofield, P. N. Pusey, and P. Radcliffe, “Stability of the binary colloidal crystals AB<sub>2</sub> and AB<sub>13</sub>”, *Phys. Rev. E* **72**, 031407 (2005).
- [194] S. Abbas and T. P. Lodge, “Superlattice formation in a binary mixture of block copolymer micelles”, *Phys. Rev. Lett.* **97**, 097803 (2006).

- [195] M. D. Eldridge, P. A. Madden, and D. Frenkel, "Entropy-driven formation of a superlattice in a hard-sphere binary mixture", *Nature* **365**, 35 (1993).
- [196] M. Eldridge, P. Madden, and D. Frenkel, "The stability of the AB<sub>13</sub> crystal in a binary hard sphere system", *Mol. Phys.* **79**, 105 (1993).
- [197] M. Eldridge, P. Madden, and D. Frenkel, "A computer simulation investigation into the stability of the AB<sub>2</sub> superlattice in a binary hard sphere system", *Mol. Phys.* **80**, 987 (1993).
- [198] M. Eldridge, P. Madden, P. Pusey, and P. Bartlett, "Binary hard-sphere mixtures: a comparison between computer simulation and experiment", *Mol. Phys.* **84**, 395 (1995).
- [199] X. Cottin and P. A. Monson, "Substitutionally ordered solid solutions of hard spheres", *J. Chem. Phys.* **102**, 3354 (1995).
- [200] E. Trizac, M. D. Eldridge, and P. A. Madden, "Stability of the AB crystal for asymmetric binary hard sphere mixtures", *Mol. Phys.* **90**, 675 (1997).
- [201] A. R. Denton and N. W. Ashcroft, "Modified weighted-density-functional theory of nonuniform classical liquids", *Phys. Rev. A* **39**, 4701 (1989).
- [202] A. R. Denton and N. W. Ashcroft, "Weighted-density-functional theory of nonuniform fluid mixtures: application to freezing of binary hard-sphere mixtures", *Phys. Rev. A* **42**, 7312 (1990).
- [203] A. Khein and N. W. Ashcroft, "Generalized density functional theory", *Phys. Rev. Lett.* **78**, 3346 (1997).
- [204] Y. Rosenfeld, "Free-energy model for the inhomogeneous hard-sphere fluid mixture and density-functional theory of freezing", *Phys. Rev. Lett.* **63**, 980 (1989).
- [205] R. Roth, R. Evans, A. Lang, and G. Kahl, "Fundamental measure theory for hard-sphere mixtures revisited: the White Bear version", *J. Phys.: Condens. Matter* **14**, 12063 (2002).
- [206] Y.-X. Yu and J. Wu, "Structures of hard-sphere fluids from a modified fundamental-measure theory", *J. Chem. Phys.* **117**, 10156 (2002).
- [207] H. Hansen-Goos and R. Roth, "Density functional theory for hard-sphere mixtures: the White Bear version mark II", *J. Phys.: Condens. Matter* **18**, 8413 (2006).
- [208] V. B. Warshavsky and X. Song, "Fundamental measure density functional theory studies on the freezing of binary hard-sphere and Lennard-Jones mixtures", *J. Chem. Phys.* **129**, 034506 (2008).
- [209] S. Rice and A. Dinner, *Advances in chemical physics* (John Wiley & Sons, New Jersey, 2015).
- [210] A. B. Hopkins, Y. Jiao, F. H. Stillinger, and S. Torquato, "Phase diagram and structural diversity of the densest binary sphere packings", *Phys. Rev. Lett.* **107**, 125501 (2011).
- [211] A. B. Hopkins, F. H. Stillinger, and S. Torquato, "Densest binary sphere packings", *Phys. Rev. E* **85**, 021130 (2012).
- [212] A.-P. Hynninen, C. G. Christova, R. van Roij, A. van Blaaderen, and M. Dijkstra, "Prediction and observation of crystal structures of oppositely charged colloids", *Phys. Rev. Lett.* **96**, 138308 (2006).
- [213] E. Koos and N. Willenbacher, "Capillary forces in suspension rheology", *Science* **331**, 897 (2011).
- [214] A. Fortini, "Clustering and gelation of hard spheres induced by the Pickering effect", *Phys. Rev. E* **85**, 040401 (2012).
- [215] P. Erwin, "Space filling of crystal structures", *Z. Kristallogr. Cryst. Mater.* **115**, 52 (1961).
- [216] E. G. Noya, C. Vega, J. P. K. Doye, and A. A. Louis, "The stability of a crystal with diamond structure for patchy particles with tetrahedral symmetry", *J. Chem. Phys.* **132**, 234511 (2010).
- [217] F. X. Redl, K. S. Cho, C. B. Murray, and S. O'Brien, "Three-dimensional binary superlattices of magnetic nanocrystals and semiconductor quantum dots", *Nature* **423**, 968 (2003).
- [218] Z. Chen and S. O'Brien, "Structure direction of ii-vi semiconductor quantum dot binary nanoparticle superlattices by tuning radius ratio", *ACS Nano* **2**, 1219 (2008).
- [219] K. P. Velikov, C. G. Christova, R. P. A. Dullens, and A. van Blaaderen, "Layer-by-layer growth of binary colloidal crystals", *Science* **296**, 106 (2002).
- [220] J. K. Kummerfeld, T. S. Hudson, and P. Harrowell, "The densest packing of AB binary hard-sphere homogeneous compounds across all size ratios", *J. Phys. Chem. B* **112**, 10773 (2008).
- [221] L. Filion, M. Marechal, B. van Oorschot, D. Pelt, F. Smallegange, and M. Dijkstra, "Efficient method for predicting crystal structures at finite temperature: variable box shape simulations", *Phys. Rev. Lett.* **103**, 188302 (2009).
- [222] P. Villars, K. Mathis, and F. Hulliger, *The structures of binary compounds* (North-Holland, Amsterdam, 1989).
- [223] E. Parthé, *Crystal chemistry of tetrahedral structures* (Gordon and Breach, Pennsylvania, 1964).
- [224] P. Bartlett, R. H. Ottewill, and P. N. Pusey, "Freezing of binary mixtures of colloidal hard spheres", *J. Chem. Phys.* **93**, 1299 (1990).

- 
- [225] A. L. Rogach, “Binary superlattices of nanoparticles: self-assembly leads to “metamaterials””, *Angew. Chem. Int. Ed.* **43**, 148 (2004).
- [226] S. Underwood, W. van Meegen, and P. Pusey, “Observation of colloidal crystals with the cesium chloride structure”, *Physica A* **221**, 438 (1995).
- [227] A. B. Schofield, “Binary hard-sphere crystals with the cesium chloride structure”, *Phys. Rev. E* **64**, 051403 (2001).
- [228] P. Bartlett and A. I. Campbell, “Three-dimensional binary superlattices of oppositely charged colloids”, *Phys. Rev. Lett.* **95**, 128302 (2005).
- [229] G. H. Ma, T. Fukutomi, and N. Morone, “Preparation and analysis of ordered structure of binary mixtures composed of poly(4-vinylpyridine) and polystyrene microgels”, *J. Colloid Interface Sci.* **168**, 393 (1994).
- [230] S. Hachisu, “NaCl structure in a mixture of silica and gold sols”, *Phase Transitions* **21**, 243 (1990).
- [231] M. Dijkstra, R. van Roij, and R. Evans, “Phase diagram of highly asymmetric binary hard-sphere mixtures”, *Phys. Rev. E* **59**, 5744 (1999).
- [232] D. Rapaport, *The art of molecular dynamics simulation* (Cambridge University Press, Cambridge, 2004).
- [233] L. Martínez, R. Andrade, E. G. Birgin, and J. M. Martínez, “Packmol: a package for building initial configurations for molecular dynamics simulations”, *J. Comput. Chem.* **30**, 2157 (2009).

## List of Publications

This thesis is based on the following publications

- P. V. Hai *et al.*, “Cluster structures of Janus colloidal particles assembled by emulsion droplet evaporation”, in preparation (Chapter 3).
- P. V. Hai, A. Fortini, and M. Schmidt, “Assembly of open clusters of colloidal dumbbells via droplet evaporation”, *Phys. Rev. E* **93**, 052609 (2016)(Chapter 4).
- P. V. Hai *et al.*, “Crystal structures in binary hard-sphere mixtures with colloidal particles tetrahedrally bonded to droplets”, in preparation (Chapter 5).

Other publications by the author

- P. V. Hanh, L. H. Hoang, P. V. Hai, N. V. Minh, X.-B. Chen, and I.-S. Yang, “Crystal quality and optical property of MnWO<sub>4</sub> nanoparticles synthesized by microwave-assisted method”, *J. Phys. Chem. Solids* **74**, 426 (2013).
- N. V. Minh, L. M. Oanh, P. V. Doan, P. V. Hai, and L. H. Hoang, “Investigation of structural, optical and magnetic properties in PbTi<sub>1-x</sub>FexO<sub>3</sub> ceramics”, *Ceram. Int.* **37**, 3785 (2011).
- L. H. Hoang, P. V. Hai, P. V. Hanh, N. H. Hai, X.-B. Chen, and I.-S. Yang, “Microwave-assisted synthesis and characterization of Ti<sub>1-x</sub>VxO<sub>2</sub> (x=0.0-0.10) nanopowders”, *Mater. Lett.* **65**, 3047 (2011).
- L. H. Hoang, P. V. Hai, N. H. Hai, P. V. Vinh, X.-B. Chen, and I.-S. Yang, “The microwave-assisted synthesis and characterization of Zn<sub>1-x</sub>CoxO nanopowders”, *Mater. Lett.* **64**, 962 (2010).
- L. H. Hoang, N. T. M. Hien, N. H. Hai, P. V. Hai, N. T. Khoi, and I.-S. Yang, “Raman spectroscopy of Cu doping in Zn<sub>1-x</sub>CoxO diluted magnetic semiconductor”, *J. Raman Spectrosc.* **40**, 1535 (2009).

## Acknowledgements

I would like to thank all those who have made this thesis possible. My special gratitude goes first to my supervisor, Prof. Dr. Matthias Schmidt, for allowing me the opportunity to do my PhD thesis within his group. Thank you very much for understanding, encouraging, stimulating and many very helpful discussions. Most of all, I want to thank you for your confidence in me which had a great impact on my development.

I also like to express my special acknowledgments to Dr. Andrea Fortini who have been of great help in assisting me through each research stage. I am deeply grateful to him for introducing and patiently guiding me to the computer simulation. I constantly benefited from his continuous support. My thanks also go to Ingmar Schwarz for all the amazing work that he did during his diploma project. His initial development has really helped me approach and understand colloid-droplet systems quickly and effectively. I thank Dr. Daniel de las Heras for being always ready to help. I am grateful to my office mates, Phillip Krinninger and Thomas Geigenfeind for their help and talk. Furthermore, my thanks go to all (ex-) members of the Theoretical physics II group, especially Sebastian Rosenzweig, Florian Dorsch, Thomas Schindler, Lucas Treffenstädt, Julian Garhammer, Johannes Renner and Timo Lebeda, for an extremely friendly environment. A particular 'thank you' goes to Christine Scharf for her kind help and consideration in all kind of administrative problems.

I really appreciate to Prof. Dr. Luc Huy Hoang, my master supervisor, for offering me the unique opportunity and privilege to continue academic career at Faculty of Physics, Hanoi National University of Education. I also want to thank Prof. Dr. Nguyen The Khoi, Prof. Dr. Nguyen Van Hung, Prof. Dr. Nguyen Van Minh for great lectures about experimental physics as well as supporting me to study abroad. My colleagues from Department of Solid State Physics, Dr. Pham Van Vinh, Dr. Dinh Hung Manh, Dr. Nguyen Dinh Lam, Dr. Do Danh Bich, Dr. Pham Do Chung, Dr. Le Mai Oanh, Dr. Trinh Duc Thien, Nguyen Dang Phu, Do Minh Thanh and Dinh Mai Van, deserve acknowledgment for the wonderful atmosphere of team spirit and friendship.

This thesis would not have been accomplished without funds supported by Vietnamese Government Scholarship Program (Project 911). I also appreciate the financial support of Prof. Dr. Matthias Schmidt.

Finally, I would like to thank my parents for supporting me spiritually throughout writing this thesis and my life in general. My most warm gratitude is my wife Linh. Over long periods of time of raising family of two children, she has always supported me completely. I wish to dedicate this thesis with all my love to her.

## Eidesstattliche Vericherung

Hiermit versichere ich an Eides statt, dass ich die vorliegende Arbeit selbstständig verfasst und keine anderen als die von mir angegebenen Quellen und Hilfsmittel verwendet habe.

Weiterhin erkläre ich, dass ich die Hilfe von gewerblichen Promotionsberatern bzw. –vermittlern oder ähnlichen Dienstleistern weder bisher in Anspruch genommen habe, noch künftig in Anspruch nehmen werde.

Zusätzlich erkläre ich hiermit, dass ich keinerlei frühere Promotionsversuche unternommen habe.

Bayreuth, den

Unterschrift